University of Alabama in Huntsville

LOUIS

2017

Analytical investigation of thermoacoustic instabilities in premixed combustion systems

Vijaya Krishna Rani

Follow this and additional works at: https://louis.uah.edu/uah-dissertations

ANALYTICAL INVESTIGATION OF THERMOACOUSTIC INSTABILITIES IN PREMIXED COMBUSTION SYSTEMS

by

VIJAYA KRISHNA RANI

A DISSERTATION

Submitted in partial fulfillment of the requirements
for the degree of Doctor of Philosophy
in
The Department of Mechanical and Aerospace Engineering
to
The School of Graduate Studies
of
The University of Alabama in Huntsville

HUNTSVILLE, ALABAMA

2017

In presenting this dissertation in partial fulfillment of the requirements for a doctoral degree from The University of Alabama in Huntsville, I agree that the Library of this University shall make it freely available for inspection. I further agree that permission for extensive copying for scholarly purposes may be granted by my advisor or, in his/her absence, by the Chair of the Department or the Dean of the School of Graduate Studies. It is also understood that due recognition shall be given to me and to The University of Alabama in Huntsville in any scholarly use which may be made of any material in this dissertation.

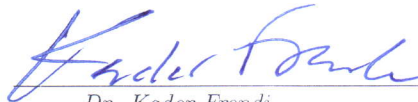Vijaya Krishna Rani

11/07/2017
(date)

DISSERTATION APPROVAL FORM

Submitted by Vijaya Krishna Rani in partial fulfillment of the requirements for the degree of Doctor of Philosophy in Mechanical Engineering and accepted on behalf of the Faculty of the School of Graduate Studies by the dissertation committee.

We, the undersigned members of the Graduate Faculty of The University of Alabama in Huntsville, certify that we have advised and/or supervised the candidate of the work described in this dissertation. We further certify that we have reviewed the dissertation manuscript and approve it in partial fulfillment of the requirements for the degree of Doctor of Philosophy in Mechanical Engineering.

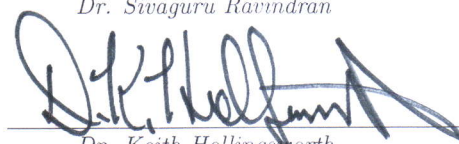|	
Dr. Sarma L. Rani (Date) 11/07/2017	Advisor
Dr. Kader Frendi (Date) 11/7/17	Committee Chair
Dr. Robert Frederick (Date) 11/7/17	
Dr. Babak Shotorban (Date) 11/7/17	
Dr. Sivaguru Ravindran (Date) 11/7/17	
Dr. Keith Hollingsworth (Date) 11/7/17	Department Chair
Dr. Shankar Mahalingam (Date) 11/08/17	College Dean
Dr. David Berkowitz (Date) 11/13/17	Graduate Dean

ABSTRACT

School of Graduate Studies
The University of Alabama in Huntsville

Degree <u> Doctor of Philosophy </u> College/Dept. <u> Engineering/Mechanical and </u>

<u> Aerospace Engineering </u>

Name of Candidate <u> Vijaya Krishna Rani </u>

Title <u> Analytical Investigation of Thermoacoustic Instabilities in </u>

<u> Premixed Combustion Systems </u>

The primary objective of this dissertation is to develop and investigate various analytical methods to predict thermoacoustic instabilities in premixed combustion systems. The analytical models derived as part of this study are of four main types: (1) Acoustically consistent, linear modal analysis method to predict the longitudinal and transverse combustion instabilities in a dump combustor; (2) Novel level set method for deriving flame surface-area response to incident acoustic fluctuations; (3) Novel approximate analytical solutions to acoustic waves in inhomogeneous media; and (4) Investigation of the limit-cycle behavior of nonlinear acoustic wave equation with combustion source term.

The linear modal analysis method that was developed in this study, has a number of novel and distinguishing features when compared to prior works on combustion instability. (i) Combustion instabilities are a thermoacoustic phenomenon, i.e. they are manifested as self-excited acoustic oscillations that are sustained by a feedback loop between the acoustic perturbations and the flame heat-release fluctuations. Therefore, first and foremost, an instability model must be able to predict

the natural acoustic modes of the combustor in the absence of combustion. Our model satisfies this criterion by successfully predicting the acoustic modes of ducts with multiple discontinuities in cross-sectional area. Such a consistency testing of an instability model had not been performed previously. (ii) New acoustically consistent matching conditions with distinct forms for the purely axial and non-axial modes were developed and applied at the zonal interfaces of a duct, whereas prior studies employed the conventional mass, momentum, and energy balances at the interfaces. For the purely axial modes, acoustic mass velocity and total pressure are mathced across the interface while for non-axial modes, the continuity of acoustic velocity and pressure fluctuations is applied. The new matching conditions are essential to accurately predict the duct acoustic modes. (iii) Effects of edge conditions on the linear modal analysis of ducts with area discontinuities are analyzed in great detail. Edge conditions are constraints that need to be satisfied in addition to the matching conditions at an area discontinuity. (iv) Through a novel approach, the effects of the fluctuating heat-release source term in the acoustic wave equation are directly incorporated into the modified axial wavenumbers in the combustion region. This approach obviates the need for applying a separate matching condition across the flame. (v) The analytical model presented in this work, is the first to account for realistic mean flame shapes in combustion instability analysis, whereas prior models assumed that combustion occurred in a cross-sectional plane of zero thickness.

A new G-equation level-set method was developed that describes flame surface-area response to acoustic oscillations incident on the flame. This method presents a different paradigm when compared to an approach that has existed for at least
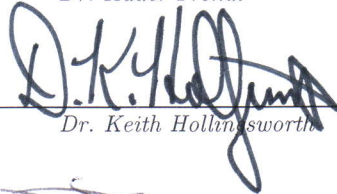
two decades. In this method, we directly solve for the level set fluctuations G' in terms of velocity fluctuations, and relate the flame surface-area oscillations to G', whereas in the conventional f-approach, the level-set G is expressed as $G(x, y, t) = x - f(y, t)$ and a solution for f is sought. In the absence of turbulent flame-speed fluctuations, the response functions from the present G-equation approach are in good agreement with those from the conventional f-equation approach. However, when turbulent flame-speed fluctuations are included, the two approaches differ, principally in the flame response to axial velocity fluctuations. This G-equation approach is more generalized since the effects of flame-speed fluctuations are reflected in both the axial and tranverse velocity response functions; whereas in the f-equation approach, this inclusion predominantly affects the axial velocity fluctuations.
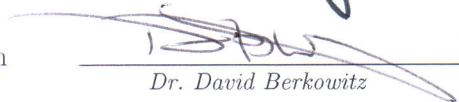
As part of this work, an analytical Wentzel-Kramers-Brillouin (WKB)-type approximation for a 2-D acoustic duct with axial gradients in temperature, axial mean flow and duct cross-sectional area has been developed. Standard WKB method uses two principal approximations: (i) the amplitude of the wave varies slowly compared to its frequency and (ii) the mean properties vary slowly in space. The modified WKB method developed in this study relaxes the latter assumption of slowly varying mean properties. Using this novel WKB-type solutions along with the acoustically consistent modal analysis framework that was developed earlier, we are able to compute acoustic resonant frequencies as well as predict lonigtudinal unstable modes of a duct with discontinuities, which has not been done before.

In this study, the effects of nonlinear acoustic and combustion source terms on the limit-cycle behavior of thermoacoustic instabilities in a Rijke tube has also been

investigated. First, the relevant parameters that dictate the linear instbility viz., convective time-lag and mean heat-release rate are identified. And in the linearly unstable regime, the limit-cycle amplitudes for the first two longitudinal modes of a duct are computed. It was found that at higher mean heat release rates, combustion source term nonlinearities are more important to achieve limi-cycle amplitudes than purely acoustic nonlinearities.

Abstract Approval: Committee Chair   _____ 11/7/17
                                                      Dr. Kader Frendi

                  Department Chair   _____ 11/7/17
                                                    Dr. Keith Hollingsworth

                  Graduate Dean   _____ 11/13/17
                                                 Dr. David Berkowitz

ACKNOWLEDGMENTS

Experimental Program to Stimulate Competitive Research (ALEPSCoR) Graduate

Research Scholars Program (GRSP) Award.

TABLE OF CONTENTS

LIST OF FIGURES

LIST OF TABLES

LIST OF SYMBOLS

SYMBOL	DEFINITION
$A_n^{\pm}$	Amplitudes of the nth mode propagating in the positive and negative x directions
$\bar{c}$	Mean sound speed
c_v	Specific heat at constant volume
$\mathscr{C}$	Amplitude of the acoustic pressure wave
$\mathrm{d}A$	Infinitesimal surface area
$\mathrm{d}\dot{Q}$	nfinitesimal heat-release rate
G	Level-set function
h_r	Heat of reaction
i	$\sqrt{-1}$
$k_n^{\pm}$	Axial wavenumbers of the nth mode propagating in the positive and negative x directions
k_y	Transverse wavenumber
L	Length of the duct
L_f	ength of the flame along the axial direction
m	Slope of the mean flame
M_{bulk}	Bulk Mach number

$\overline{M}$	Mean flow Mach number
n	Modal index
p	Pressure
q	Heat-release rate per unit volume
Q	Total heat-release rate
R	Specific gas constant
R_{HR}	Heat-of-reaction response function
R_p	Pressure response function
R_{ST}	Turbulent-flame-speed response function
R_u	Axial-velocity response function
R_v	Transverse-velocity response function
$R_{u,f}$	Axial-velocity response function in the f-equation approach
$R_{v,f}$	Transverse-velocity response function in the f-equation approach
R_ρ	Density response function
s_T	Turbulent flame speed
S	Duct cross-sectional area
T	Temperature
$u,\ v$	Axial and transverse components of velocity

$u_f,\ v_f$	Axial and transverse components of velocity on the flame
γ	Ratio of specific heats
ρ	Density
τ	Convective time-lag
ϕ	Equivalence ratio
Ω	Angular frequency
$\bar{\cdot}$	Mean quantity
$\cdot'$	Fluctuating quantity

I dedicate this work to my loving parents,

Shri. Murali Krishna Rani *and* **Smt. Indira Rani**

The Road goes ever on and on
Down from the door where it began.
Now far ahead the Road has gone,
And I must follow, if I can,
Pursuing it with eager feet,
Until it joins some larger way
Where many paths and errands meet.
And whither then? I cannot say.

—J. R. R. Tolkien

CHAPTER 1

INTRODUCTION

Combustion instabilities are a significant concern when designing and operating combustors in a number of propulsion systems such as the low NO_x gas turbines, solid and liquid rocket motors, jet engine afterburners, and ramjets. Combustion instabilities refer to the self-excited acoustic oscillations that are triggered by the constructive interference between the flow perturbations in the combustor and the flame heat-release fluctuations. The self-excited oscillations are sustained by a feedback loop between the combustor perturbations and the heat release fluctuations, wherein the former generate the latter and the latter, in turn, pump energy into the former. The persistent, high-amplitude pressure oscillations resulting from combustion instability could compromise the structural integrity and performance of an engine. Therefore, the ability to predict the unstable frequencies for a given combustor configuration will facilitate the isolation and mitigation of these instabilities using active and/or passive design modifications. Detailed experiments to map the combustor stability boundaries are known to be cost- and time-intensive. Sufficiently resolved numerical simulations are also computationally prohibitive due to the complex coupling of turbulence, combustion, acoustics and multiphase flow.
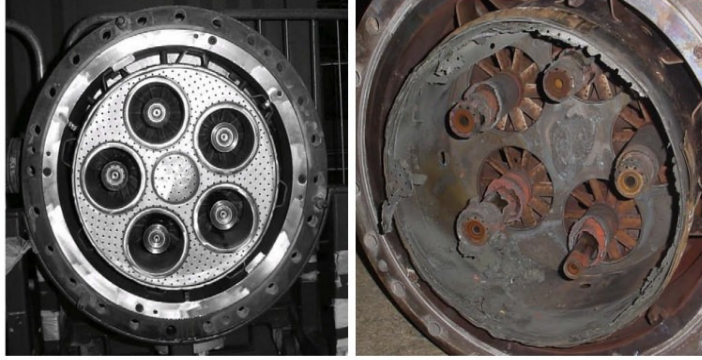
Figure 1.1: A new injector plate on the left and the same plate damaged due to combustion instabilities on the right.

The design of gas-turbine combustors has been considerably improved in the past decades to meet increasingly restrictive emission regulations. The major concern of the emission control is on nitric oxides (NO_x). Researchers have been working seriously to develop low NO_x combustors for gas turbines. So far, two approaches have been taken. One involves various minor modifications to the conventional designs, at the same time retaining the existing size and configuration. Therefore, the improvements can be made without trespassing far outside the bounds of the established technology. However, the end product is a tradeoff between the effectiveness of emission control and the combustor performance. The other approach is essentially a rejection of the traditional design philosophy based on heterogeneous diffusion flames. Of the various advanced concepts now being actively studied, the most promising ones appear to be lean-premixed (LPM) combustion, variable geometry, and catalytic oxidation (Lefebvre, A. H., 1999). Among these developments,

the concept of lean-premixed combustors, which are generally similar to combustion system hardware used in conventional gas turbines, is believed to be the best solution. In LPM combustion, the fuel and oxidizer are premixed upstream of the combustor. Due to the lean-premixed condition, the temperature in the combustion chamber is significantly reduced, consequently leading to the lower level of NOx emission.

While lean-premix technology shows promising prospect for the emission control of NOx, pressure oscillations driven by combustion have been a repeated problem as the result of specific changes made to the combustor to accommodate the lean-premix approach. Unlike diffusion-style combustors, most of the combustion air is sent through the fuel injector in premix systems, eliminating the need for downstream combustion air holes, which would otherwise provide acoustic damping that constrains the occurrence of the oscillations (Richards, G.A., 2000). Furthermore, the coupling between the heat- release and the acoustic perturbations is weak in diffusion systems due to the distributed reaction associated with diffusion burning, while the likelihood of this coupling is fairly high in LPM combustion systems. Slight disturbances in pressure will create immediate variations in airflow, causing a subsequent change in equivalence ratio. Near the lean combustion limit that is optimum for the operation from the emission-control viewpoint, even minor changes in equivalence ratio can lead to significant fluctuations in heat release, compared to the stoichiometric condition. These variations can induce severe combustion instabilities and cause serious damage to the engine. Since the 1970s, with the development of LPM systems, substantial attention has been given to the causes of and potential solutions for combustion instability in gas turbine combustors. The passive control technique, for instance, acoustic

liners, and Helmholtz resonators have been used to suppress the acoustic waves when combustion instability occurs. Meanwhile, active control methods also have been developed and have made some progress.

Two fundamental origins can explain the prevalence of combustion instability in various systems (Culick, 1998): (1) an exceedingly small part of the available energy is sufficient to produce unacceptable large unsteady motions; (2) the processes tending to attenuate unsteady motions are weak relative to driving energy. In addition, gas turbine combustor chambers are almost entirely closed, which prevents the perturbations from traveling out. Therefore, it is implied that the possibility of instabilities occurring in a newly designed gas-turbine combustor must be recognized and anticipated. In order to design systems with stable combustion operation, it is an essential to understand the characteristics of combustion instability.

The primary objective of this dissertation is to develop and investigate various analytical methods to predict thermoacoustic instabilities in premixed combustion systems. The analytical models derived as part of this study are of four main types: (1) Acoustically consistent, linear modal analysis method to predict the longitudinal and transverse combustion instabilities in a dump combustor; (2) Novel level set method for deriving flame surface-area response to incident acoustic fluctuations; and (3) Novel approximate analytical solutions to acoustic waves in inhomogeneous media; and (4) Investigation of the limit-cycle behavior of nonlinear acoustic wave equation with combustion source term. Each of these four topics forms a chapter in this study. Each chapter addresses a fundamental problem in the study of combustion instabilities and progressively applies the ideas and techniques developed in

the prior chapter to upcoming chapters that tackle a different problem concerning thermoacoustic instabilities.

1.1 Derivation of the Acoustic Wave Equation

Analytical investigation of combustion instabilities involves predicting the natural acoustic modes of the combustor and modeling the flame transfer function (FTF) that relates the heat-release fluctuations to acoustic pressure and velocity perturbations. In order to study the problem of combustion instabilities, we first derive the acoustic wave equation with combustion source term from the governing mass, momentum and energy balance equations. The continuity equation is given by

$$\frac{\partial \rho}{\partial t} + \boldsymbol{\nabla} \bullet (\rho \mathbf{u}) = 0 \tag{1.1}$$

where ρ is the fluid density and $\mathbf{u}$ is the flow velocity. We decompose the flow variables into mean and fluctuating quantities (e.g., $\rho = \overline{\rho} + \rho'$) yielding the mean and fluctuating forms of the continuity equation.

$$\boldsymbol{\nabla}\overline{\rho} + \overline{\rho}\boldsymbol{\nabla} \bullet \mathbf{u} = 0 \tag{1.2}$$

$$\frac{\partial \rho'}{\partial t} + \boldsymbol{\nabla}\rho' \bullet \overline{\mathbf{u}} + \boldsymbol{\nabla}\overline{\rho} \bullet \mathbf{u}' + \boldsymbol{\nabla}\rho' \bullet \mathbf{u}' + \overline{\rho}\boldsymbol{\nabla} \bullet \mathbf{u}' + \rho'\boldsymbol{\nabla} \bullet \overline{\mathbf{u}} + \rho'\boldsymbol{\nabla} \bullet \mathbf{u}' = 0 \tag{1.3}$$

The inviscid momentum balance equation is

$$\rho\left(\frac{\partial \mathbf{u}}{\partial t} + \mathbf{u} \bullet \boldsymbol{\nabla}\mathbf{u}\right) = -\boldsymbol{\nabla}p \tag{1.4}$$

where p is the fluid pressure. Mean and fluctuating forms (upto first order) of the momentum equation are

$$\bar{\rho}\left(\frac{\partial\bar{\mathbf{u}}}{\partial t}+\bar{\mathbf{u}}\bullet\boldsymbol{\nabla}\bar{\mathbf{u}}\right)=-\boldsymbol{\nabla}\bar{p} \tag{1.5}$$

$$\bar{\rho}\frac{\partial\mathbf{u}'}{\partial t}+\rho'\frac{\partial\mathbf{u}'}{\partial t}+\bar{\rho}(\bar{\mathbf{u}}\bullet\boldsymbol{\nabla})\mathbf{u}'+\rho'(\bar{\mathbf{u}}\bullet\boldsymbol{\nabla})\bar{\mathbf{u}}+\rho'(\bar{\mathbf{u}}\bullet\boldsymbol{\nabla})\mathbf{u}'+\rho'(\mathbf{u}'\bullet\boldsymbol{\nabla})\bar{\mathbf{u}}+\bar{\rho}(\mathbf{u}'\bullet\boldsymbol{\nabla})\mathbf{u}'+\rho'(\mathbf{u}'\bullet\boldsymbol{\nabla})\mathbf{u}'=-\boldsymbol{\nabla}p' \tag{1.6}$$

The energy balance equation written in terms of pressure with the viscous dissipation terms dropped is [14]

$$\frac{\partial p}{\partial t}+\mathbf{u}\bullet\boldsymbol{\nabla}p+\gamma p\boldsymbol{\nabla}\bullet\mathbf{u}=(\gamma-1)q \tag{1.7}$$

where γ is the ratio of specific heats and q is the heat-release rate per unit volume. The mean and the fluctuating forms of the energy equation are

$$\frac{\partial\bar{p}}{\partial t}+\bar{\mathbf{u}}\bullet\boldsymbol{\nabla}\bar{p}+\gamma\bar{p}\boldsymbol{\nabla}\bullet\bar{\mathbf{u}}=(\gamma-1)\bar{q} \tag{1.8}$$

$$\frac{\partial p'}{\partial t}+\bar{\mathbf{u}}\bullet\boldsymbol{\nabla}p'+\mathbf{u}'\bullet\boldsymbol{\nabla}\bar{p}+\mathbf{u}'\bullet\boldsymbol{\nabla}p'+\gamma(\bar{p}\bullet\boldsymbol{\nabla}\mathbf{u}'+p'\bullet\boldsymbol{\nabla}\bar{\mathbf{u}}+p'\bullet\boldsymbol{\nabla}\mathbf{u}')=(\gamma-1)q' \tag{1.9}$$

Multiplying Eq. (1.9) with $\frac{1}{\bar{c}^2}$ (where $\bar{c}$ is the mean speed of sound) and taking the time derivative of the resulting equation and subtracting it from the divergence of (1.6), yields

$$\frac{1}{\bar{c}^2}\frac{\partial^2 p'}{\partial t^2}-\nabla^2 p'=\mathscr{F}_1+\mathscr{F}_2+\mathscr{F}_3 \tag{1.10}$$

6

where

$$\mathscr{F}_1 = \boldsymbol{\nabla} \bullet \left(\bar{\rho} \frac{\partial \mathbf{u}'}{\partial t} \right) + \boldsymbol{\nabla} \bullet (\bar{\rho}(\bar{\mathbf{u}} \bullet \boldsymbol{\nabla})\mathbf{u}') + \boldsymbol{\nabla} \bullet (\bar{\rho}(\mathbf{u}' \bullet \boldsymbol{\nabla})\bar{\mathbf{u}}) + \boldsymbol{\nabla} \bullet \left(\frac{p'}{\bar{c}^2}(\bar{\mathbf{u}} \bullet \boldsymbol{\nabla})\bar{\mathbf{u}} \right)$$
$$- \frac{1}{\bar{c}^2} \frac{\partial}{\partial t} (\bar{\mathbf{u}} \bullet \boldsymbol{\nabla} p') - \frac{1}{\bar{c}^2} \frac{\partial}{\partial t} (\mathbf{u}' \bullet \boldsymbol{\nabla} \bar{p}) - \frac{\gamma}{\bar{c}^2} \frac{\partial}{\partial t} (\bar{p} \boldsymbol{\nabla} \bullet \mathbf{u}') - \frac{1}{\bar{c}^2} \frac{\partial}{\partial t} (p' \boldsymbol{\nabla} \bullet \bar{\mathbf{u}})$$

$$(1.11)$$

$$\mathscr{F}_2 = \boldsymbol{\nabla} \bullet \left(\frac{p'}{\bar{c}^2}(\mathbf{u}' \bullet \boldsymbol{\nabla})\bar{\mathbf{u}} \right) + \boldsymbol{\nabla} \bullet \left(\frac{p'}{\bar{c}^2}(\mathbf{u}' \bullet \boldsymbol{\nabla})\mathbf{u}' \right) - \frac{1}{\bar{c}^2} \frac{\partial}{\partial t} (\mathbf{u}' \bullet \boldsymbol{\nabla} p')$$
$$- \frac{1}{\bar{c}^2} \frac{\partial}{\partial t} (p' \boldsymbol{\nabla} \bullet \mathbf{u}') + \boldsymbol{\nabla} \bullet (\bar{\rho}(\mathbf{u}' \bullet \boldsymbol{\nabla})\mathbf{u}') + \boldsymbol{\nabla} \bullet \left(\frac{p'}{\bar{c}^2} \frac{\partial \mathbf{u}'}{\partial t} \right)$$

$$(1.12)$$

$$\mathscr{F}_3 = \frac{\gamma - 1}{\bar{c}^2} \frac{\partial q'}{\partial t} \qquad (1.13)$$

Equation (1.10) is an inhomogeneous acoustic wave equation where the left hand side (LHS) is the standard wave part and the right hand side (RHS) contains the linear source terms in $\mathscr{F}_1$, the nonlinear source terms in $\mathscr{F}_2$ and the combustion source term in $\mathscr{F}_3$.

CHAPTER 2

AN ACOUSTICALLY CONSISTENT INVESTIGATION OF COMBUSTION INSTABILITIES IN A DUMP COMBUSTOR

2.1 Abstract

An acoustically consistent, linear modal analysis-based analytical method is presented to predict the longitudinal and transverse combustion instabilities in a two-dimensional (2-D) cartesian dump combustor. At first, rigorous acoustical analysis (without combustion) is performed of two duct configurations with one and two discontinuities in cross-sectional area. Novel, acoustically consistent jump or matching conditions are developed and applied at the duct cross-sectional interface(s), with distinct forms for the purely axial and non-axial modes. The effects of uniform and non-uniform mean flow, cross-sectional area ratio, as well as of different types of boundary conditions on the duct acoustic modes are investigated. Acoustic modal frequency predictions are in excellent agreement with the analytical and numerical results of Meissner [1]. In the second part, combustion instabilities of a 2-D, cartesian dump combustor are investigated. The instability analysis employs the developed acoustically consistent jump conditions, instead of the conventional mass, momentum, and energy balance-based conditions. Effects of the fluctuating heat-release

8

source term in the acoustic wave equation are incorporated directly into the longitudinal wavenumber, obviating the need for a separate energy matching condition across the flame. A detailed investigation of the parametric space and boundary conditions affecting combustion instabilities is undertaken, and the consistency of the modal analysis with the Rayleigh criterion is explicitly demonstrated. Further, the present approach enables the consideration of arbitrary mean flame shapes in determining the unstable modes. Instabilities are demonstrated for the fundamental longitudinal mode and its harmonics, as well as for the fundamental transverse mode. Effects of cross-sectional area ratio and flow Mach number on the unstable-mode growth rates are also presented.

2.2 Introduction

Combustion instabilities are a significant concern when designing and operating combustors in a number of propulsion systems such as the low NO_x gas turbines, solid and liquid rocket motors, and jet engine afterburners. Combustion instabilities are manifested as self-excited acoustic oscillations that are triggered by the constructive interference between the flow perturbations in the combustor and the flame heat-release fluctuations. The self-excited oscillations are sustained by a feedback loop between the combustor perturbations and the heat release fluctuations, wherein the former generate the latter and the latter, in turn, pump energy into the former. The persistent, high-amplitude pressure oscillations resulting from combustion instability could compromise the structural integrity and performance of an engine. Therefore, the ability to predict the unstable frequencies for a given combustor configuration

will facilitate the isolation and mitigation of these instabilities using active and/or passive design modifications. Detailed experiments and well-resolved computations to map the combustor stability boundaries are known to be cost- and time-intensive.

It is in this context that reduced-order analytical approaches are attractive because such methods can provide reasonably accurate predictions in a time- and cost-effective manner. Principally, these methods are based on utilizing the inherently acoustic nature of combustion instabilities. Analytical investigation of combustion instabilities entails two broad aspects: acoustics and combustion. The former involves calculating the resonant frequencies of a given combustor configuration, while the latter consists of deriving the flame response function and incorporating it into the broader acoustic model to determine the unstable modes. Each of these aspects is quite complex in and of itself, so we have adopted a step-by-step approach with rigorous validation at every stage. This allows us to both study the individual aspects of physics in great detail and explore an extensive parametric space impacting combustion instability.

The current study comprises a number of novel and distinguishing features when compared to prior works on combustion instability, including that by one of the current authors [4]. These features can be summarized as follows: (1) Rigorous, *a priori* acoustical analysis of two different duct configurations with area discontinuities is performed. The effects on acoustic mode predictions of a wide space of parameters, non-uniform mean flow profiles, and various types of boundary conditions are exhaustively explored. The impact of non-uniform mean velocity profile on combustor acoustics has been investigated for the first time, where in both lami-

nar parabolic and turbulent power-law profiles are considered; (2) Novel acoustically consistent matching conditions are developed and applied at the zonal interfaces of a duct, whereas the conventional mass, momentum, and energy balances were employed in prior studies [4]; (3) Effects of edge conditions on linear modal analysis of ducts with area discontinuities are discussed in substantial detail. Edge conditions are constraints that need to be satisfied in addition to jump conditions at an area discontinuity; and (4) Through a novel approach, effects of the fluctuating heat-release source term in the acoustic wave equation are directly incorporated into the modified axial wavenumbers in the combustion region. This approach obviates the need for applying an energy matching condition across the flame.

Crucial to the reliable prediction of combustion instabilities is the accurate determination of combustion chamber acoustics because it is seen that the unstable frequencies are close to the natural frequencies of the combustor. In the absence of combustion, the acoustic modes of a chamber with uniform cross-section are the well-known normal modes. However, most combustion chambers have non-uniform cross-sections (e.g., an area discontinuity in a dump combustor). The longitudinal, transverse and mixed acoustic modes will therefore have to be determined for the entire duct inclusive of area changes. Further, in combustors, one will have to include in the acoustical analysis the regions of high heat release rates. In the proximity of discontinuities such as a change in cross-section, the high-frequency mixed (axial-transverse) modes also become significant. These mixed modes are generally evanescent, i.e., they decay exponentially away from the discontinuity. The presence of combustion could, however, excite one of these higher modes making them unstable.

Linear modal analysis is a well-established approach to determine the unstable modes of a combustion chamber. Dowling and Stow [5] provided a comprehensive, tutorial-like review of this method in the context of lean premixed prevaporized gas turbine combustors. Most prior works employing modal analysis belong to one of two broad categories. The first consists of studies that include geometrical complexities such as discontinuities in cross-section, but perform a 1-D analysis by considering only the purely axial modes [6–8]. The coupling of axial and non-axial modes is ignored primarily because of the analytical complexity it introduces. The second category consists of studies that include both axial and non-axial modes, but consider only simplified geometries whose resonant frequencies are the well-known normal modes, e.g., a uniform cross-section duct [9,10]. In addition, the vast parametric space affecting instabilities including the mean velocity profile, ratio of the areas of cross-section, realistic flame shapes, boundary conditions, and the time-lag between pressure and heat release fluctuations have not been thoroughly investigated, especially over a broad frequency space consisting of axial and non-axial modes.

Hubbard and Dowling [11] performed a 1-D linear stability analysis of a simplified premixed gas turbine geometry. Two flame shapes, a 1-D planar flame and a 2-D conical flame, were considered both occurring immediately downstream of the primary premix duct. Entropy fluctuations were also included in the stability analysis. It is shown that the time-lag between fuel injection and combustion is an important parameter, and instability occurs when the product of frequency and time-lag $\Omega\tau \sim 0.5$, which is when Rayleigh's criterion is also satisfied. In a study similar to [11], Hubbard and Dowling [12] concluded that the form of the flame response function does

not significantly impact the eigenmode predictions, but the phase lag $\Omega\tau$ determines whether a mode is stable or not. Dowling and Hubbard [13] also investigated the instability characteristics of a number of 1-D combustor configurations including: (1) a duct with rigid and open ends, (2) a duct with choked inlet and outlet boundaries and a 1-D planar flame, (3) a duct with a bluffbody-stabilized 2-D flame, and (4) a duct with a choked inlet and an open outlet and a 1-D planar flame.

Lieuwen [7] performed a 1-D linear modal analysis to determine the combustion stability boundaries of a simplified low NO_x gas turbine configuration. The turbine geometry consisted of a fuel line, an inlet duct, and a larger cross-section combustion chamber. A 2-D conical mean flame shape was considered in conjunction with a flame response function that related flame heat-release fluctuations to the equivalence ratio fluctuations at the flame. The flame response function also included a time-lag in the form of an averaged convective time-scale that accounted for the mean distance between the fuel line and the flame base. The parametric space investigated included the variation of fuel-line length and location, mean equivalence ratio, and the inlet Mach number.

You [14] performed a comprehensive investigation of combustion instabilities in a 3-D combustion chamber with an axially varying circular cross-section into which fuel was introduced through swirl injectors. This study is remarkable for the multitude of the physics included in the instability analysis, including: 3-D acoustic fluctuations comprising velocity, pressure, vorticity and entropy fluctuations; detailed flame response function relating heat release fluctuations to the acoustic fluctuations using separate response functions for the pressure fluctuations, as well as the three velocity

13

fluctuations. Modal analysis was performed by discretizing the varying cross-section chamber into a large number of axial segments, with matching conditions at the interfaces between neighboring segments. The matching conditions included mass, momentum and entropy balances across an interface. It is interesting that the effects of heat release were incorporated into the modal analysis through the entropy matching condition, and not through an explicit energy balance. While You's study [14] is quite comprehensive in its inclusion of physics, a thorough mapping of the parametric space impacting instabilities, such as the effects of inflow Mach number and boundary conditions, was not considered.

Rani [4] developed an analytical approach to predict the combustion instabilities of a 2-D bluffbody stabilized flame. In that study [4], a 2-D modal analysis was used in conjunction with a flame response function that related flame heat-release fluctuations to those in the flame surface area. A detailed G-equation approach was used to derive the flame response function. The fluctuating field included entropy and vorticity fluctuations in addition to acoustic fluctuations. Mean flow and temperature and mean heat-release rate, needed as inputs to the model, were obtained from highly resolved 2-D large eddy simulation (LES) data for the bluffbody flame. Reasonable quantitative agreement was found between the modal analysis and LES instability predictions.

The principal objective of this study is to develop a reduced-order analytical model to determine the combustion stability characteristics of a 2-D cartesian dump combustor. To this end, an acoustically consistent linear modal analysis-based method is presented. Prior to determining the combustion instabilities, a detailed

14

investigation was undertaken of the acoustics of ducts with discontinuities in cross-section. Using linear modal analysis, the axial, transverse and mixed acoustic modes were determined for two duct configurations with one and two area discontinuities. The effects of uniform and non-uniform mean flow, mean inflow Mach number, cross-sectional area ratio, as well as of the different types of boundary conditions on the duct acoustic modes were investigated. For the case with no mean flow and closed-closed boundary conditions at the duct inlet and outlet, the current acoustic mode predictions are compared with those of Meissner [1]. Meissner used a 1-D impedance-based analytical approach to determine the longitudinal acoustic modes, and numerical simulations based on a forced oscillator method to compute the non-longitudinal modes. Excellent agreement was observed for the axial, transverse, as well as the mixed modes. The novel jump or matching conditions used at the cross-sectional interface(s) are such that the analytically known dispersion relations governing the acoustic modes of ducts with discontinuities are consistently recovered. This is the reason for characterizing the linear modal analysis developed in this study as acoustically consistent.

Building upon the detailed acoustical analysis, combustion instabilities of a 2-D cartesian dump combustor are investigated. Conventionally, to determine the unstable modes, the homogeneous acoustic wave equation is solved for the acoustic fluctuations, and the effects of combustion are incorporated *a posteriori* using an explicit energy matching condition across the flame. In this study, a novel approach is presented in which the inhomogeneous wave equation with the fluctuating heat-release source term is directly solved. As a result, the combustion effects are incorporated

into the modified axial wavenumbers in the combustion region, thereby obviating the need for applying an energy matching condition across a presumed 1-D planar flame. This approach is validated using the study of Yu et al. [2], who studied the combustion instability of a dump combustor using both experiments and a 1-D linear modal analysis. It is seen that the current predictions show good agreement with the Yu et al. experiments. Finally, the effects of a wide range of parameters on combustion instability have been studied, including mean flow Mach number, cross-sectional area ratio, flame length, and the time-lag between the acoustic and heat-release fluctuations in the flame response function.

2.3 Theory

In linear modal analysis of acoustics and combustion instabilities, the fundamental governing equation is the acoustic wave equation (Eq. (1.10)). We begin by considering a generic, linear inhomogeneous acoustic wave equation of the form

$$\frac{1}{\bar{c}^2}\frac{\overline{D}^2 p'}{\overline{Dt}^2} - \nabla^2 p' = f \tag{2.1}$$

where

$$\frac{\overline{D}}{\overline{Dt}} = \frac{\partial}{\partial t} + \overline{\mathbf{u}} \bullet \boldsymbol{\nabla},$$

$\overline{\mathbf{u}}$ is the mean velocity vector, p' represents the acoustic pressure oscillations, $\bar{c}$ is the mean speed of sound, and f is a generic linear source term that may include effects such as non-uniform mean flow and fluctuating heat release. For the purposes of

16

linear modal analysis, mean flow is considered to be in the axial (x-)direction, i.e. $\overline{\mathbf{u}} = \overline{u}(y)\,\widehat{\mathbf{e}}_x$, where $\overline{u}(y)$ accounts for non-uniform mean velocity such as the laminar parabolic profile or turbulent power-law profile.

Most combustion instability studies only consider the homogeneous form of Eq. (2.1), which imposes two significant restrictions. First, such an approach would mean that one can only consider a uniform mean flow. Second and more important in the context of predicting combustion instabilities, an explicit "energy matching condition" will have to be employed across the flame. The use of the energy matching condition restricts the flame shape to a few idealized forms—e.g., a 1-D planar flame occurring at a specified axial location. The planar flame approach, in turn, is based on the compact flame assumption. In our approach, we avoid both the above restrictions by directly solving the inhomogeneous wave equation Eq. (2.1) with the appropriate source term(s). The most significant advantage of this approach is that source terms due to non-uniform mean flow and to fluctuating heat release are directly incorporated into the axial wavenumber, obviating the need for a separate energy matching condition.

The theory section consists of two main parts: Acoustics (Section 2.3.1), and Combustion Instabilities (Section 2.3.2). In the discussion on acoustics (Section 2.3.1), we begin by presenting the generic forms of acoustic fluctuations for a 2-D cartesian duct, but without specifying the form of the axial wavenumbers in these fluctuations. This is because axial wavenumbers depend on the nature of inhomogeneity (or the source term) in the acoustic wave equation. Subsequently, the specific forms of axial wavenumbers are presented for cases with uniform and non-uniform

17

mean velocity profiles. This is followed by the linear modal analysis to determine the acoustics of two ducts with one and two discontinuities in cross-section. A detailed discussion on the "edge conditions" accounting for the velocity singularities at the corners of the cross-sectional interface(s) is also presented. In the section on combustion instabilities (Section 2.3.2), the approach for the acoustically consistent combustion instability analysis of a 2-D dump combustor is presented, where in the wave equation with the fluctuating heat-release source term is considered. A flame response function is used to relate the fluctuating heat release to the fluctuating axial velocity, but with a time-lag. In solving the wave equation, a modified axial wavenumber is derived that accounts for heat release fluctuations in the combustion zone.

2.3.1 Acoustics

2.3.1.1 Generic Acoustic Fluctuation Forms

Acoustic pressure fluctuations in a 2-D cartesian, uniform cross-section duct can be written as

$$p'(x,y,t) = e^{i\Omega t} \sum_{n=0}^{\infty} \left(A_n^+ e^{ik_n^+ x} + A_n^- e^{ik_n^- x} \right) \cos\left(\frac{2n\pi}{S} y \right) \tag{2.2}$$

where n is the transverse mode index, $A_n^{\pm}$ and $k_n^{\pm}$ are the amplitudes and axial wavenumbers, respectively, of the waves propagating in the positive and negative x-direction, and S is the duct height.

Density fluctuations (ρ') due to p' are given by

$$\rho'(x,y,t) = \frac{p'(x,y,t)}{\bar{c}^2} = \frac{1}{\bar{c}^2}e^{i\Omega t}\sum_{n=0}^{\infty}\left(A_n^+ e^{ik_n^+ x} + A_n^- e^{ik_n^- x}\right)\cos\left(\frac{2n\pi}{S}y\right) \qquad (2.3)$$

The axial component of fluctuating velocity $u'(x,y,t)$ can be derived from the linearized (inviscid) axial momentum equation:

$$\frac{\partial u'}{\partial t} + \bar{u}\frac{\partial u'}{\partial x} = -\frac{1}{\rho}\frac{\partial p'}{\partial x} \qquad (2.4)$$

Using Eq. (2.2) in (Eq. (2.4)), $u'(x,y,t)$ can be obtained as

$$u'(x,y,t) = -\frac{1}{\rho}\,e^{i\Omega t}\sum_{n=0}^{\infty}\left(\frac{k_n^+}{\Omega + \bar{u}k_n^+}A_n^+ e^{ik_n^+ x} + \frac{k_n^-}{\Omega + \bar{u}k_n^-}A_n^- e^{ik_n^- x}\right)\cos\left(\frac{2n\pi}{S}y\right) \quad (2.5)$$

Similarly, the transverse component of velocity fluctuations $v'(x,y,t)$ can be derived from the linearized transverse momentum equation:

$$\frac{\partial v'}{\partial t} + \bar{u}\frac{\partial v'}{\partial x} = -\frac{1}{\rho}\frac{\partial p'}{\partial y} \qquad (2.6)$$

giving us

$$v'(x,y,t) = \frac{1}{\rho}\,e^{i\Omega t}\sum_{n=0}^{\infty}\left(\frac{1}{\Omega + \bar{u}k_n^+}A_n^+ e^{ik_n^+ x} + \frac{1}{\Omega + \bar{u}k_n^-}A_n^- e^{ik_n^- x}\right)\frac{2n\pi}{S}\sin\left(\frac{2n\pi}{S}y\right)$$

$$(2.7)$$

Equations Eq. (2.2), Eq. (2.3), Eq. (2.5) and Eq. (2.7) represent the generic forms of acoustic fluctuations whose axial wavenumbers, $k_n^{\pm}$, are yet unknown. The

forms of $k_n^\pm$ depend upon the specific inhomogeneity in the wave equation Eq. (2.1), and are demonstrated below for various cases.

2.3.1.2 Acoustic Fluctuations with Uniform Mean Flow

For the case of uniform axial mean flow without combustion, Eq. (2.1) can be written in 2-D cartesian coordinates as [4]

$$\frac{1}{\overline{c}^2}\frac{\partial^2 p'}{\partial t^2} + \frac{2\overline{M}}{\overline{c}}\frac{\partial^2 p'}{\partial t \partial x} + (\overline{M}^2 - 1)\frac{\partial^2 p'}{\partial x^2} - \frac{\partial^2 p'}{\partial y^2} = 0 \tag{2.8}$$

where $\overline{M} = \overline{u}/\overline{c}$ is the mean flow Mach number. Equation Eq. (2.8) can be solved for p' using separation of variables along with the hard-wall boundary conditions in the transverse direction, i.e. $dp'/dy = 0$ at $y = \pm S/2$, where S is the duct height. This gives us the form of p' as shown in Eq. (2.2), where the axial wavenumbers specific to uniform mean flow are

$$k_n^\pm = \frac{\frac{\Omega \overline{M}}{\overline{c}} \mp \sqrt{\frac{\Omega^2}{\overline{c}^2} - (1 - \overline{M}^2)(\frac{2n\pi}{S})^2}}{1 - \overline{M}^2} \tag{2.9}$$

Equations Eq. (2.2), Eq. (2.3), Eq. (2.5) and Eq. (2.7) coupled with Eq. (2.9) provide the forms of p', ρ', u' and v' for the case of uniform mean flow.

2.3.1.3 Acoustic Fluctuations with Non-Uniform Mean Flow

In this section, we derive the specific form of the axial wavenumbers for the case of non-uniform axial mean flow. For this case, wave equation Eq. (2.1) becomes

$$\frac{1}{\bar{c}^2}\frac{\partial^2 p'}{\partial t^2} + \frac{2\overline{M}(y)}{\bar{c}}\frac{\partial^2 p'}{\partial t\partial x} + \left[\overline{M}^2(y) - 1\right]\frac{\partial^2 p'}{\partial x^2} - \frac{\partial^2 p'}{\partial y^2} = 2\bar{\rho}\frac{d\bar{u}}{dy}\frac{\partial v'}{\partial x} \tag{2.10}$$

where $\bar{u} = \bar{u}(y)$ and consequently $\overline{M} = \overline{M}(y)$. Two mean velocity profiles, namely laminar parabolic and turbulent power-law profiles, are considered.

First, we present the derivation for the case of laminar parabolic velocity profile given by

$$\bar{u}(y) = \alpha\left(\frac{S^2}{4} - y^2\right) \tag{2.11}$$

Here $\alpha = 6\,\overline{M}_{\text{bulk}}\,\bar{c}/S^2$, where $\overline{M}_{\text{bulk}}$ is the mean Mach number based on the bulk mass flow. We substitute into Eq. (2.10) the mean velocity profile given by Eq. (2.11), as well as the following fluctuation forms:

$$p' = e^{i\Omega t}\,A_n\,e^{ik_n x}\cos\left(k_y y\right) \tag{2.12}$$

$$\rho' = \frac{1}{\bar{c}^2}e^{i\Omega t}\,A_n\,e^{ik_n x}\cos\left(k_y y\right) \tag{2.13}$$

$$u' = -\frac{1}{\bar{\rho}}e^{i\Omega t}\,\frac{k_n}{\Omega + \bar{u}k_n}\,A_n\,e^{ik_n x}\cos\left(k_y y\right) \tag{2.14}$$

$$v' = \frac{1}{\bar{\rho}}e^{i\Omega t}\,\frac{1}{\Omega + \bar{u}k_n}\,A_n\,e^{ik_n x}\,k_y\,\sin\left(k_y y\right) \tag{2.15}$$

where k_n is the axial wavenumber to be determined and $k_y = \frac{2n\pi}{S}$ is the wavenumber of the nth transverse mode. The above substitutions yield the following equation for

k_n:

$$\cos(k_y y)\left(k_n^2 + k_y^2 - \frac{\Omega^2}{\bar{c}^2} - \frac{k_n \Omega S^2 \alpha}{2\bar{c}^2} - \frac{S^4 k_n^2 \alpha^2}{16\bar{c}^2}\right)$$
$$+\cos(k_y y)\left(\frac{2k\Omega\alpha y^2}{\bar{c}^2} + \frac{S^2 k_n^2 \alpha^2 y^2}{2\bar{c}^2} - \frac{k_n^2 \alpha^2 y^4}{\bar{c}^2}\right) =$$
$$\sin(k_y y)\left[\frac{-4ik_n k_y y}{\Omega + \alpha\left(\frac{S^2}{4} - y^2\right)k_n}\right] \tag{2.16}$$

It can be seen from Eq. (2.16) that for uniform mean flow, we recover Eq. (2.9). For non-uniform mean flow and $n = 0$ (i.e., for purely axial modes), Eq. (2.16) is quadratic in the axial wavenumber k_n, which can be solved to yield:

$$k_0^{\pm} = \frac{\frac{\Omega \overline{M}_{\text{bulk}}}{\bar{c}} \mp \sqrt{\frac{\Omega^2}{\bar{c}^2}\left(1 - \frac{1}{5}\overline{M}_{\text{bulk}}^2\right)}}{1 - \frac{6}{5}\overline{M}_{\text{bulk}}} \tag{2.17}$$

By comparing Eq. (2.17) with Eq. (2.9) for $n = 0$, one can see the effects of the laminar parabolic profile on the wavenumbers of the purely axial modes. For $n \neq 0$, to solve for k_n, we multiply Eq. (2.16) with $\cos(k_y y)$ and integrate from $-\frac{S}{2}$ to $\frac{S}{2}$. Subsequently, on the LHS of Eq. (2.16), we utilize the orthogonality of the cosine function, but the integration on the RHS can only be performed numerically. Therefore, the expression for k_n when $n \neq 0$ is not explicitly provided here.

The procedure discussed above is also used to compute the axial wavenumbers for the turbulent mean velocity profile given by

$$\overline{u}(y) = \overline{M}_{\text{bulk}}\,\bar{c}\left(1 - \frac{4y^2}{S^2}\right)^{\frac{1}{7}} \tag{2.18}$$

22

Equations Eq. (2.2), Eq. (2.3), Eq. (2.5) and Eq. (2.7) coupled with the axial wavenumbers derived above provide the forms of p', ρ', u' and v' for the case of non-uniform mean flow. The effects of including non-uniform mean flow on duct acoustics are demonstrated in Section 2.4.1.4 for both the laminar and turbulent mean velocity profiles. It will be seen that for a given bulk mean Mach number, there is not a significant difference between the acoustic mode predictions for the uniform and non-uniform mean flow cases. This conclusion is particularly significant when predicting combustion instabilities.

We now discuss the modal analysis for determining the acoustic modes of ducts with discontinuities. This *a priori* acoustics exercise is crucial in order to have confidence in the subsequent combustion instability analysis.

2.3.1.4   Fluctuations Forms for Ducts with Discontinuities

Ducts with one and two discontinuities in cross-section, shown in Figs. Figure 2.1 and Figure 2.2 respectively, are considered for the acoustic analysis. These duct configurations were chosen so as to compare our modal predictions with the analytical and numerical data of Meissner [1].
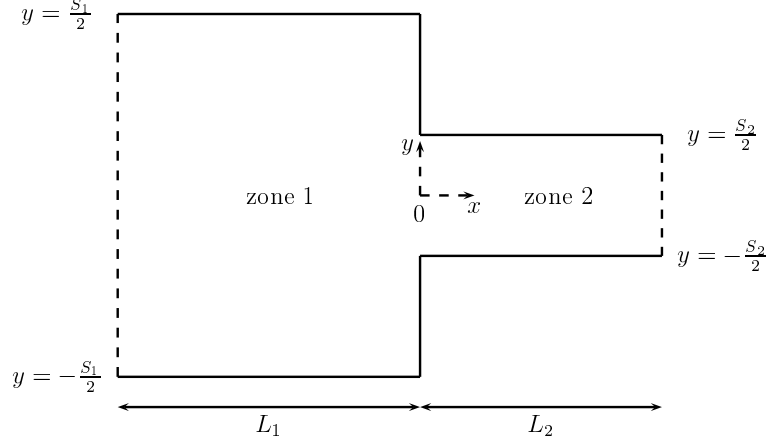
Figure 2.1: Geometry of duct with single discontinuity. Duct dimensions $L_1 = 0.3$m and $L_2 = 0.7$m are chosen from Meissner [1]. Coordinate axes are also shown.

Duct with Single Discontinuity

The pressure, density and velocity fluctuations for the duct in Fig. Figure 2.1 are:

$$
p'_\beta(x,y,t) = e^{i\Omega t} \sum_{n=0}^{\infty} \left(A^+_{n,\beta} e^{ik^+_{n,\beta}x} + A^-_{n,\beta} e^{ik^-_{n,\beta}x} \right) \cos\left(\frac{2n\pi}{S_\beta} y \right)
$$

$$
\rho'_\beta(x,y,t) = \frac{1}{\bar{c}_\beta^2} e^{i\Omega t} \sum_{n=0}^{\infty} \left(A^+_{n,\beta} e^{ik^+_{n,\beta}x} + A^-_{n,\beta} e^{ik^-_{n,\beta}x} \right) \cos\left(\frac{2n\pi}{S_\beta} y \right)
$$

$$
u'_\beta(x,y,t) = -\frac{1}{\bar{\rho}_\beta} e^{i\Omega t} \sum_{n=0}^{\infty} \left(\frac{k^+_{n,\beta}}{\Omega + \bar{u}_\beta k^+_{n,\beta}} A^+_{n,\beta} e^{ik^+_{n,\beta}x} + \frac{k^-_{n,\beta}}{\Omega + \bar{u}_\beta k^-_{n,\beta}} A^-_{n,\beta} e^{ik^-_{n,\beta}x} \right) \cos\left(\frac{2n\pi}{S_\beta} y \right)
$$

$$
v'_\beta(x,y,t) = \frac{1}{\bar{\rho}_\beta} e^{i\Omega t} \sum_{n=0}^{\infty} \left(\frac{\beta}{\Omega + \bar{u}_\beta k^+_{n,\beta}} A^+_{n,\beta} e^{ik^+_{n,\beta}x} + \frac{\beta}{\Omega + \bar{u}_\beta k^-_{n,\beta}} A^-_{n,\beta} e^{ik^-_{n,\beta}x} \right) \frac{2n\pi}{S_\beta} \sin\left(\frac{2n\pi}{S_\beta} y \right)
$$

$$
(2.19)
$$

where $\beta = 1, 2$ is the zonal index.

As discussed in the previous sections, the axial wavenumbers $k^\pm_{n,\beta}$ will assume the appropriate form depending upon the nature of the source term in the wave equation. The unknown coefficients in Eq. (2.19) are $A^\pm_{n,\beta}$, $\beta = 1, 2$.
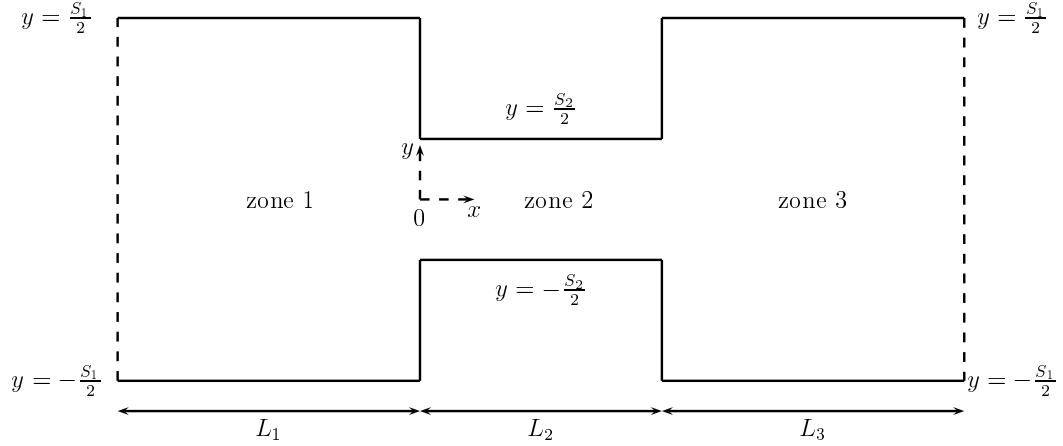
Figure 2.2: Geometry of duct with two discontinuities. Duct dimensions are $L_1 = 0.475$m, $L_2 = 0.05$m and $L_3 = 0.520$m (Meissner [1]). Coordinate axes are also shown.

Duct with Two Discontinuities

The fluctuating pressure, density and velocity in zones 1, 2 and 3 (see Figure 2.2) are similar to those in Eqs. (2.19). The unknown coefficients for this case are $A_{n,\beta}^{\pm}$, with $\beta = 1, 2, 3$. The necessary equations to solve for the unknown coefficients are obtained from the various boundary and matching conditions. Since the imperme-ability boundary condition in the transverse direction has already been applied (see Eq. (2.2)), we have at our disposal the inlet and exit boundary conditions, as well as the matching conditions at zonal interfaces.

2.3.1.5 Edge Conditions

The velocity fluctuation forms in Eq. (2.19) are fundamentally valid for uniform cross-section ducts. Therefore, when using these forms for ducts with discontinuities, one has to impose additional constraints at the zonal interface(s) (see Figure 2.1 and Figure 2.2). For the duct in Figure 2.1, u_1' and v_1' should satisfy the following interface

boundary conditions in addition to the hard-wall boundary condition at $y = \pm S_1/2$:

$$u_1'(0^-, y) = 0, \quad y \in \left[\frac{S_2}{2}, \frac{S_1}{2}\right] \text{ and } y \in \left[-\frac{S_1}{2}, -\frac{S_2}{2}\right] \tag{2.20}$$

$$v_1'(0^-, y) = 0, \quad y \in \left[\frac{S_2}{2}, \frac{S_1}{2}\right] \text{ and } y \in \left[-\frac{S_1}{2}, -\frac{S_2}{2}\right] \tag{2.21}$$

$$u_1'(0, y) = u_2'(0, y), \quad y \in \left[-\frac{S_2}{2}, \frac{S_2}{2}\right] \tag{2.22}$$

Further, the following edge conditions should also be satisfied at the interface corner points in Figure 2.1:

$$u_1'\left(0, \pm\frac{S_2}{2}\right) = u_2'\left(0, \pm\frac{S_2}{2}\right) = 0 \tag{2.23}$$

$$v_1'\left(0, \pm\frac{S_2}{2}\right) = v_2'\left(0, \pm\frac{S_2}{2}\right) = 0 \tag{2.24}$$

Satisfying the edge conditions is necessary in order to obtain a unique fluctuating velocity field at the interface [15]. It is evident that the fluctuation forms in Eq. (2.19) do not satisfy the above constraints Eq. (2.20)-Eq. (2.24).

According to Mittra and Lee [16], the criterion for a fluctuating field quantity to be consistent with the edge condition is that the integral of the field energy in the neighborhood of the interface corner point be finite. This criterion can be written as

$$\int_V |\mathbf{u}|^2 \, dV \to 0 \text{ as } \sigma \to 0 \tag{2.25}$$

where σ is the distance from the edge (see Figure 2.3), $\mathbf{u}$ is the velocity vector, and the differential volume $dV = \sigma d\sigma d\phi dz$ is defined in terms of local cylindrical coordinates with the edge as the origin.
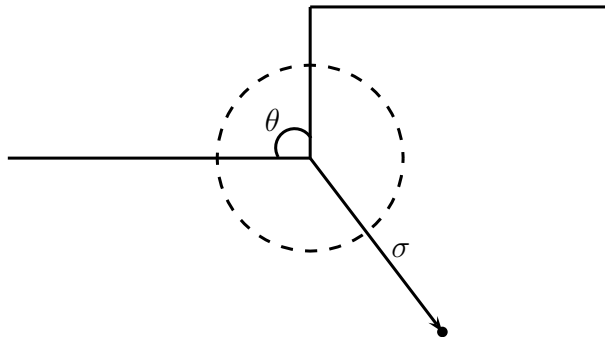
Figure 2.3: Corner of an interface where edge condition is applied.

Mittra and Lee [16] showed that the implication of Eq. (2.25) is that the fluctuating velocities u' and v' should not grow more rapidly than $\sigma^{-1+\eta}$ as $\sigma \to 0$, where $\eta > 0$ is determined by the internal wedge angle θ as shown in Figure 2.3. Therefore, for the solution to converge

$$u'(\sigma),\ v'(\sigma) \sim O(\sigma^{-1+\eta})$$

Collins [17] provided an the expression for η in case of a wedge with an internal angle θ as

$$\eta = \frac{\pi}{2\pi - \theta}$$

For the ducts under consideration, $\theta = \frac{\pi}{2}$, hence $\eta = \frac{2}{3}$. Therefore

$$u'(\sigma), \ v'(\sigma) \sim O(\sigma^{-\frac{1}{3}})$$

In order that the interface boundary and edge conditions are satisfied, Hermentcov-schi and Miles [15] rewrote the interface velocity using Gegenbauer polynomials as the basis functions in the y-direction since these polynomials are naturally defined in the interval $y \in [-1, 1]$, and can be scaled to $y \in [-S_1/2, S_1/2]$. It is, how-ever, not necessary that one replace the Fourier basis functions with the Gegenbauer polynomials. In fact, it can be shown that the above additional constraints can be satisfied by appropriately modifying the amplitudes only—e.g., by modifying $A_{n,\{1,2\}}^{\pm}$ in Eq. (2.19) [16, 18, 19]. This is rigorously demonstrated in Appendix A. The pre-ceding realization is important in the context of a linear modal analysis where the final assembled system of equations is homogeneous, and one is only interested in the dispersion relation obtained by equating the determinant of the coefficient matrix to zero, i.e. one does not explicitly solve for the amplitudes. Consequently, the modified amplitudes do not impact the overall linear stability analysis. However, one has to be mindful of the edge conditions when performing a non-linear analysis.

2.3.1.6 Zonal Matching Conditions

This section presents the acoustically consistent matching conditions that are applied at the interface(s) between zones in a duct with discontinuities in cross-section. There are important differences between the matching conditions used in

the current study and those used conventionally in combustion instability studies. Firstly, in order to be acoustically consistent, separate matching conditions are applied for the purely axial modes, and the non-axial (transverse and mixed) modes [20]. By acoustical consistency, we mean that by using the current matching conditions, one consistently recovers the analytical dispersion relations governing the purely axial modes for ducts with discontinuities. Secondly, the current matching conditions eliminate the problem of overdetermined system of equations, i.e. a situation where the number of matching and boundary conditions exceeds the number of unknown amplitudes. This predicament arises when the momentum conservation matching condition is applied at the zonal interface, which gives rise to three equations when only one is needed. Thirdly, an explicit energy matching condition is not needed since the wave equation is directly solved with the heat release source term included in it.

Acoustic Velocity Matching

Velocity matching condition for the purely axial modes is prescribed in terms of the continuity of acoustic mass velocity V [20, 21], which is defined as

$$V = \int_S \rho u \, dy \tag{2.26}$$

where ρ and u are instantaneous density and streamwise velocity, respectively. The continuity of mass velocity at the interface between zones 1 and 2 is given by

$$\int_{S_1} \rho_1 u_1 \, dy = \int_{S_2} \rho_2 u_2 \, dy \tag{2.27}$$

Linearizing Eq. (2.27) yields

$$\int_{S_1} [\rho_1' \bar{u}_1 + \bar{\rho}_1 u_1'] \, dy = \int_{S_2} [\rho_2' \bar{u}_2 + \bar{\rho}_2 u_2'] \, dy \tag{2.28}$$

It is to be noted that when a fluctuating quantity is integrated over the cross-section of the corresponding zone, e.g. u_1' is integrated over S_1 ($\int_{S_1} u_1' \, dy$), only the zeroth-mode (purely axial) contribution remains. Accordingly, the velocity matching condition for the purely axial modes is given by:

$$[\rho_1^{(0)} \, \bar{u}_1 + \bar{\rho}_1 \, u_1^{(0)}] \, S_1 = [\rho_2^{(0)} \, \bar{u}_2 + \bar{\rho}_2 \, u_2^{(0)}] \, S_2 \tag{2.29}$$

where the superscript (0) represents the zeroth mode ($n = 0$) of a fluctuating quantity. Writing Eq. (2.29) in terms of the amplitudes gives the following form of the velocity matching condition for the purely axial modes.

$$
\begin{aligned}
S_1 &\left\{ \left(\frac{\overline{M}_1}{\bar{c}_1} - \frac{k_{0,1}^+}{\Omega + \bar{u}_1 k_{0,1}^+} \right) e^{i k_{0,1}^+ x} A_{0,1}^+ + \left(\frac{\overline{M}_1}{\bar{c}_1} - \frac{k_{0,1}^-}{\Omega + \bar{u}_1 k_{0,1}^-} \right) e^{i k_{0,1}^- x} A_{0,1}^- \right\} = \\
S_2 &\left\{ \left(\frac{\overline{M}_2}{\bar{c}_2} - \frac{k_{0,2}^+}{\Omega + \bar{u}_2 k_{0,2}^+} \right) e^{i k_{0,2}^+ x} A_{0,2}^+ + \left(\frac{\overline{M}_2}{\bar{c}_2} - \frac{k_{0,2}^-}{\Omega + \bar{u}_2 k_{0,2}^-} \right) e^{i k_{0,2}^- x} A_{0,2}^- \right\}
\end{aligned}
\tag{2.30}
$$

For the non-axial modes, the acoustic velocity matching condition at the zonal interface is inspired by the pioneering study of Karal [20], who investigated acoustical impedances in waveguides with cross-sectional discontinuities. Based on Karal [20], one can write the velocity matching condition for non-axial modes as

$$u_1' = u_2' \tag{2.31}$$

30

It is relevant to mention here that prior works have applied an alternative set of matching conditions based on the conservation of mass and axial momentum over a differential control volume spanning the interface. A brief derivation of this alternative approach and a discussion of its implications are provided in Appendix B. However, Eq. (2.31) is more rigorous since it ensures the uniqueness of both the mean and fluctuating velocities at the interface. Equation Eq. (2.31) contains an infinite series summation on both the LHS and RHS. We reduce this complexity by utilizing the orthogonality property of the cosine function. Multiplying Eq. (2.28) with $\cos\left(\frac{2N\pi}{S_1}y\right)$ ($N > 0$ is an integer), and integrating over $y \in [-S_1/2, S_1/2]$ yields

$$
\frac{S_1}{2} \left\{ \left(\frac{k_{N,1}^+}{\Omega + \overline{u}_1 k_{N,1}^+}\right) e^{ik_{N,1}^+ x} A_{N,1}^+ + \left(\frac{k_{N,1}^-}{\Omega + \overline{u}_1 k_{N,1}^-}\right) e^{ik_{N,1}^- x} A_{N,1}^- \right\} =
$$
$$
\sum_{n=0}^{N} \alpha_n \left\{ \left(\frac{k_{n,2}^+}{\Omega + \overline{u}_2 k_{n,2}^+}\right) e^{ik_{n,2}^+ x} A_{n,2}^+ + \left(\frac{k_{n,2}^-}{\Omega + \overline{u}_2 k_{n,2}^-}\right) e^{ik_{n,2}^- x} A_{n,2}^- \right\}
$$

(2.32)

where

$$
\alpha_n = \int_{-\frac{S_1}{2}}^{\frac{S_1}{2}} \cos\left(\frac{2n\pi}{S_2}y\right) \cos\left(\frac{2N\pi}{S_1}y\right) \, dy
$$

(2.33)

Equation Eq. (2.32) is the final form of the velocity matching condition for the non-axial modes.

Acoustic Pressure Matching

Acoustic pressure matching is achieved through the continuity of the total pressure (static + dynamic) at the zonal interfaces [21]. Again, separate matching conditions are needed for the purely axial and non-axial modes.

For the axial modes, the pressure matching condition (for the duct in Figure 2.1) is written as [20]

$$\int_{S_1} \left\{ p_1 + \frac{1}{2}\rho_1 u_1^2 \right\} dy = \int_{S_1} \left\{ p_2 + \frac{1}{2}\rho_2 u_2^2 \right\} dy \tag{2.34}$$

which upon linearization yields

$$\int_{S_1} \left\{ p_1' + \overline{\rho}_1 \, \overline{u}_1 \, u_1' + \frac{1}{2}\rho_1' \, \overline{u}_1 \, \overline{u}_1 \right\} dy = \int_{S_1} \left\{ p_2' + \overline{\rho}_2 \, \overline{u}_2 \, u_2' + \frac{1}{2}\rho_2' \, \overline{u}_2 \, \overline{u}_2 \right\} dy \tag{2.35}$$

Substituting the appropriate fluctuating forms into the above equation and integrating results in different behaviors on the LHS and RHS. On the LHS of Eq. (2.35), only the zeroth mode terms remain since the fluctuating quantities in zone 1 are being integrated across S_1; whereas on the RHS, fluctuations in zone 2 are being integrated across S_1. Consequently, both purely axial ($n = 0$) and non-axial modes ($n \neq 0$) contribute to the RHS.

For the purely axial modes, the pressure matching condition is obtained by retaining only the $n = 0$ terms on the RHS of Eq. (2.35), as follows:

$$\begin{aligned}
\left(\frac{\overline{M}_1^2}{2} + 1 - \overline{u}_1 \frac{k_{0,1}^+}{\Omega + \overline{u}_1 k_{0,1}^+} \right) A_{0,1}^+ + \left(\frac{\overline{M}_1^2}{2} + 1 - \overline{u}_1 \frac{k_{0,1}^-}{\Omega + \overline{u}_1 k_{0,1}^-} \right) A_{0,1}^- = \\
\left(\frac{\overline{M}_2^2}{2} + 1 - \overline{u}_2 \frac{k_{0,2}^+}{\Omega + \overline{u}_2 k_{0,2}^+} \right) A_{0,2}^+ + \left(\frac{\overline{M}_2^2}{2} + 1 - \overline{u}_2 \frac{k_{0,2}^-}{\Omega + \overline{u}_2 k_{0,2}^-} \right) A_{0,2}^-
\end{aligned} \tag{2.36}$$

For the non-axial modes, the acoustic pressure matching condition is given by [21]

$$p_1 + \frac{1}{2}\rho_1 u_1^2 = p_2 + \frac{1}{2}\rho_2 u_2^2 \tag{2.37}$$

which upon linearization can be written as

$$p_1' + \overline{\rho}_1\,\overline{u}_1\,u_1' + \frac{1}{2}\rho_1'\,\overline{u}_1\,\overline{u}_1 = p_2' + \overline{\rho}_2\,\overline{u}_2\,u_2' + \frac{1}{2}\rho_2'\,\overline{u}_2\,\overline{u}_2 \tag{2.38}$$

Substituting the appropriate fluctuation forms, multiplying Eq. (2.38) with $\cos\left(\frac{2N\pi}{S_1}y\right)$ ($N > 0$ is an integer), and integrating over y across the cross-section S_1 yields

$$\frac{S_1}{2}\left\{\left(\frac{\overline{M}_1^2}{2} + 1 - \overline{u}_1\frac{k_{N,1}^+}{\Omega + \overline{u}_1 k_{N,1}^+}\right)A_{N,1}^+ + \left(\frac{\overline{M}_1^2}{2} + 1 - 2\overline{u}_1\frac{k_{N,1}^-}{\Omega + \overline{u}_1 k_{N,1}^-}\right)A_{N,1}^-\right\} =$$
$$\sum_{n=0}^{N}\alpha_n\left\{\left(\frac{\overline{M}_2^2}{2} + 1 - \overline{u}_2\frac{k_{n,2}^+}{\Omega + \overline{u}_2 k_{n,2}^+}\right)A_{n,2}^+ + \left(\frac{\overline{M}_2^2}{2} + 1 - \overline{u}_2\frac{k_{n,2}^-}{\Omega + \overline{u}_2 k_{n,2}^-}\right)A_{n,2}^-\right\} \tag{2.39}$$

where α_n is same as that in Eq. (2.33). The matching conditions are similarly formulated for zones 2 and 3 of the two-discontinuity duct (see Figure 2.2).

2.3.1.7   Inlet and Exit Boundary Conditions

In this study we considered three kinds of boundary conditions (BCs): closed, open and choked. *Closed boundary condition* is where the normal (to the boundary) derivative of pressure is zero: $\frac{dp'}{dx} = 0$. *Open boundary condition* is a specified pressure boundary condition. This means that pressure fluctuations at this boundary are zero: $p' = 0$. *Choked boundary condition* is used when the flow is choked at the outlet, and

is given by [4]: $\frac{2u'}{\bar{u}} + \frac{\rho'}{\bar{\rho}} - \frac{p'}{\bar{p}} = 0$. After utilizing the matching conditions, we apply the chosen boundary condition at the inlet/outlet boundary. The BCs are then simplified into algebraic equations using the orthogonality property.

2.3.1.8 Equation Assembly and Solution

The matching and boundary conditions are assembled to get a homogeneous matrix system of equations of the form $\mathbf{CA} = \mathbf{0}$, where $\mathbf{C}$ is the coefficient matrix and $\mathbf{A}$ is the vector of unknowns containing the modal amplitudes $A_n^{\pm}$. A unique and non-trivial solution to $\mathbf{CA} = \mathbf{0}$ exists only when $\det(\mathbf{C}) = 0$, which gives us a dispersion relation that can be solved to obtain the modal frequencies. Next, we present the modal analysis to determine the combustion instabilities.

2.3.2 Combustion Instabilities

To predict combustion instabilities, we consider the inhomogeneous wave equation with the fluctuating heat-release source term [4]:

$$\frac{1}{\bar{c}^2}\frac{\overline{D}^2 p'}{\overline{D}t^2} - \nabla^2 p' = \frac{\gamma - 1}{\bar{c}^2}\frac{\overline{D}q'}{\overline{D}t} \tag{2.40}$$

where q' is the fluctuating volumetric heat-release rate. The fluctuating heat-release rate q' is expressed in terms of acoustic fluctuations using the flame response function (FRF) adopted from Dowling [5]. Incorporating an additional time-lag factor into

34

the FRF of Dowling [5] gives us

$$\frac{q'}{\overline{q}} = \frac{u'(t-\tau)}{\overline{u}} \tag{2.41}$$

where $\overline{q}$ is the mean volumetric heat release rate which is non-zero only in the combustion zone, $u'(t-\tau) = \exp(-i\Omega\tau)\, u'(t)$, and τ is the time-lag between the heat release (q') and velocity (u') perturbations. Substituting Eq. (2.41) into the RHS of Eq. (2.40) gives

$$\frac{\gamma-1}{\overline{c}^2}\frac{\overline{D}q'}{\overline{D}t} = \frac{\gamma-1}{\overline{c}^2}\overline{q}\left[\frac{1}{\overline{u}}\frac{\partial}{\partial t}u'(t-\tau) + \frac{\partial}{\partial x}u'(t-\tau)\right] \tag{2.42}$$

Before proceeding further with the combustion instability analysis, it is pertinent to discuss the combustor geometry under consideration. The geometry of the 2-D dump combustor is shown in Figure 3.1. The combustor is divided into three zones: an inflow zone (zone 1), the combustion zone (zone 2), and the outflow zone (zone 3). The mean flame shape being considered is shown in zone 2 in Figure 3.1. Therefore, the fluctuating heat release source term on the RHS of Eq. (2.40) is non-zero only in zone 2, and is absent in zones 1 and 3. We assume a uniform mean velocity profile, which is reasonable since it will be seen that for a given bulk mean Mach number, the mean velocity profile does not significantly affect the duct acoustics.

The acoustic fluctuation forms in zones 1 and 3 are known completely, and are given in Section 2.3.1.1, with the axial wavenumbers corresponding to those for a uniform mean flow. Our goal is to determine the modified axial wavenumbers

for the combsution zone (i.e. zone 2). To this end, we follow the same procedure as that outlined in Section 2.3.1.3. Substituting the fluctuation forms Eq. (2.12)-Eq. (2.15) into Eq. (2.40) and utilizing the orthogonality of the cosine function yields a quadratic equation governing the combustion-modified axial wavenumbers. The resulting modified wavenumbers that account for the heat release fluctuations are given by:

$$k_{n,2}^{\pm} = \frac{1}{2\overline{\rho}_2(\overline{c}_2^2 - \overline{u}_2^2)} e^{-i\Omega\tau}(G \mp H) \tag{2.43}$$

where G and H are given by

$$G = 2\overline{\rho}_2\overline{u}_2\Omega e^{i\Omega\tau} - i(\gamma - 1)\overline{q}$$

$$H = \sqrt{-\overline{q}^2(\gamma - 1)^2 - 4i\ \overline{q}\ \overline{\rho}_2\ \overline{u}_2\ \Omega\ e^{i\Omega\tau} - 4\ \overline{\rho}_2^2\ \overline{c}_2^2\ e^{2i\Omega\tau}(\overline{c}_2^2\ k_y^2 - \overline{u}_2^2\ k_y^2 - \Omega^2)}$$

and $k_y = 2n\pi/S_2$. The mean volumetric heat release rate, $\overline{q}$, for the mean flame shape under consideration is given by

$$\overline{q} = \frac{\overline{Q}}{S_2 L_f} \tag{2.44}$$

where $\overline{Q}$ is the total heat release rate is obtained by integrating over the flame surface area:

$$\overline{Q} = 2\overline{\rho}_2\overline{u}_2 c_p(\overline{T}_2 - \overline{T}_1) \int_0^{\frac{S_1}{2}} \left(y - \frac{S_1}{2}\right)\left(\frac{-2L_f}{S_1}\right)\ dy \tag{2.45}$$

Here $\overline{T}_1$, $\overline{T}_2$ are the mean temperatures in zones 1 and 2, $\overline{\rho}_2$ and $\overline{u}_2$ are the mean density and axial velocity in zone 2, and c_p is the specific heat at constant pressure. The factor 2 in Eq. (2.45) accounts for the flame above and below the duct centerline.
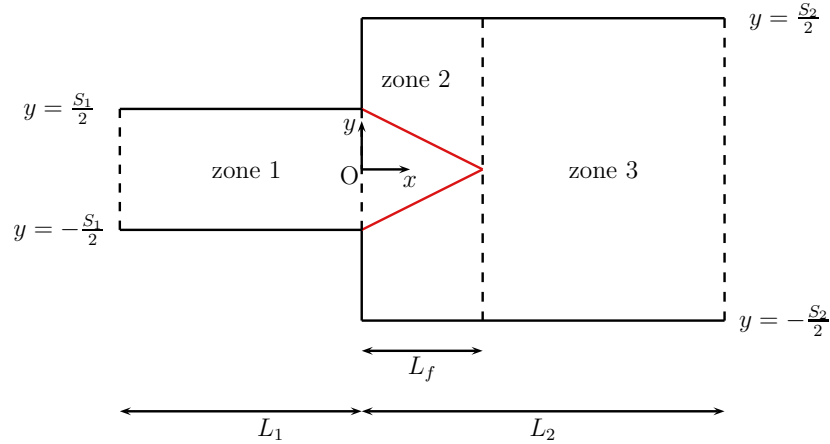
Figure 2.4: Geometry of the combustor with the mean flame shape indicated in red. Duct dimensions $L_1 = 0.3$m and $L_2 = 0.7$m. Coordinate axes are also shown.

2.4 Results

This section again consists of two main parts: (1) Acoustics (Section 2.4.1), and (2) Combustion Instabilities (Section 2.4.2). In the former, we present the results from the purely acoustical analysis of the two ducts under consideration. In the latter, we present the results from the combustion instability analysis of a dump combustor.

2.4.1 Acoustics

Motivated by the acoustics study of Meissner [1], two duct configurations were considered with one and two discontinuities in cross-sectional area. While Meissner only studied duct acoustics for closed-closed boundary conditions, i.e. with no mean

flow, this study also considered open-open (with and without mean flow). The various acoustic cases considered in this study are as follows:

- Case 1(a)–Single discontinuity duct with no mean flow and closed-closed boundary conditions (BCs) at the inlet and outlet.

- Case 1(b)–Single discontinuity duct with uniform mean flow and open-open BCs.

- Case 2–Two discontinuity duct with no mean flow and closed-closed BCs.

- Case 3–Single discontinuity duct with non-uniform mean flow and open-open BCs.

2.4.1.1   Case 1(a)

Here we consider a single discontinuity duct with no mean flow and closed-closed boundary conditions (BCs) at the inlet and outlet. The frequency space explored includes the first six axial modes ($\Omega_{1,0}$ to $\Omega_{6,0}$), the first transverse mode ($\Omega_{0,1}$) and the first oblique mode ($\Omega_{1,1}$). All frequencies are normalized with the fundamental axial mode Ω_0 of a uniform cross-section duct with the same length ($L_1 + L_2$) as the duct under consideration. Modal frequencies as a function of the cross-sectional area ratio S_2/S_1 are shown in Figure 2.5. Axial mode frequencies are compared with the analytical predictions of Meissner [1], while the transverse and oblique mode frequencies are compared with the numerical data of Meissner.

It can be seen from Figure 2.5 that the current axial modes are identical to those of Meissner. This is to be expected because for the purely axial modes,

dispersion relation obtained from $\det(\mathbf{C}) = 0$ is identical to that in Meissner's study, who used a 1-D impedance approach to determine the dispersion relation. The fifth axial mode (Ω_{50}) in Figure 2.5(c) is interesting as it does not depend on S_2/S_1. Meissner concluded that this is an artifact of the specific value of the zonal length ratio considered. Predictions of the transverse and oblique modes from the current theory also agree quite well with the corresponding numerical results of Meissner, with the peak deviation being less than 5%. One can conclude from Figure 2.5(a)-(d) that the cross-sectional area ratio has a significant effect on the longitudinal, transverse and oblique modes of the duct.

An interesting aspect that merits discussion is regarding the area ratio parameter S_2/S_1. It is clear that this ratio can be varied by decreasing or increasing S_2 and/or S_1. However, it can be shown that changing S_2/S_1 through a reduction of S_2 or S_1 prevents one from capturing the lower modes using modal analysis. This can be explained in terms of the cut-off frequency. Consider the axial wavenumber given by Eq. (2.9) with zero mean flow ($\overline{M} = 0$):

$$k_n^{\pm} = \mp\sqrt{\frac{\Omega^2}{\bar{c}^2} - \left(\frac{2n\pi}{S}\right)^2} \qquad (2.46)$$

where S is the zonal cross-sectional area of interest (S_2 or S_1) and n is the modal index. For a given value of n and S, there is a critical value of Ω below which the wavenumber ($k_n^{\pm}$) is purely imaginary. This frequency is called the cut-off frequency and is given by $\Omega_{\text{cut-off}} = \bar{c}\frac{2n\pi}{S}$.

It is clear from Eq. (2.46) that a reduction in S leads to an increase in the cut-off frequency, preventing one from capturing lower frequencies. This suggests that the ratio S_2/S_1 has to be changed by increasing either S_1 or S_2, and not by reducing either cross-sectional area. Therefore, in this study we chose to increase S_1. With increasing S_1, zone 1 acts like a large buffer that stabilizes the modes, thereby enabling us to mitigate the effects of cut-off frequency, as well as capture the modes of interest.
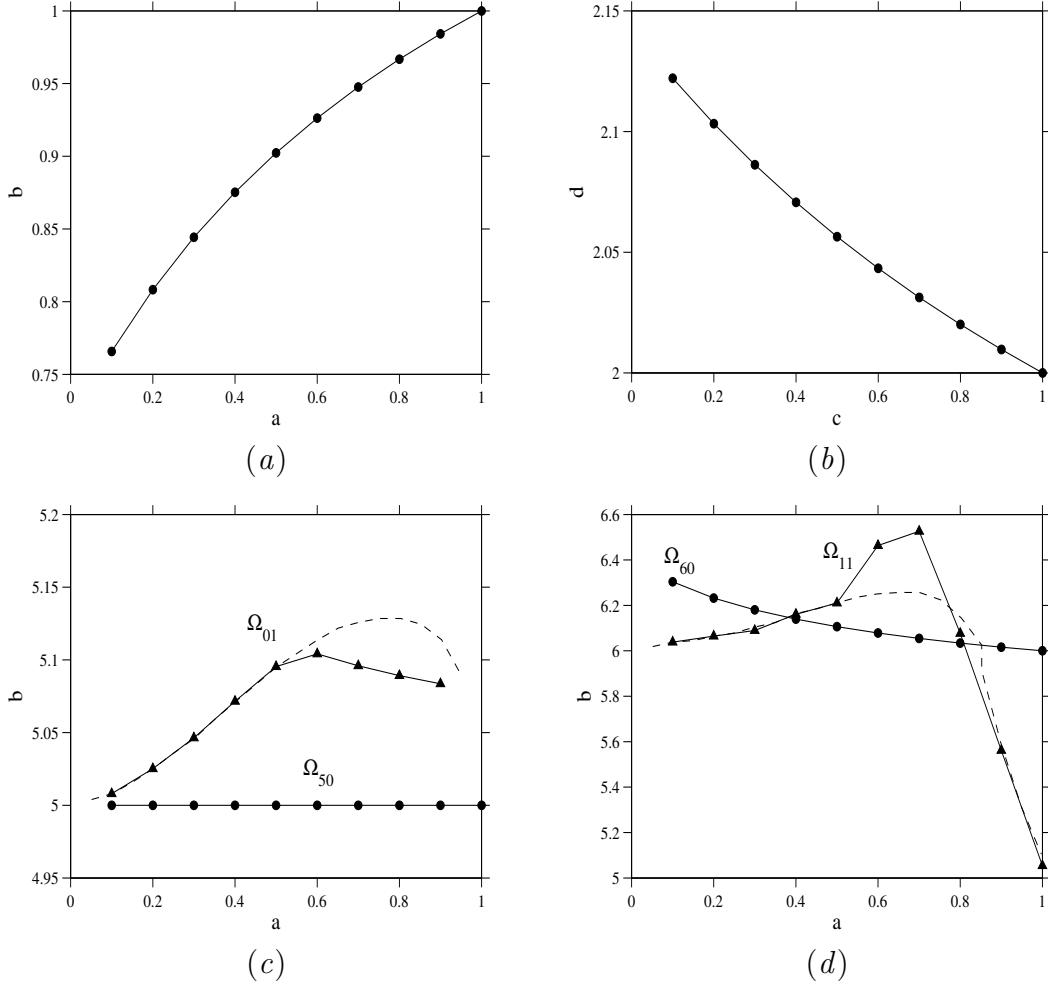
Figure 2.5: Comparison of modal predictions from the current theory with Meissner [1] for Case 1(a). Frequencies are normalized with the fundamental axial mode Ω_0 for a uniform cross-sectional duct of same length. (a) $\Omega_{1,0}$, (b) $\Omega_{2,0}$, (c) $\Omega_{5,0}$, (d) $\Omega_{6,0}$ and $\Omega_{1,1}$. —— Meissner's theoretical results for axial modes; - - - - Meissner's computational results for non-axial modes; • Current theoretical results for axial modes; ▲ Current theoretical results for non-axial modes.

2.4.1.2 Case 1(b)

This case investigates the effects of mean flow Mach number on the modal frequency predictions for a single discontinuity duct with open-open (inlet and outlet) boundary conditions. Results from only the current study are presented as Meissner's impedance-based approach did not include the mean flow. However, current results

41

are validated at one point, i.e., for $S_2/S_1 = 1$, where the axial mode frequencies can be analytically calculated as:

$$\Omega_n = (1 - \overline{M}^2)\overline{c}\frac{2n\pi}{S}. \tag{2.47}$$

where S is the constant cross-sectional area of the duct.

The inlet Mach numbers considered are $M = 0$, 0.01, 0.1, 0.2, 0.3. The upper limit for inlet Mach number is set at $M = 0.3$ because at higher mean flow velocities, the Mach number in zone 2 may approach unity at which point there is a singularity in the axial wavenumber (see Eq. (2.9)). The $M = 0.01$ case was chosen since modal frequencies for this Mach number should be nearly equal to those for $M = 0$. This was found to be the case thereby acting as an indirect validation of our approach.

The first and fourth axial modes are shown in Figure 2.6(a)-(b). It can be seen that the $M = 0$ and $M = 0.01$ curves almost overlap, as expected. Transverse and oblique modes are not presented due to the lack of validation data. It is evident from Figure 2.6 that the mean flow significantly impacts modal frequencies even at inflow Mach numbers as low as $M = 0.1$. For a given area ratio S_2/S_1, as the Mach number increases, there is a monotonic decrease in frequencies. This trend can be inferred from Eq. (2.47). The conclusion one can draw is that the neglect of mean flow in combustion systems can result in significant errors in the prediction of unstable modes. For a given inflow Mach number M_1, the Mach number in zone 2, M_2, increases as the area ratio S_2/S_1 decreases. For a certain value of S_2/S_1, $M_2 = 1$

which leads to a singularity in Eq.Eq. (2.9). The area ratios where the singularity occurs is indicated using vertical dashed lines in Figure 2.6(a).
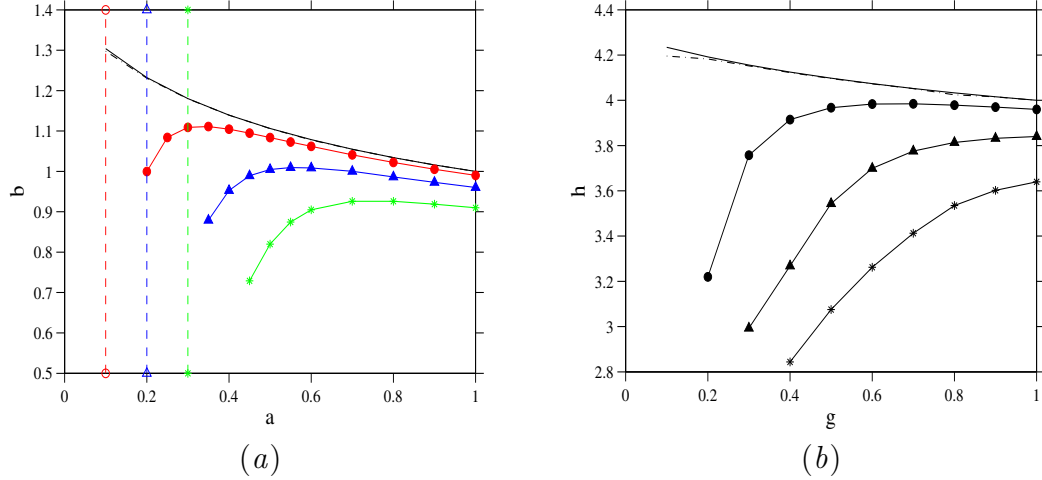
Figure 2.6: (color online) Axial mode predictions from the current theory for Case 1(b) as a function of mean inflow Mach number. Frequencies are normalized with the fundamental axial mode Ω_0 for a uniform cross-sectional duct of the same length. (a) $\Omega_{1,0}$, (b) $\Omega_{4,0}$. (——— $M = 0$); ($- \cdot - \cdot -$ $M = 0.01$); ($\bullet$ $M = 0.1$); ($\blacktriangle$ $M = 0.2$); ($*$ $M = 0.3$). Red, blue and green dashed lines represent the area ratios at which the axial wavenumber singularity occurs for $M = 0.1$, $M = 0.2$ and $M = 0.3$, respectively.

2.4.1.3 Case 2

This case considers the duct with two discontinuities, closed-closed boundaries and no mean flow. The cross-sectional areas of zones 1 and 3 are taken to be the same, $S_1 = S_3$, so that there is only one area ratio to be varied, S_2/S_1. In Figure 2.7, the first and fifth axial modes are compared with the theoretical predictions of Meissner, while the first transverse mode is compared with the numerical data of Meissner. Excellent agreement is seen for both the axial and transverse modes. The particularly good agreement observed for the $\Omega_{0,1}$ transverse mode, when compared to that in Case 1(a), may be attributed to the stabilizing effects on the modes due to the two

larger cross-section zones on either side of the smaller cross-section zone. It is to be noted that the limit $S_2/S_1 \rightarrow 0$ is arrived at differently in the current study and in Meissner [1]. In the current study, this limit is achieved by increasing S_1 due to the restrictions imposed on modal analysis by the cut-on frequency; whereas Meissner achieved this limit simply by reducing S_2 to zero. Therefore, as $S_2/S_1 \rightarrow 0$, the two analyses asymptote to different limiting cases. In the current study, the three-zone duct becomes a single-zone duct equivalent to zone 2, whereas no such thing happens in Meissner's case. Therefore, in the limit of $S_2/S_1 \rightarrow 0$, we recover the frequency of the central duct (zone 2) with open-open BCs.
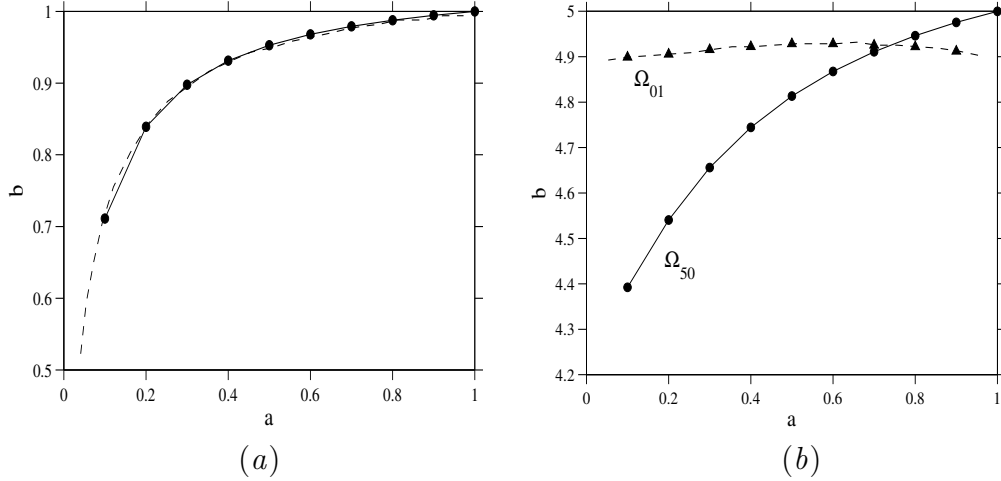
Figure 2.7: Comparison of modal predictions from the current theory with Meissner [1] for Case 2. Frequencies are normalized with the fundamental axial mode Ω_0 for a uniform cross-sectional duct of same length. (a) $\Omega_{1,0}$, (b) $\Omega_{5,0}$. —— Meissner's theoretical results for axial modes; - - - - Meissner's computational results for non-axial modes; • Current theoretical results for axial modes; ▲ Current theoretical results for non-axial modes.

2.4.1.4   Case 3

Cases 1 and 2 consider a uniform mean velocity profile. In this section, we present the effects of non-uniform, laminar parabolic and turbulent power-law mean velocity profiles on the acoustics of a single discontinuity two-zone duct. The acoustic modes explored are the fundamental axial mode and its first harmonic. Three area ratios $S_1/S_2 = 1$, 0.8, 0.5 are considered and the boundary conditions are open-open on both ends of the duct. Frequency predictions obtained using the current modal analysis are presented in Table 2.1.

As can be seen from Table 2.1, the effects of the non-uniform velocity profiles on the duct acoustics are not very significant. At $M_1 = 0.1$, there is less than 1% difference between the modal frequencies for the various velocity profiles. The difference, however, increases marginally both as the Mach number increases and the area ratio decreases, but the maximum difference between the uniform and turbulent velocity profiles is still less than 5% even at $M_1 = 0.3$ and $S_1/S_2 = 0.5$. Similar trends are also seen for the first axial harmonic in Table 2.2, with the effects of the laminar and turbulent velocity profiles being even smaller than those seen for the fundamental axial mode. From these results, we can conclude that the effects of the non-uniform mean velocity profiles on the acoustics of a duct are not significant enough to warrant their inclusion, particularly because of the significantly increased analytical complexity that their inclusion leads to.

Table 2.1: Fundamental mode (Ω_{10}, rad/s) as a function of inlet Mach number and area ratio for uniform mean flow, and the laminar and turbulent mean velocity profiles.

			Inlet Mach Number, M_1		
			0.1	0.2	0.3
Uniform Mean Flow	$\mathbf{\Omega_{10}}$	1.0	1079.85	1047.13	992.59
	Area Ratio	0.8	1113.72	1070.64	998.03
	$\frac{S_1}{S_2}$	0.5	1177.03	1080.35	1572.97
Parabolic Mean Flow	$\mathbf{\Omega_{10}}$	1.0	1078.75	1042.58	981.84
	Area Ratio	0.8	1112.03	1063.58	980.82
	$\frac{S_1}{S_2}$	0.5	1172.65	1059.39	1495.21
Turbulent Mean Flow	$\mathbf{\Omega_{10}}$	1.0	1081.44	1053.45	1006.80
	Area Ratio	0.8	1116.13	1080.33	1020.03
	$\frac{S_1}{S_2}$	0.5	1183.15	1106.55	1648.53

Table 2.2: First harmonic (Ω_{20}, rad/s) as a function of inlet Mach number and area ratio for uniform mean flow, and the laminar and turbulent mean velocity profiles.

			Inlet Mach Number, M_1		
			0.1	0.2	0.3
Uniform Mean Flow	$\boldsymbol{\Omega_{20}}$	1.0	2159.71	2094.26	1985.18
	Area Ratio	0.8	2127.48	2036.09	1884.21
	$\frac{S_1}{S_2}$	0.5	2042.48	1860.53	2168.09
Parabolic Mean Flow	$\boldsymbol{\Omega_{20}}$	1.0	2157.50	2085.17	1963.68
	Area Ratio	0.8	2124.54	2023.75	1854.29
	$\frac{S_1}{S_2}$	0.5	2036.83	1834.93	2037.96
Turbulent Mean Flow	$\boldsymbol{\Omega_{20}}$	1.0	2162.87	2106.91	2013.60
	Area Ratio	0.8	2131.69	2052.90	1922.03
	$\frac{S_1}{S_2}$	0.5	2050.34	1891.93	2310.92

2.4.2   Combustion Instabilities

2.4.2.1   Validation

The methodology developed in this study to incorporate the effects of fluctuating heat release rate into the combustion instability analysis is first validated using the study of Yu et al. [2], who investigated the combustion instabilities of a dump combustor using both experiments and a 1-D linear modal analysis. The zonal matching conditions employed by Yu et al. include the conventional mass, momentum, and

energy balances across the zonal interface(s), whereas acoustically consistent matching conditions are applied in the present study. Consequently, the current approach obviates the need for a separate energy matching condition. The Yu et al. choice of both the mean flame shape and its location involved significant assumptions as well. In that study, combustion is assumed to occur in the form of a 1-D planar flame at some location downstream of the area discontinuity. A consequence of these assumptions is that the flame is essentially a discontinuity in zonal mean properties, analogous to the discontinuity due to change in cross-section. The combustion chamber configuration in their study similar to that in Figure 4.10. The geometric parameters and mean flow properties in the Yu et al. study are provided in Table 4.2, and are used for validating the current approach as well.
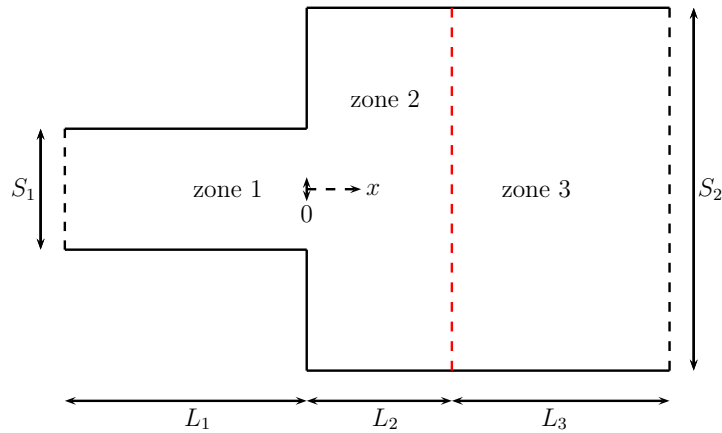
Figure 2.8: Geometry of the dump combustor considered by Yu et al., with the planar mean flame shape indicated using red dashed line.

Table 2.3: Geometric parameters and mean flow properties in the three-zone dump combustor (see Figure 3.1) considered in Yu et al. [2].

Geometry/Mean Property	Zone 1	Zone 2	Zone 3
Length (m)	0.171	0.038	0.215
Height (m)	0.0225	0.0450	0.0450
Mach number, $\overline{M}$	0.265	0.0548	0.0933
Temperature, $\overline{T}$ (K)	1020	1030	2660
Speed of sound, $\overline{c}$ (ms^{-1})	698	701	1110
Density, $\overline{\rho}$ (kg·m^{-3})	7.53	5.92	2.20
Pressure, $\overline{p}$ (MPa)	2.27	2.29	2.28

In Table 4.4, the unstable longitudinal mode frequencies obtained from the current analysis are compared with those from the experiments and 1-D modal analysis of Yu et al. [2]. It can be seen that the current predictions agree better with the Yu et al. experiments than do the results of their modal analysis. We believe that these improved predictions may be attributed to: (1) the acoustically consistent matching conditions employed in the current study, and (2) the novel approach to incorporate heat release effects directly into the longitudinal wavenumber. The difference between the experimental and current unstable mode predictions is less than 5%.

Table 2.4: Comparison of unstable longitudinal mode frequencies obtained from the current theory with those from the experiments and 1-D modal analysis of Yu et al. [2].

Frequency (Hz)	1-D Analytical (Yu et al.)	Experimental (Yu et al.)	Modal Analysis (Current)
Fundamental (Ω_{10})	1997	1905	1853
First harmonic (Ω_{20})	3785	3890	3906
Second harmonic (Ω_{30})	5878	5610	5791

2.4.2.2 Instability Characteristics

Here, we present the results for the 2-D instability analysis of the dump combustor with the mean flame shape indicated in Figure 3.1. The combustor is divided into three zones with the mean properties given in Table 2.5.

Table 2.5: Geometric parameters and mean flow properties in the three zones of the dump combustor.

Geometry/Mean Flow Property	Zone 1	Zone 2	Zone 3
Length, L (m)	0.3	L_f	$0.7 - L_f$
Temperature, $\overline{T}$ (K)	900	2500	2500
Speed of sound, $\overline{c}$ (m/s)	880.4	1856.4	1856.4
Density, $\overline{\rho}$ ($\frac{kg}{m^3}$)	1.6	1.6	1.6
Pressure, $\overline{p}$ (MPa)	1.0	1.0	1.0

The frequency space explored consists of the fundamental axial mode and its first two harmonics, as well as the first transverse mode. An extensive parametric space has also been studied consisting of: (i) inlet Mach number $M_1 = 0.1$, 0.2, 0.3; (ii) area ratio $S_1/S_2 = 0.8$, 0.6, 0.4; (iii) open-open and open-choked boundary conditions; (iv) flame length $L_f = S_1$, $1.59S_1$, which were chosen from Lee and Lieuwen [6]; and (v) time-lag between heat release and acoustic fluctuations $\tau = 0, \pi/3\Omega$. However, in the interest of brevity, we present representative results only. In this study, the temporal dependence of the acoustic fluctuations is given by $\exp(i\Omega t)$. This means that the stable frequencies have a positive imaginary part, whereas the *unstable frequencies have a negative imaginary part.*

The criterion for a feedback loop to be completed between the acoustic and heat release oscillations was given by Rayleigh [22], and is commonly referred to as the Rayleigh's criterion. Rayleigh's criterion states that instability occurs when the

heat release oscillations and pressure oscillations are positively correlated in time (constructive interference). Mathematically, it can be written as [7, 14]:

$$\frac{1}{T} \int_0^T q'(t)p'(t)dt > 0 \tag{2.48}$$

where T is the time period. For the flame response function under consideration (Eq. (2.41)), this criterion is satisfied when time-lag τ is given by [14]

$$0 < \tau < \frac{\pi}{2\Omega}; \ \frac{3\pi}{2\Omega} < \tau < \frac{5\pi}{2\Omega}; \ \ldots \tag{2.49}$$

Figure 2.9 shows the real and imaginary parts of the first three axial harmonics for $L_f = S_1$ and $\tau = 0$ with open-open boundary conditions at the duct inlet and outlet. Figure 2.9(a) plots the real parts of the fundamental axial mode and its first two harmonics as a function of area ratio S_1/S_2 for three inlet Mach numbers $\overline{M}_1 = 0.1$, 0.2, 0.3. In Figure 2.9(a), the lowest (blue) curves are for $\overline{M}_1 = 0.1$, while the middle (red) curves and the upper (black) curves are for $\overline{M}_1 = 0.2$ and $\overline{M}_1 = 0.3$, respectively. It is seen that for the fundamental mode (blue) and the second harmonic (black), Ω_{real} increases with area ratio, while the opposite is true for the first harmonic (red). Similar trends were observed in the acoustics study as well in the sense that the variation in modal frequency with duct area ratio differed from mode to mode. For a given area ratio, Ω_{real} of all three modes decrease with Mach number, as can be inferred from Eq. (2.47).
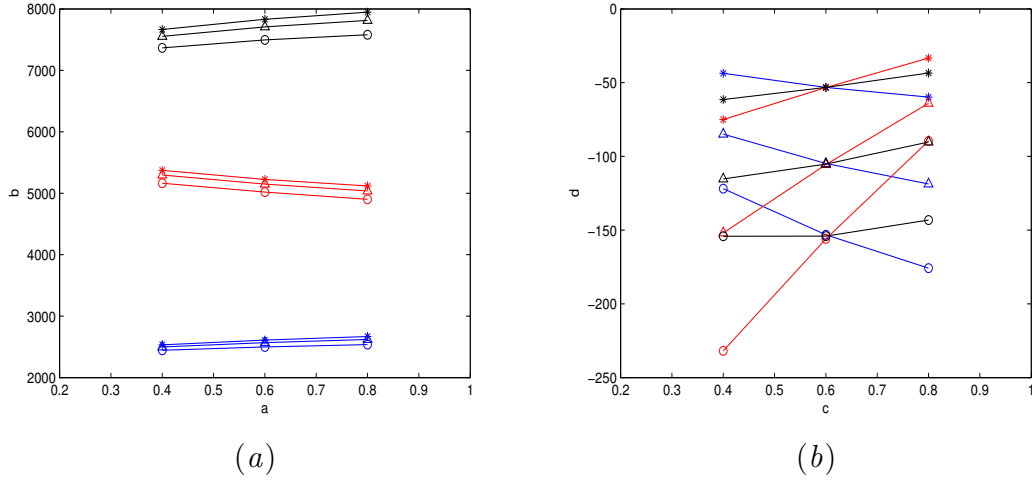
Figure 2.9: Instability characteristics of the first three axial harmonics for the case $L_f = S_1$, $\tau = 0$ and with open-open boundary conditions. (a) Real part of Ω (in rad/s), and (b) imaginary part of Ω versus the area ratio of the dump combustor (S_1/S_2). Blue lines represent the fundamental axial mode (Ω_{10}), red lines represent the first axial harmonic (Ω_{20}) and the black lines represent the second axial harmonic (Ω_{30}). Symbols $*$, $\triangle$ and $\circ$ represent frequencies at various Mach numbers; ($* \; \overline{M}_1 = 0.1$), ($\triangle \; \overline{M}_1 = 0.2$) and ($\circ \; \overline{M}_1 = 0.3$).

Figure 2.9(b) shows the imaginary parts of the fundamental axial mode and its first two harmonics as a function of area ratio for the three inlet Mach numbers considered. Since the value of $\tau = 0$ is such that the Rayleigh's criterion is satisfied, we can see that Ω_{imag} is negative for all three axial modes, suggesting that they are unstable. The magnitude of Ω_{imag} represents the temporal growth rate of the unstable modes, at least for small times when linear stability analysis is still valid. It is seen that for all three axial modes, the magnitudes of growth rates increase monotonically with inlet Mach number. The growth rate of the fundamental axial mode increases with the duct area ratio, while the opposite trend is seen for the first and second harmonics.

Figure 2.10 shows the real and imaginary parts of the first three axial harmonics for $L_f = 1.59S_1$ and $\tau = \frac{\pi}{3\Omega}$. Open-open boundary conditions are imposed
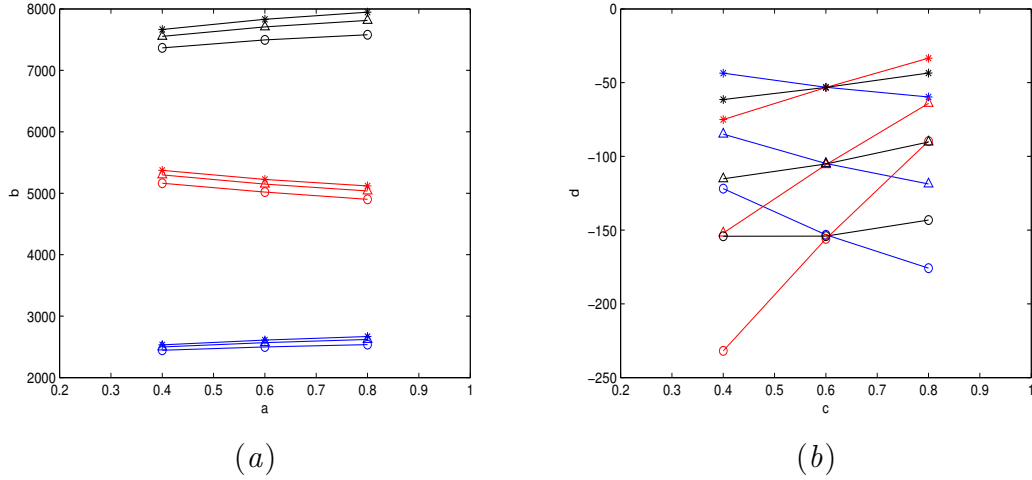
Figure 2.10: Instability characteristics of the first three axial harmonics for the case $L_f = 1.59S_1$, $\tau = \frac{\pi}{3\Omega}$ and with open-open boundary conditions. (a) Real part of Ω (in rad/s), and (b) imaginary part of Ω versus the area ratio of the dump combustor (S_1/S_2). Blue lines represent the fundamental axial mode (Ω_{10}), red lines represent the first axial harmonic (Ω_{20}) and the black lines represent the second axial harmonic (Ω_{30}). Symbols $*$, $\triangle$ and $\circ$ represent frequencies at various Mach numbers; ($* \ \overline{M}_1 = 0.1$), ($\triangle \ \overline{M}_1 = 0.2$) and ($\circ \ \overline{M}_1 = 0.3$).

at the duct inlet and outlet. It can be seen from Figure 2.9 and Figure 2.10 that a simultaneous variation in flame length from $L_f = S_1$ to $L_f = 1.59S_1$, and time-lag from $\tau = 0$ to $\tau = \frac{\pi}{3\Omega}$ does not result in significant changes in the real and imaginary parts of the unstable modes. In fact, it was found that changing L_f while τ is held fixed, or changing τ while L_f is held fixed, resulted in negligible changes in the real and imaginary parts of the three axial modes as long as τ satisfied the Rayleigh's criterion. This is because combustion instability is strongly driven by the mean flow properties and rather weekly influenced by other parameters. An interesting artifact of the growth rates ($|\Omega_{\text{imag}}|$) seen in Figure 2.10 is that for a given Mach number, the Ω_{imag} curves for all three modes nearly intersect at an area ratio of about 0.6; it is, however, not clear why this is the case.

54
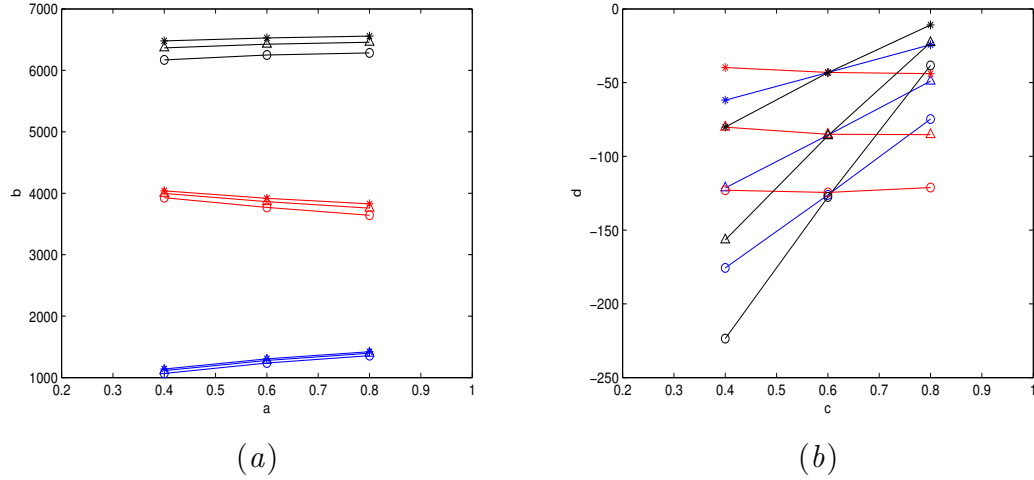
Figure 2.11: Instability characteristics of the first three axial harmonics for the case $L_f = S_1$, $\tau = 0$ and with open-choked boundary conditions. (a) Real part of Ω (in rad/s), and (b) imaginary part of Ω versus the area ratio of the dump combustor (S_1/S_2). Blue lines represent the fundamental axial mode (Ω_{10}), red lines represent the first axial harmonic (Ω_{20}) and the black lines represent the second axial harmonic (Ω_{30}). Symbols $*$, $\triangle$ and $\circ$ represent frequencies at various Mach numbers; ($* \ \overline{M}_1 = 0.1$), ($\triangle \ \overline{M}_1 = 0.2$) and ($\circ \ \overline{M}_1 = 0.3$).

The results presented in Figure 2.9-Figure 2.10 were for open-open boundary conditions. Next, we will discuss the effects of changing the boundary conditions on the unstable frequencies. Figure 2.11 shows the real and imaginary parts of the first three axial harmonics for $L_f = S_1$ and $\tau = 0$. The trends are essentially the same as those in Figure 2.9. However, both the real frequencies (Ω_{real}) and growth rates ($|\Omega_{\mathrm{imag}}|$) are higher for the open-open case than for the open-choked case.

So far, we have discussed the axial mode instabilities. In Table 2.6, we present the instability characteristics of the first transverse mode (Ω_{01}) for open-open boundary condition. The flame length and time-lag considered are $L_f = S_1$ and $\tau = 0$, respectively. The first transverse mode (Ω_{01}) appears to be unstable for all area ratios and inlet Mach numbers. We do not present the instability characteristics of Ω_{01}

for the other boundary conditions owing to the insignificant effect axial boundary conditions have on the transverse modes.

The results presented in Table 2.6 indicate that the transverse-mode growth rates follow no particular trend with varying area ratio and Mach number, unlike the axial modes considered in the preceding discussion. For instance, when the area ratio is 0.8, the growth rate increases with inlet Mach number. For area ratios of 0.6 and 0.4, the growth rates increase at first and then decrease with increasing Mach number. For the inlet Mach numbers of 0.1 and 0.2, growth rates decrease with an increase in area ratio, but no specific trend can be ascertained for the Mach number of 0.3. This may be because we are approaching the limits of applicability of the linear stability analysis with an inlet Mach number of 0.3. As with the growth rates, Table 2.6 indicates that the real frequencies also do not adhere to any discernible trend for the fundamental transverse mode.

Table 2.6: First transverse mode (Ω_{01}) frequency (rad/s) and growth rates (rad/s) for different values of area ratio and inlet Mach number for $L_f = S_1$ and $\tau = 0$. The boundary conditions are open-open.

		Inlet Mach Number, $\overline{M}_1$					
		0.1		0.2		0.3	
		Frequency Ω_{real}	Growth Rate Ω_{imag}	Frequency Ω_{real}	Growth Rate Ω_{imag}	Frequency Ω_{real}	Growth Rate Ω_{imag}
$\boldsymbol{\Omega_{01}}$	0.8	15637.192	-4.02	15450.95	-8.367	15101.1	-28.295
Area Ratio	0.6	15656.558	-10.106	15483.142	-19.075	15684.67	-12.966
$\frac{S_1}{S_2}$	0.4	15672.476	-16.77	15850.588	-25.355	15456.64	-14.57

2.5 Summary

A novel, acoustically consistent linear modal analysis to predict the combustion instabilities of a dump combustor is presented. As a first step, an *a priori* acoustical analysis of two ducts with one and two discontinuities in cross-section was performed. Acoustically consistent matching conditions involving matching of acoustic velocity and acoustic pressure at the cross-sectional interface(s) were developed. In conjunction with the duct boundary conditions, these constraints enable us to recover the dispersion relation governing the axial modes. A detailed investigation of the effects of non-uniform laminar and turbulent mean velocity profiles was undertaken. It is seen that the nature of the velocity profile, uniform or non-uniform, has only a small impact on duct acoustics. This is an important conclusion since the inclusion of non-uniform mean velocity profile leads to significantly increased analytical complexity for the instability analysis. The complexity arises because a non-uniform velocity profile contributes both as a stand-alone source term in the wave equation, and as a factor in the heat release source term $\overline{D}q'/\overline{D}t$. A distinguishing feature of the current instability analysis is that the acoustic wave equation is solved along with the fluctuating heat-release source term. Consequently, combustion effects are incorporated directly into the axial wavenumber in the combustion zone. This is to be contrasted with prior studies in which heat release effects are included *a posteriori* in the form of energy balance across the flame, which inherently means that the flame is assumed to be compact. The current approach makes no such assumption. Instabilities are demonstrated for the fundamental longitudinal mode and its harmonics, as well as for

the fundamental transverse mode. A detailed parametric study reveals that instabilities are principally affected by the mean flow properties and the combustor geometry, and parameters such as the flame length are seen to have little impact. The current study may be extended to 3-D geometries without much difficulty, and can also be enhanced to include additional physics such as entropy and vorticity waves, as well as vortex shedding that occurs in many combustors.

CHAPTER 3

A NOVEL LEVEL SET APPROACH FOR PREMIXED FLAME RESPONSE AND ITS APPLICATION TO PREDICT COMBUSTION INSTABILITIES IN A DUMP COMBUSTOR

3.1 Abstract

In combustion instability analysis, a flame transfer function is used to describe the response of a premixed flame to incident acoustic oscillations. A novel flame transfer function (FTF) is developed that relates the fluctuations in flame heat-release rate to those in density, heat of reaction, turbulent flame speed, and the flame surface area. Each of these four contributions is eventually expressed in terms of the fluctuations in acoustic pressure and velocity through the respective response functions. The flame surface-area response to acoustic oscillations is incorporated into the FTF through a novel G-equation level-set method. In this method, we directly solve for the level set fluctuations G' in terms of the velocity fluctuations, and then relate the flame surface-area oscillations to G'. In the absence of turbulent flame-speed fluctuations, the response functions from the present G-equation approach are in good agreement with those from the conventional f-equation approach (where one writes $G(x, y, t) = x - f(y, t)$). However, when turbulent flame-speed fluctuations

are included, the two approaches differ, principally in the flame response to axial velocity fluctuations. The current flame transfer function, generalized for any mean flame shape, is applied to analyze the response of a V-shaped mean flame located at the cross-sectional interface of a 2-D dump combustor. For this flame, the effects of variation in acoustic frequency, mean Mach number, mean temperature, and mean equivalence ratio on the FTF magnitude and phase are investigated. Both axial and mixed mode acoustic perturbations are considered. For the purely axial modes, the response-function amplitudes of density and heat of reaction are seen to be independent of frequency, while those of flame speed and axial velocity exhibit harmonic-like oscillations as a function of frequency. For the mixed-mode fluctuations, the response-function amplitude of density decays monotonically with frequency, whereas the response-function amplitudes of the heat of reaction, turbulent flame speed, and velocity components show decaying oscillatory behavior in frequency. Further, it is observed that the flame-speed response function contributes the most to the overall flame transfer function. Phase analysis of the FTF shows that the transverse velocity response is nearly in phase with the heat-release fluctuations. In addition, density and transverse velocity fluctuations always show constructive interference with pressure fluctuations. The current FTF is also incorporated into a linear modal analysis framework to predict the combustion instabilities in a 2-D dump combustor, and the model predictions validated against experiments. Three mean velocity profiles—uniform, parabolic, and turbulent power law—are considered. For the three flames, the first three longitudinal and fundamental transverse unstable modes are predicted.

3.2 Introduction

Prediction of combustion instabilities using linear modal analysis requires as an input a transfer function describing the flame response to acoustic perturbations, commonly referred to as the flame transfer function (FTF). The two principal characteristics of interest in an FTF are its: (1) magnitude, which is a measure of the ratio of the amplitudes of heat-release and acoustic perturbations, and (2) phase, which quantifies the phase difference between these two perturbations. In the present FTF, the fluctuations in flame heat-release rate are expressed in terms of those in density, heat of reaction, turbulent flame speed, and flame surface area. The response of flame surface area to incident disturbances is described using a novel G-equation level set method that is based on directly solving for the fluctuations G' in terms of the acoustic velocity fluctuations. This method differs from the conventional approach that involves writing $G(x, y, t) = x - f(y, t)$ and then solving for f'. The response functions from the two methods are compared, and the advantages of the current method are discussed. While the FTF developed is generalized for any mean flame shape, the response of a V-shaped flame is analyzed in detail, focusing on the effects of acoustic frequency, mean Mach number, mean temperature, and mean equivalence ratio on the magnitude and phase of the flame transfer function. Subsequently, the FTF is combined with an acoustically consistent modal analysis approach developed by the current authors [23]. For three mean flames, corresponding to three mean velocity profiles, the longitudinal and transverse unstable modes of a 2-D dump combustor are computed.

Combustion instabilities are manifested as self-excited acoustic oscillations that are sustained by a feedback loop between the acoustic perturbations and the heat-release fluctuations. The Rayleigh criterion [14, 22, 24–26] suggests that instabilities occur when the net acoustic energy pumped into the system due to the pressure–heat-release feedback exceeds the energy losses due to various mechanisms (e.g., acoustic radiation and viscous losses). Reduced order analytical approaches, such as the linear modal analysis [2, 4, 5, 11–14, 23, 27] and Nyquist-plot-based network models [28–33], are commonly used to predict the instability modes. An essential component of these analytical methods is the flame transfer function (FTF) that relates flame heat-release fluctuations to acoustic perturbations impinging on the flame.

Among the early works on premixed flame response to acoustic fluctuations are those of Marble and Candel [34], Subbiah [35], Yang and Culick [36], and Poinsot and Candel [37], which were all based on applying the integral technique. This technique entails the integration, normal to the flame, of the relevant conservation equations, in conjunction with the solution of level-set equations that track the flame surface. Marble and Candel [34] investigated the unsteady flame response, and quantified the variation in flame shape with the inflow Mach number, and in pressure transmission and reflection coefficients with the Strouhal number. Using an approach similar to that of Marble and Candel [34], Subbiah [35] performed both steady and unsteady analysis of premixed flame response. It is to be noted, however, that the integral approach in [34] and [35] does not result in an explicit flame transfer function. Yang and Culick [36] combined the integral technique with a modal representation of acoustic fluctuations to perform flame response analysis, as well as determine the unstable

modes. Poinsot and Candel [37] used the integral technique to numerically determine nonlinear flame response in premixed combustors.

A large number of subsequent studies on flame response used the level-set equation approach for deriving various forms of the flame transfer function, which may be incorporated into a reduced-order model for predicting instabilities [28, 38–45]. Boyer and Quinard [39] studied the dynamics of premixed, anchored V flames. The effects of longitudinal acoustic waves and Von Karmen vortex shedding on the flame shape and dynamics were analyzed. They showed that for low-amplitude disturbances in the flow and the acoustic field, their linear model satisfactorily predicted the flame shape. Fleifil et al. [45] derived an FTF for a conical flame on the rim of a tube that relates the flame heat-release fluctuations to the flame surface-area fluctuations. Their analysis considered a spatially uniform acoustic field, with 1-D flame surface kinematics. Fleifil et al. [45] found that the flame dynamics is predominantly governed by two parameters: (1) flame Strouhal number based on duct radius and laminar flame speed, and (2) ratio of laminar flame speed to mean flow velocity. It was found that the flame essentially acts as a high-pass filter, i.e., higher frequencies have only weak effects on flame heat release, whereas lower frequencies interact strongly with the flame.

Important contributions to the development and analysis of flame transfer functions were made by Lieuwen and co-workers [7, 46–53]. For instance, a detailed analysis of the response of laminar premixed flames to equivalence ratio fluctuations was performed by Cho and Lieuwen [46]. Lieuwen [47] provided a comprehensive overview of the existing literature on the modeling of premixed flame-acoustic inter-

actions. Two FTFs based on linear flamelet analysis were discussed in particular—the first relating heat release oscillations to velocity perturbations, and the second to equivalence ratio fluctuations. Lieuwen [47] demonstrated that the former can be expressed as a time-lag model at low frequencies, while the latter required kinematic modeling of flame-equivalence-ratio interactions. You et al. [54] also employed the G-equation-based flame kinematics to perform detailed flame response analysis that included axial variations in the chamber geometry and mean flow field. Fluctuations in laminar flame speed, flame surface area, and the heat of reaction were also considered.

In the current study, a comprehensive flame transfer function is derived and applied to analyze the response of a V-shaped mean flame anchored at the cross-sectional interface in a 2-D dump combustor. The transfer function includes the effects of acoustic fluctuations in density, heat of reaction, turbulent flame speed, and flame surface area. The flame surface-area response is derived based on a novel G-equation method that involves directly solving the G'-equation by using the harmonic nature of the incident velocity fluctuations. A detailed comparison of the present approach with an approach based on writing $G(x, y, t) = x - f(y, t)$ is undertaken. The conditions under which the two methods agree and differ are presented. Using the current FTF, a detailed parametric study is undertaken that investigates the effects of acoustic frequency, mean Mach number, mean temperature and mean equivalence ratio on the FTF magnitude and phase. Following the flame response analysis, the combustion instability modes of the dump combustor are computed for uniform, parabolic and turbulent mean velocity profiles.

3.3 Derivation of Flame Transfer Function
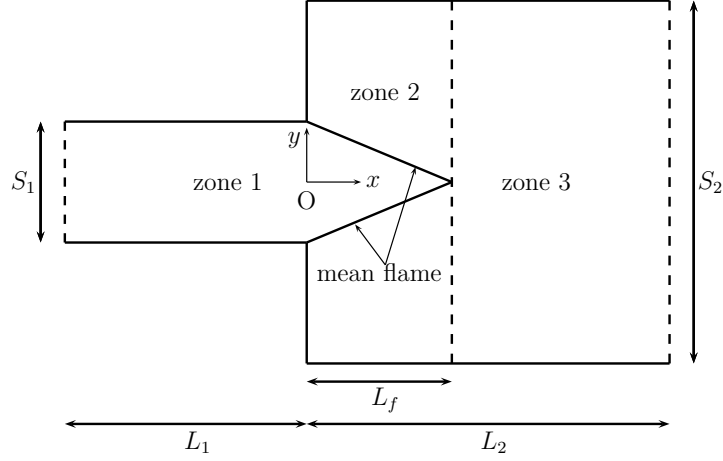
Figure 3.1: Geometry of the dump combustor with a V-shaped mean flame.

The combustor geometry and mean flame shape under consideration are shown in Figure 3.1. The local, instantaneous heat-release rate on the flame, $\mathrm{d}\dot{Q}$, is given by:

$$\mathrm{d}\dot{Q} = h_r \rho \ s_L \mathrm{d}A \tag{3.1}$$

where h_r is the heat of reaction, ρ is density, s_L is the local flame speed, and $\mathrm{d}A$ is the local flame surface area.

Following the triple decomposition of variables used in [54–56], a flow variable Θ may be expressed as

$$\Theta = \overline{\Theta} + \Theta' + \Theta''$$

$$= \langle \Theta \rangle + \Theta'' \tag{3.2}$$

where $\overline{\Theta}$ is the long-time mean, Θ' and Θ'' are the periodic and turbulent fluctuations, respectively, and $\langle \Theta \rangle = \overline{\Theta} + \Theta'$ is the ensemble average of Θ.

Ensemble averaging Eq. (3.1), followed by using the property $\langle \Theta'' \rangle = 0$, and dropping the non-linear covariance terms as well as using the definition of turbulent flame speed s_T, we obtain [14, 54]

$$\langle \mathrm{d}\dot{Q} \rangle = \langle h_r \rangle \langle \rho \rangle s_T \langle \mathrm{d}A \rangle \tag{3.3}$$

Decomposing the ensemble averaged quantities into the sum of long-time means and periodic fluctuations, we get

$$\langle \mathrm{d}\dot{Q} \rangle = \overline{\mathrm{d}\dot{Q}} + \mathrm{d}\dot{Q}' \tag{3.4}$$

where $\overline{\mathrm{d}\dot{Q}} = \overline{\rho} \overline{h_r} \overline{s_T} \mathrm{d}\overline{A}$. Upon linearization $\mathrm{d}\dot{Q}'$ becomes

$$\mathrm{d}\dot{Q}' = \overline{h_r} \overline{s_T} \mathrm{d}\overline{A}\rho' + \overline{\rho}\ \overline{s_T} \mathrm{d}\overline{A}h_r' + \overline{\rho}\overline{h_r}\mathrm{d}\overline{A}s_T' + \overline{\rho}\overline{h_r}\overline{s_T}\mathrm{d}A' \tag{3.5}$$

Dividing Eq. (3.5) by $\overline{\mathrm{d}\dot{Q}}$,

$$\frac{\mathrm{d}\dot{Q}'}{\overline{\mathrm{d}\dot{Q}}} = \frac{\rho'}{\overline{\rho}} + \frac{h_r'}{\overline{h_r}} + \frac{s_T'}{\overline{s_T}} + \frac{\mathrm{d}A'}{\mathrm{d}\overline{A}} \tag{3.6}$$

In the next step, each of the fluctuations on the RHS of Eq. (3.6) is related to the acoustic pressure and velocity perturbations p' and $\mathbf{u}'$ through the corresponding response functions. It is relevant to mention here that Eq. (3.6) also includes the effects of density fluctuations that are often neglected using the argument that $\rho' =$

$p'/\overline{c}^2$. However, it is evident from Eq. (3.6) that we are interested in the ratio $\rho'/\overline{\rho}$, rather than ρ' itself. The relative importance of the four terms on the RHS of (3.6) is quantitatively established in Section 3.5. In the discussion that follows, we present the derivation of the response functions for each of the fluctuations, as well as the current G-equation approach.

3.3.1 Density Fluctuations

Using the ideal gas equation $p = \rho R T$, performing a Taylor-series expansion of ρ about the mean pressure and temperature (motivated by You [54]), and retaining the first order terms, we have

$$\rho = \underbrace{\frac{\overline{p}}{R\overline{T}}}_{\overline{\rho}} + \underbrace{\left.\frac{\partial\rho}{\partial p}\right|_{\overline{p},\overline{T}} p' + \left.\frac{\partial\rho}{\partial T}\right|_{\overline{p},\overline{T}} T'}_{\rho'} = \frac{\overline{p}}{R\overline{T}} + \frac{1}{R\overline{T}}p' - \frac{\overline{p}}{R\overline{T}^2}T' \tag{3.7}$$

Now, we need expressions for p' and T'. In a 2-D cartesian duct of uniform cross-section, the acoustic pressure fluctuations p', u' and v' may be written as [5, 10, 14, 23, 54]

$$p'(x, y, t) = \mathscr{C}e^{ikx}\cos{(k_y y)}e^{i\Omega t} \tag{3.8}$$

$$u'(x, y, t) = -\mathscr{C}\frac{1}{\overline{\rho}}\frac{k}{\Omega + \overline{u}k}e^{ikx}\cos{(k_y y)}e^{i\Omega t} \tag{3.9}$$

$$v'(x, y, t) = \mathscr{C}\frac{1}{\overline{\rho}}\frac{k_y}{\Omega + \overline{u}k}e^{ikx}\sin{(k_y y)}e^{i\Omega t} \tag{3.10}$$

where $\mathscr{C}$ is the amplitude, Ω is the angular frequency, $k = \Omega/\overline{c}$ is the axial wavenumber ($\overline{c}$ is the mean speed of sound), and $k_y = 2n\pi/S$ is the transverse wavenumber (n

is the modal index, and S is the duct height). These fluctuating forms satisfy the homogeneous convected wave equation (Eq. (3.61)), as well as the linearized axial and transverse momentum equations.

To derive an expression for the temperature fluctuations T', we consider the temperature form of the energy equation (ignoring heat conduction, and viscous losses) [14, 57, 58]:

$$\rho c_v \left(\frac{\partial T}{\partial t} + \mathbf{u} \bullet \boldsymbol{\nabla} T \right) + p \left(\frac{\partial u}{\partial x} + \frac{\partial v}{\partial y} \right) = 0 \qquad (3.11)$$

where c_v is the specific heat at constant volume, and u and v are the axial and transverse components of velocity. Assuming there are no axial gradients in mean quantities and no transverse mean flow, and linearizing, we get

$$\bar{\rho} c_v \left(\frac{\partial T'}{\partial t} + \bar{u} \frac{\partial T'}{\partial x} \right) + \bar{p} \left(\frac{\partial u'}{\partial x} + \frac{\partial v'}{\partial y} \right) = 0 \qquad (3.12)$$

One may consider the following form for temperature fluctuations T'

$$T' = e^{i\Omega t} e^{ikx} [\alpha_1 \cos(k_y y) + \alpha_2 \sin(k_y y)] \qquad (3.13)$$

where amplitudes α_1 and α_2 are to be determined. Substituting u', v' and T' into Eq. (3.12), we can solve for α_1 and α_2 in terms of the amplitude of pressure fluctua-

tions, $\mathscr{C}$. Finally, the form for temperature fluctuations is given by:

$$
\begin{aligned}
T' &= -i\frac{\overline{p}}{c_v\overline{\rho}^2}\frac{1}{(\Omega + \overline{u}k)^2}(ik^2 - k_y^2)[\mathscr{C}e^{ikx}\cos{(k_y y)}e^{i\Omega t}] \\
&= -i\frac{\overline{p}}{c_v\overline{\rho}^2}\frac{1}{(\Omega + \overline{u}k)^2}(ik^2 - k_y^2)p'
\end{aligned}
\tag{3.14}
$$

It can be verified that Eq. (3.14), in conjunction with Eqs. (3.9) and (3.10), satisfies

the linearized energy equation (3.12).

Substituting p' and T' into Eq. (3.7) gives the following expression for ρ'

$$
\frac{\rho'}{\overline{\rho}} = \underbrace{\left\{1 + i\frac{\overline{p}^2}{c_v\overline{T}\overline{\rho}^2}\frac{1}{(\Omega + \overline{u}k)^2}(ik^2 - k_y^2)\right\}}_{R_\rho}\frac{p'}{\overline{p}}
\tag{3.15}
$$

where R_ρ may be referred to as the response function that relates density fluctuations

to pressure fluctuations. It may be noted that in Eq. (3.15), the second term of

R_ρ (with the coefficient i) arises from T'. If one were to neglect T', we will have

$\rho'/\overline{\rho} = p'/\overline{p}$, suggesting that density fluctuations may not be neglected.

3.3.2   Heat of Reaction Fluctuations

For a methane-air mixture with equivalence ratio ϕ, Abu-Orf and Cant [59]

provided the following expression for the heat of reaction:

$$
h_r(\phi) = \begin{cases} \frac{2.9125\times10^6\,\phi}{1+0.05825\,\phi}, & \phi \geq 1 \\[2mm] \frac{2.9125\times10^6}{1+0.05825\,\phi}, & \phi < 1 \end{cases} \quad \text{(J/kg)}
\tag{3.16}
$$

69

Performing a Taylor-series expansion of h_r about $\overline{\phi}$ and retaining the first order terms,

$$h'_r = \left.\frac{\partial h_r}{\partial \phi}\right|_{\overline{\phi}} \phi' \tag{3.17}$$

You et al. [54] provided the following expression for ϕ'

$$\phi' = \overline{\phi}\left(\frac{u'}{\overline{u}} - \frac{\rho'}{\overline{\rho}}\right) e^{-i\Omega\tau} \tag{3.18}$$

where τ is the convective time lag for the equivalence ratio fluctuations to travel from the injector to the flame front. Considering a V-shaped mean flame, τ is given by

$$\tau = \frac{L_1}{\overline{u}} + \underbrace{\frac{1}{L_f} \int_0^{L_f/\overline{u}} \frac{y - S_1/2}{m} \, \mathrm{d}y}_{\tau_{\mathrm{f,avg}}} \tag{3.19}$$

where L_1 is the length of the smaller duct as shown in Figure 3.1, and $\tau_{\mathrm{f,avg}}$ is the average time taken by the fluctuations to travel to the flame from the cross-sectional interface (S_1 is the height of the smaller duct, L_f is the flame length, and m is the slope of the mean flame).

Substituting Eq. (3.18) into Eq. (3.17), and plugging into the resulting equation u' and Eq. (3.15) gives

$$\frac{h'_r}{\overline{h_r}} = \underbrace{-\left.\frac{\partial h_r}{\partial \phi}\right|_{\overline{\phi}} \frac{\overline{\phi}}{\overline{h_r}} \left\{1 + \frac{\overline{p}}{\overline{\rho}} \frac{k}{\overline{u}} \frac{1}{\Omega + \overline{u}k} + i\frac{\overline{p}^2}{c_v\overline{T}\overline{\rho}^2} \frac{1}{(\Omega + \overline{u}k)^2}(ik^2 - k_y^2)\right\}}_{R_{\mathrm{HR}}} \frac{p'}{\overline{p}} \tag{3.20}$$

where R_{HR} is the response function relating fluctuations in the heat of reaction to those in pressure.

3.3.3 Turbulent Flame Speed Fluctuations

We consider the Abu-Orf and Cant [60] model for the flame speed as a function of equivalence ratio, temperature, and pressure:

$$s_T(\phi, T, p) = C_1 \phi^{C_2} e^{-C_3(\phi - C_4)^2} \left(\frac{T}{T_0}\right)^{C_5} \left(\frac{p}{p_0}\right)^{C_6} \tag{3.21}$$

where $T_0 = 300\text{K}$ and $p_0 = 1\text{bar}$ are the reference temperature and pressure, and C_1 through C_6 are constants measured at these reference conditions. Their values are [54]: $C_1 = 0.6079$ m/s, $C_2 = -2.554$, $C_3 = 7.31$, $C_4 = 1.23$, $C_5 = 2$, $C_6 = -0.5$.

Again, s_T can be linearized in terms of (ϕ', T', p') as

$$s_T(\phi, T, p) = \underbrace{s_T(\overline{\phi}, \overline{T}, \overline{p})}_{\overline{s_T}} + \underbrace{\left\{ \left(\frac{\partial s_T}{\partial \phi}\right)\Big|_{(\overline{\phi}, \overline{T}, \overline{p})} \phi' + \left(\frac{\partial s_T}{\partial T}\right)\Big|_{(\overline{\phi}, \overline{T}, \overline{p})} T' + \left(\frac{\partial s_T}{\partial p}\right)\Big|_{(\overline{\phi}, \overline{T}, \overline{p})} p' \right\}}_{s_T'}$$

$$\tag{3.22}$$

Substituting ϕ' and T' from Eqs. (3.18) and (3.14) into Eq. (3.22) gives us

$$\frac{s_T'}{\overline{s_T}} = \frac{p'}{\overline{p}} \frac{\overline{p}}{C_1\overline{\phi}^{C_2}e^{-C_3(\overline{\phi}-C_4)^2}\left(\frac{\overline{T}}{T_0}\right)^{C_5}\left(\frac{\overline{p}}{p_0}\right)^{C_6}} \times$$

$$\left\{ -\overline{\phi}e^{-i\Omega\tau}\left[C_1C_2\overline{\phi}^{C_2-1}e^{-C_3(\overline{\phi}-C_4)^2} - 2C_1C_3\overline{\phi}^{C_2}(\overline{\phi}-C_4)e^{-C_3(\overline{\phi}-C_4)^2}\right]\left(\frac{\overline{T}}{T_0}\right)^{C_5}\left(\frac{\overline{p}}{p_0}\right)^{C_6} \times \right.$$

$$\left[1 + \frac{1}{\overline{\rho u}}\frac{k}{\Omega + \overline{u}k} + +i\frac{\overline{p}}{c_v\overline{T}\overline{\rho}^2}\frac{1}{(\Omega + \overline{u}k)^2}(ik^2 - k_y^2)\right]$$

$$+ C_1C_6\overline{\phi}^{C_2}e^{-C_3(\overline{\phi}-C_4)^2}\left(\frac{\overline{T}}{T_0}\right)^{C_5}p_0^{-C_6}\overline{p}^{C_6-1} - iC_1C_5\overline{\phi}^{C_2}e^{-C_3(\overline{\phi}-C_4)^2}T_0^{-C_5}\overline{T}^{C_5-1} \times$$

$$\left.\left(\frac{\overline{p}}{p_0}\right)^{C_6}\frac{\overline{p}}{c_v\overline{\rho}^2}\frac{1}{(\Omega + \overline{u}k)^2}(ik^2 - k_y^2)\right\}$$

$$= \frac{p'}{\overline{p}}R_{\mathrm{ST}} \tag{3.23}$$

where R_{ST} is the response function relating fluctuations in turbulent flame speed to those in pressure.

3.3.4 Flame Surface Area Fluctuations

Flame surface kinematics may be described using the level-set G-equation

$$\frac{\partial G}{\partial t} + \mathbf{u} \bullet \boldsymbol{\nabla} G = s_L|\boldsymbol{\nabla} G| \tag{3.24}$$

where $G(x,y,t) = 0$ is nominally defined as the flame, $\mathbf{u}$ is the velocity field, and s_L is the local flame speed. Prior studies, such as [45–47, 54], substituted $G(x,y,t) = x - f(y,t)$ into Eq. (3.24) and then solved for the fluctuations $f'(y,t)$. The flame surface area fluctuations were then related to $f'(y,t)$ (we will henceforth refer to this method as the f-approach). In the present study, we directly solve for the

field quantity, $G'(x, y, t)$, by utilizing the harmonic form of the acoustic oscillations. Subsequently, we relate the flame surface area oscillations to G' (we will refer to this as the G-approach). A detailed discussion of the G-approach follows.

We begin by writing $G(x, y, t) = \overline{G}(x, y) + G'(x, y, t)$, where $\overline{G}(x, y)$, $G'(x, y, t)$ and $G(x, y, t)$ are all field quantities that are defined everywhere in the flow. This gives rise to the question: how does one reconstruct the flame at any time t? At time t, we consider the flame to be located at the positions $(x, y) \ni G(x, y, t) = 0$. For $t = 0$, since $G'(x, y, 0) = 0$, the flame surface is given by the $\overline{G}(x, y) = 0$ isosurface, i.e., initially the flame surface coincides with the mean flame. For $t > 0$, however, the flame surface is given by the isosurface of points satisfying $\overline{G}(x, y) + G'(x, y, t) = 0$, where the locations (x, y) are not the same as those satifying $\overline{G}(x, y) = 0$. Flame reconstruction using this approach is also elaborated subsequently.

Considering Eq. (3.24), and splitting the variables into mean and coherent fluctuations yields

$$
\frac{\partial G'}{\partial t} + \overline{\mathbf{u}} \bullet \boldsymbol{\nabla} \overline{G} + \overline{\mathbf{u}} \bullet \boldsymbol{\nabla} G' + \mathbf{u}' \bullet \boldsymbol{\nabla} \overline{G} + \mathbf{u}' \bullet \boldsymbol{\nabla} G' = (\overline{s_T} + s_T') \sqrt{\left(\frac{\partial \overline{G}}{\partial x} + \frac{\partial G'}{\partial x} \right)^2 + \left(\frac{\partial \overline{G}}{\partial y} + \frac{\partial G'}{\partial y} \right)^2}
$$

$$(3.25)$$

Linearizing (3.25) yields the following equations for $\overline{G}$ and G':

$$
\overline{u} \frac{\partial \overline{G}}{\partial x} = \overline{s_T} \sqrt{\left(\frac{\partial \overline{G}}{\partial x} \right)^2 + \left(\frac{\partial \overline{G}}{\partial y} \right)^2}
\qquad (3.26)
$$

$$\frac{\partial G'}{\partial t} + \overline{\mathbf{u}} \bullet \boldsymbol{\nabla} G' + \mathbf{u'} \bullet \boldsymbol{\nabla}\overline{G} = s'_T \sqrt{\left(\frac{\partial\overline{G}}{\partial x}\right)^2 + \left(\frac{\partial\overline{G}}{\partial y}\right)^2}$$
$$+ \overline{s_T}\sqrt{\left(\frac{\partial\overline{G}}{\partial x}\right)^2 + \left(\frac{\partial\overline{G}}{\partial y}\right)^2} \left\{ \frac{\frac{\partial\overline{G}}{\partial x}\frac{\partial G'}{\partial x} + \frac{\partial\overline{G}}{\partial y}\frac{\partial G'}{\partial y}}{\left(\frac{\partial\overline{G}}{\partial x}\right)^2 + \left(\frac{\partial\overline{G}}{\partial y}\right)^2} \right\} \tag{3.27}$$

$$\Rightarrow \frac{\partial G'}{\partial t} + \overline{u}\frac{\partial G'}{\partial x} - \frac{\overline{s_T}\frac{\partial\overline{G}}{\partial x}}{\sqrt{\left(\frac{\partial\overline{G}}{\partial x}\right)^2 + \left(\frac{\partial\overline{G}}{\partial y}\right)^2}}\frac{\partial G'}{\partial x} - \frac{\overline{s_T}\frac{\partial\overline{G}}{\partial y}}{\sqrt{\left(\frac{\partial\overline{G}}{\partial x}\right)^2 + \left(\frac{\partial\overline{G}}{\partial y}\right)^2}}\frac{\partial G'}{\partial y}$$
$$= s'_T\sqrt{\left(\frac{\partial\overline{G}}{\partial x}\right)^2 + \left(\frac{\partial\overline{G}}{\partial y}\right)^2} - \frac{\partial\overline{G}}{\partial x}u' - \frac{\partial\overline{G}}{\partial y}v' \tag{3.28}$$

The above equation may be solved for G' using the u', v', and s'_T forms given in Eqs. (3.9), (3.10) and (3.23), respectively, and the mean flame shape $\overline{G}$. This is illustrated below for a linear mean flame.

G' Solution and Flame Reconstruction for a Linear Mean Flame
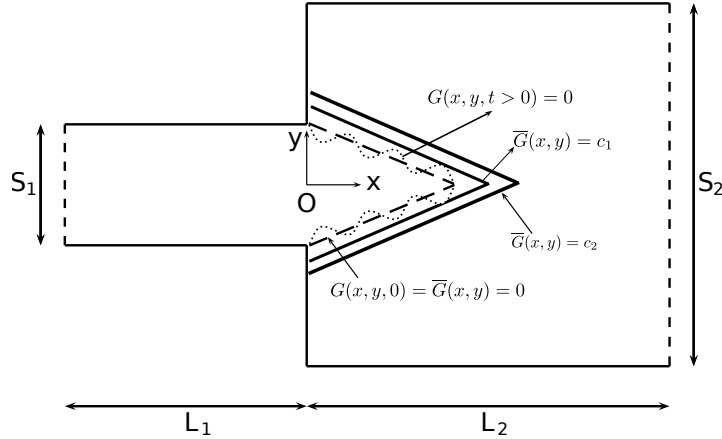
Figure 3.2: Dump combustor with the mean and instantaneous flame isocontours. $\overline{G}(x,y) = c_1$ and c_2 represent different isocontours of the mean level-set $\overline{G}$. $\overline{G}(x,y) = 0$ represents the flame at $t = 0$ (dashed line). The instantaneous flame shape is shown as a dotted line.

When analyzing linear mean flames, such as that in Figure 3.1, we consider a $\overline{G}$ field of the following form:

$$\overline{G}(x, y) = mx - y + \frac{S_1}{2} \tag{3.29}$$

where m is the slope of the mean flame, and S_1 is the height of the smaller duct. Evidently, at $t = 0$ the flame is given by $\overline{G}(x, y) = 0$. We are interested in G' of the following form

$$G'(x, y, t) = e^{i\Omega t} e^{ikx} [\psi_1 \cos(k_y y) + \psi_2 \sin(k_y y)] \tag{3.30}$$

where the amplitudes ψ_1 and ψ_2 are to be determined. At $t > 0$, the flame location (x, y) is obtained from

$$\left[mx - y + \frac{S_1}{2} \right] + e^{i\Omega t} e^{ikx} [\psi_1 \cos(k_y y) + \psi_2 \sin(k_y y)] = 0 \tag{3.31}$$

Substituting Eq. (3.29) into Eq. (3.26), we have

$$\overline{s_T} = \frac{m\overline{u}}{\sqrt{1 + m^2}} \tag{3.32}$$

Using Eqs. (3.22) and (3.32) we can uniquely determine the slope m as follows:

$$\overline{s_T} = \frac{m\overline{u}}{\sqrt{1 + m^2}} = C_1 \overline{\phi}^{C_2} e^{-C_3(\overline{\phi} - C_4)^2} \left(\frac{\overline{T}}{T_0} \right)^{C_5} \left(\frac{\overline{p}}{p_0} \right)^{C_6} \tag{3.33}$$

$$\Rightarrow m = \pm \frac{C_1 \bar{\phi}^{-C_2} e^{-C_3(\bar{\phi}-C_4)^2} \left(\frac{\bar{T}}{T_0}\right)^{C_5} \left(\frac{\bar{p}}{p_0}\right)^{C_6}}{\sqrt{\bar{u}^2 - \left\{C_1 \bar{\phi}^{-C_2} e^{-C_3(\bar{\phi}-C_4)^2} \left(\frac{\bar{T}}{T_0}\right)^{C_5} \left(\frac{\bar{p}}{p_0}\right)^{C_6}\right\}^2}} \tag{3.34}$$

To solve for G', we substitute Eqs. (3.29)-(3.32) into Eq. (3.28) yielding

$$i\Omega \left[\psi_1 \cos(k_y y) + \psi_2 \sin(k_y y)\right] + i\bar{u}k \left[\psi_1 \cos(k_y y) + \psi_2 \sin(k_y y)\right]$$

$$- i\frac{m^2 \bar{u}k}{1+m^2} \left[\psi_1 \cos(k_y y) + \psi_2 \sin(k_y y)\right] + \frac{m\bar{u}k_y}{1+m^2} \left[-\psi_1 \sin(k_y y) + \psi_2 \cos(k_y y)\right]$$

$$= s_T' \sqrt{1+m^2} + \frac{m}{\bar{\rho}} \frac{k}{\Omega + \bar{u}k} \mathscr{C} \cos(k_y y) + \frac{1}{\bar{\rho}} \frac{1}{\Omega + \bar{u}k} k_y \mathscr{C} \sin(k_y y)$$

$$\tag{3.35}$$

Equating the coefficients of $\cos(k_y y)$ and $\sin(k_y y)$, respectively, on both sides of Eq. (3.35) yields two linear algebraic equations in ψ_1 and ψ_2. These can be solved to give

$$\psi_1 = -\mathscr{C}\mathscr{E}_1 \left\{\mathscr{E}_2 + \mathscr{E}_3 \left[\mathscr{E}_4 + \mathscr{E}_5(\mathscr{E}_6 + \mathscr{E}_7)\right]\right\} \tag{3.36}$$

$$\psi_2 = -\mathscr{C}\mathscr{F}_1 \left\{\mathscr{F}_2 \left[\mathscr{F}_3 + \mathscr{F}_4\mathscr{F}_5\right] + \mathscr{F}_6\right\} \tag{3.37}$$

where the terms $\mathscr{E}_1$ through $\mathscr{E}_6$ and $\mathscr{F}_1$ through $\mathscr{F}_6$ are provided in the Appendix C. Substituting ψ_1 and ψ_2 into Eq. (3.30) gives us an expression for G'. Next, we relate G' to the flame surface area fluctuations.

The surface area of a differential element of the flame ($\mathrm{d}A$) of unit depth is given by

$$
\begin{aligned}
\mathrm{d}A &= \sqrt{(\mathrm{d}x)^2 + (\mathrm{d}y)^2} \cdot 1 \\
&= \mathrm{d}y\sqrt{1 + \left(\frac{\frac{\partial G}{\partial y}}{\frac{\partial G}{\partial x}}\right)^2}
\end{aligned}
\tag{3.38}
$$

Splitting $\mathrm{d}A$ into mean and fluctuating components and linearizing it gives

$$
\mathrm{d}\overline{A} = \mathrm{d}y\sqrt{1 + \left(\frac{\frac{\partial \overline{G}}{\partial y}}{\frac{\partial \overline{G}}{\partial x}}\right)^2}
\tag{3.39}
$$

$$
\mathrm{d}A' = \mathrm{d}y\frac{\frac{\partial \overline{G}}{\partial x}\frac{\partial \overline{G}}{\partial y}\frac{\partial G'}{\partial y} - \left(\frac{\partial \overline{G}}{\partial y}\right)^2\frac{\partial G'}{\partial x}}{\left(\frac{\partial \overline{G}}{\partial x}\right)^3\sqrt{1 + \left(\frac{\frac{\partial \overline{G}}{\partial y}}{\frac{\partial \overline{G}}{\partial x}}\right)^2}}
\tag{3.40}
$$

Substituting Eq. (3.29) into Eq. (3.40), we get

$$
\frac{\mathrm{d}A'}{\mathrm{d}\overline{A}} = \frac{-1}{m(m^2+1)}\left(\frac{\partial G'}{\partial x} + m\frac{\partial G'}{\partial y}\right)
\tag{3.41}
$$

which upon the substitution of G' from Eq. (3.30) becomes

$$
\frac{\mathrm{d}A'}{\mathrm{d}\overline{A}} = \underbrace{\frac{\overline{u\rho}(\Omega + k\overline{u})}{k}\left(i\frac{\psi_1 k}{m^3+m} + \frac{\psi_2 k_y}{m^2+1}\right)\frac{u'}{\overline{u}}}_{R_u} + \underbrace{\frac{\overline{u\rho}(\Omega + k\overline{u})}{k_y}\left(\frac{\psi_1 k_y}{m^2+1} - i\frac{\psi_2 k}{m^3+m}\right)\frac{v'}{\overline{u}}}_{R_v}
\tag{3.42}
$$

Equation (3.42) relates the flame surface area fluctuations to the axial and transverse velocity perturbations, with R_u and R_v being the respective response functions.

77

Notice that the transverse velocity perturbation v' is normalized by the mean axial velocity $(\bar{u})$ since $\bar{v} = 0$.

Finally, substituting Eqs. (3.15),(3.20), (3.23) and (3.42) into Eq. (3.6) gives us the flame transfer function:

$$
\begin{aligned}
\frac{\mathrm{d}\dot{Q}'}{\mathrm{d}\bar{\dot{Q}}} &= (R_\rho + R_{\mathrm{HR}} + R_{\mathrm{ST}})\frac{p'}{\bar{p}} + R_u\frac{u'}{\bar{u}} + R_v\frac{v'}{\bar{u}} \\
&= R_p\frac{p'}{\bar{p}} + R_u\frac{u'}{\bar{u}} + R_v\frac{v'}{\bar{u}}
\end{aligned}
\tag{3.43}
$$

where $R_p = R_\rho + R_{\mathrm{HR}} + R_{\mathrm{ST}}$. Figure 3.3 shows a tree diagram representation of the overall flame transfer function (3.43). This figure presents a lucid illustration of how the various sources of fluctuations may all be expressed in terms of the fundamental acoustic fluctuations p', u', and v'.

$\mathrm{d}\dot{Q}'$

ρ' h_r' s_T' $\mathrm{d}A'$

$\boxed{p'}$ T' ϕ' ϕ' T' $\boxed{p'}$ s_T' $\boxed{u'}$ $\boxed{v'}$

$\boxed{p'}$ u' ρ' u' ρ' $\boxed{p'}$ ϕ' T' $\boxed{p'}$

$\boxed{p'}$ $\boxed{p'}$ T' $\boxed{p'}$ $\boxed{p'}$ T' u' ρ' $\boxed{p'}$

$\boxed{p'}$ $\boxed{p'}$ $\boxed{p'}$ $\boxed{p'}$ T'

$\boxed{p'}$

Figure 3.3: A tree diagram representation of the flame transfer function. Fundamental acoustic fluctuations p', u', and v' are enclosed in boxes at the end of all branches.

3.4 Comparison Between Current G-Approach and Prior f-Approach

In this section, we undertake a detailed, quantitative comparison of the G-approach with the f-approach. We demonstrate the conditions under which the two

methods give nearly identical flame surface-area response functions, as well as the situations where they are different. To begin with, we derive the response function relating $dA'/d\overline{A}$ to f', where dA' is the fluctuation in the local flame surface area. While this derivation is motivated by the method outlined in prior studies [13, 39, 45–47, 54, 54], we believe that this is the first time that the additional assumptions and steps needed for the f-approach to handle multi-dimensional fluctuations are explicitly identified.

The level set field G is expressed as $G(x, y, t) = x - f(y, t)$, which upon substitution into Eq. (3.24) yields

$$\frac{\partial f}{\partial t} - u + v\frac{\partial f}{\partial y} = -s_L \sqrt{1 + \left(\frac{\partial f}{\partial y}\right)^2} \tag{3.44}$$

Writing $f = \overline{f} + f'$, $u = \overline{u} + u'$, $v = v'$ (with $\overline{v} = 0$), $s_L = \overline{s_T} + s_T'$ and linearizing, we obtain the following equations for $\overline{f}$ and f'.

$$\overline{u} = \overline{s_T}\sqrt{1 + \left(\frac{d\overline{f}}{dy}\right)^2} \tag{3.45}$$

$$\frac{\partial f'}{\partial t} + \Gamma\frac{\partial f'}{\partial y} = u' - \frac{d\overline{f}}{dy}v' - s_T'\sqrt{1 + \left(\frac{\partial \overline{f}}{\partial y}\right)^2} \tag{3.46}$$

where

$$\Gamma = \frac{\overline{s_T}\,\frac{\mathrm{d}\overline{f}}{\mathrm{d}y}}{\sqrt{1 + \left(\frac{\mathrm{d}\overline{f}}{\mathrm{d}y}\right)^2}}, \tag{3.47}$$

u' and v' are given by Eqs. (3.9) and (3.10) respectively. In Eq. (3.46), $u' = u'(x, y, t)$ and $v' = v'(x, y, t)$, whereas $f' = f'(y, t)$. Since previous studies did not include

e^{ikx} dependence in u' and v' *for the flame response analysis*, this problem had not arisen. For instance, in reference [45] $u' = u_0 e^{i\Omega t}$ (u_0 is constant), i.e., u' did not have any spatial dependence. In studies [47, 54], $u' = \hat{u}(r)e^{i\Omega t}$ only had 1-D (radial) dependence.

This problem may be overcome by considering the velocity fluctuations at the flame $x = f(y, t)$:

$$u'_f(y, t) = -\mathscr{C}\frac{1}{\overline{\rho}}\frac{k}{\Omega + \overline{u}k}e^{ikf(y,t)}\cos(k_y y)e^{i\Omega t} \tag{3.48}$$

$$v'_f(y, t) = \mathscr{C}\frac{1}{\overline{\rho}}\frac{k_y}{\Omega + \overline{u}k}e^{ikf(y,t)}\sin(k_y y)e^{i\Omega t} \tag{3.49}$$

Upon substitution of the above fluctuations into Eq. (3.46), we see that the linearized f' equation becomes non-linear again. Further, the time-dependence is no longer limited to the $e^{i\Omega t}$ term only, but also appears as $e^{ikf(y,t)}$, thereby deviating from the time-periodic nature of acoustic fluctuations. These two issues can be obviated by the approximation $e^{ikf(y,t)} \approx e^{ik\overline{f}(y)}$. Using this approximation in Eqs. (3.48) and (3.49), and considering harmonic temporal dependence for fluctuating quantities i.e., $f'(y, t) = \hat{f}(y)e^{i\Omega t}$, $u'_f(y, t) = \hat{u}_f(y)e^{i\Omega t}$, $v'_f(y, t) = \hat{v}_f(y)e^{i\Omega t}$ and $s'_T(y, t) = \hat{s}_T(y)e^{i\Omega t}$, we can write Eq. (3.46) as

$$\frac{d\hat{f}}{dy} + \frac{i\Omega}{\Gamma}\hat{f} = \frac{1}{\Gamma}\left(\hat{u}_f - \frac{d\overline{f}}{dy}\hat{v}_f - \hat{s}_T\sqrt{1 + \left(\frac{d\overline{f}}{dy}\right)^2}\right) \tag{3.50}$$

From Eq. (3.23), we have

$$\hat{s}_T = \overline{s_T}R_{ST}\frac{\hat{p}}{\overline{p}} \tag{3.51}$$

81

where $\hat{p} = p'/e^{i\Omega t}$. Expressing the pressure fluctuations in terms of the axial velocity fluctuations, we have

$$\hat{s}_T = -\frac{\overline{\rho}}{\overline{p}}\overline{s_T}R_{\text{ST}}\frac{\Omega + \overline{u}k}{k}\hat{u} \tag{3.52}$$

Substituting Eq. (3.52) into Eq. (3.50) and using the boundary condition $\hat{f}(S/2) = 0$, for a linear mean flame $(\overline{f}(y) = \frac{y - S/2}{m})$, $\hat{f}(y)$ is given as

$$\hat{f}(y) = \frac{1}{\Gamma}e^{-i\frac{\Omega}{\Gamma}y}\int_{S/2}^{y} e^{i\frac{\Omega}{\Gamma}\eta}\left\{\left(1 + \frac{\overline{\rho}}{\overline{p}}\overline{s_T}R_{\text{ST}}\frac{\Omega + \overline{u}k}{k}\sqrt{1 + \left(\frac{d\overline{f}}{d\eta}\right)^2}\right)\hat{u}_f(\eta) - \frac{d\overline{f}}{d\eta}\hat{v}_f(\eta)\right\}d\eta \tag{3.53}$$

Multiplying Eq. (3.53) by $e^{i\Omega t}$, we get

$$f(y,t) = \frac{1}{\Gamma}e^{-i\frac{\Omega}{\Gamma}y}\int_{S/2}^{y} e^{i\frac{\Omega}{\Gamma}\eta}\left\{\left(1 + \frac{\overline{\rho}}{\overline{p}}\overline{s_T}R_{\text{ST}}\frac{\Omega + \overline{u}k}{k}\sqrt{1 + \left(\frac{d\overline{f}}{d\eta}\right)^2}\right)u'_f(\eta) - \frac{d\overline{f}}{d\eta}v'_f(\eta)\right\}d\eta \tag{3.54}$$

Flame surface area fluctuations are then given by:

$$\frac{dA'}{d\overline{A}} = \frac{\frac{d\overline{f}}{dy}}{1 + \left(\frac{d\overline{f}}{dy}\right)^2}\frac{\partial f'}{\partial y} = \frac{1}{m^2 + 1}\frac{\partial f'}{\partial y} \tag{3.55}$$

where m is the slope of the mean flame.

Equation (3.55) can be written in terms of velocity response functions as follows:

$$\frac{dA'}{d\overline{A}} = R_{u,f}\frac{u'}{\overline{u}} + R_{v,f}\frac{v'}{\overline{u}} + \psi(y,t) \tag{3.56}$$

82

where

$$R_{u,f} = \frac{\overline{u}}{k\alpha} \left\{ \Omega \left[\overline{\rho} R_{\mathrm{ST}} \overline{u}^2 \left(k^2 \left(m^2 + 2 \right) - k_y^2 m^2 \right) + \left(m^2 + 1 \right) \overline{p} \left(k^2 - i k_y^2 \right) \right] + \right. $$
$$\left. k\overline{u}(k + k_y m)(k - k_y m) \left(\overline{p} + \overline{\rho} R_{\mathrm{ST}} \overline{u}^2 \right) + k \left(m^2 + 1 \right) \overline{\rho} R_{\mathrm{ST}} \overline{u} \Omega^2 \right\} \qquad (3.57)$$

$$R_{v,f} = \frac{\overline{u}}{m\alpha} \left\{ -k^2 \overline{pu} - ik \left(m^2 + 1 \right) \Omega \left[m^2 \overline{\rho} R_{\mathrm{ST}} \overline{u}^2 + \left(m^2 - i \right) \overline{p} \right] + m^2 \overline{u} \left[k_y^2 \overline{p} - i \left(m^2 + 1 \right) \overline{\rho} R_{\mathrm{ST}} \Omega^2 \right] \right\} \qquad (3.58)$$

$$\psi(y,t) = -\frac{\left(m^2 + 1 \right) \Omega}{m\alpha \overline{\rho u}(k\overline{u} + \Omega)} e^{\frac{i\left(m^2 + 1 \right) \Omega (S - 2y)}{2m\overline{u}}} e^{i\Omega t} \cos\left(n\pi \right) \left\{ k^2 \overline{u} \left(\overline{p} + \overline{\rho} R_{\mathrm{ST}} \overline{u}^2 \right) + \right.$$
$$\left. k\Omega \left[\left(m^2 + 1 \right) \overline{p} + \left(m^2 + 2 \right) \overline{\rho} R_{\mathrm{ST}} \overline{u}^2 \right] + i k_y^2 \overline{pu} + \left(m^2 + 1 \right) \overline{\rho} R_{\mathrm{ST}} \overline{u} \Omega^2 \right\} \qquad (3.59)$$

and

$$\alpha = \overline{p} \left(k\overline{u} - k_y m \overline{u} + m^2 \Omega + \Omega \right) \left(k\overline{u} + k_y m \overline{u} + m^2 \Omega + \Omega \right) \qquad (3.60)$$

In Eq. (3.56), the first two terms on the RHS represent the contributions from the flow perturbations, whereas the last term accounts for flame anchoring at $y = S/2$. We will now compare the response functions $R_{u,f}$ and $R_{v,f}$ in Eqs. (3.57) and (3.58) with R_u and R_v in Eq. (3.42).

Comparison of Response Functions

We compare the magnitudes and phases of the response functions R_u and $R_{u,f}$, as well as R_v and $R_{v,f}$. We first compare the response functions for the mixed ($n = 1$) modes, with and without the effects of the turbulent flame-speed fluctuations s_T'. Next, we show the comparison for the axial ($n = 0$) modes. The motivation for

discussing the $n = 1$ modes before $n = 0$ will also be apparent from the discussion that follows.

In Figure 3.4, the response functions R_u and $R_{u,f}$ are compared for the modal index $n = 1$, mean Mach number $\overline{M} = 0.1$, and mean temperature $\overline{T} = 2000$K. Figure 3.4(a) shows the magnitudes of R_u and $R_{u,f}$ as a function of frequency. We can see that their magnitudes are in good agreement at low frequencies ($\Omega < 500$ radians/s), but differ at higher frequencies. It will also become evident from Figure 3.6 that the differences in the magnitudes of R_u and $R_{u,f}$ at higher Ω are, in fact, due to the inclusion of turbulent flame speed fluctuations (s_T'). A more detailed discussion of the response functions trends in Ω is presented elsewhere (see Section 3.5). At this point, we limit ourselves to a quantitative comparison of the two approaches.

Figure 3.4(b) shows the phases of R_u and $R_{u,f}$ as a function of frequency. We see that the phases are both negative, and show oscillations in Ω. The differences in the phases, which increase with frequency, may be attributed to the effects of s_T'. Also shown in Figure 3.4(b) are the phases of R_u and $R_{u,f}$ for the $s_T' = 0$ case (long-dashed line). It is interesting to note that the locus of the intersections of the phases of R_u and $R_{u,f}$ when $s_T' \neq 0$ corresponds to their phase plots when $s_T' = 0$ (the two phases coincide when $s_T' = 0$). Thus, the phases of R_u and $R_{u,f}$ with $s_T' \neq 0$ oscillate about the phases of R_u and $R_{u,f}$ with $s_T' = 0$.
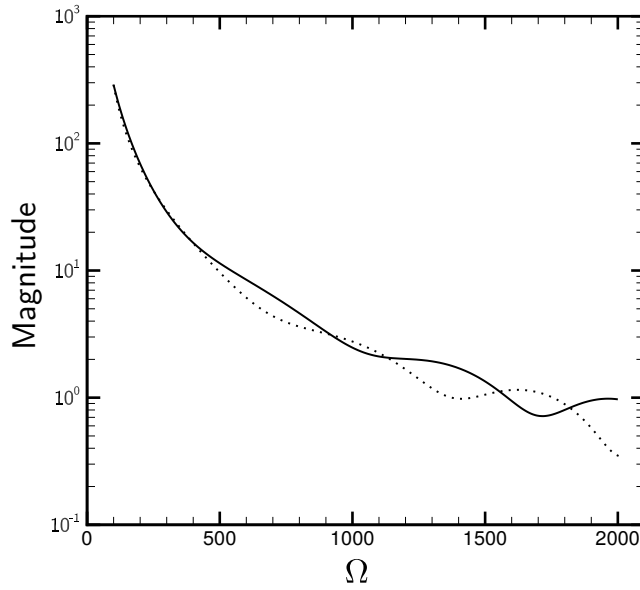
(a)
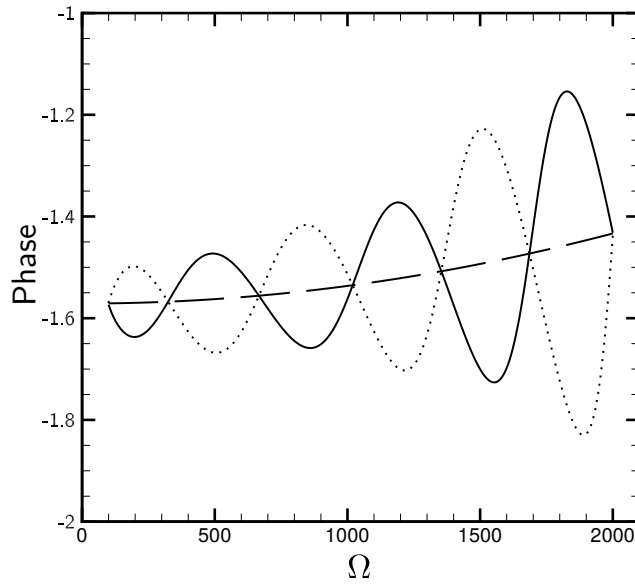
(b)

Figure 3.4: (a) Magnitude and (b) phase of the axial velocity response functions R_u and $R_{u,f}$ for $s'_T \neq 0$ are plotted as a function of frequency (in radians/s). The modal index $n = 1$. R_u: solid line (————); and $R_{u,f}$: dotted line ($\cdots\cdots$). Also shown in (b) are the phases R_u and $R_{u,f}$ for $s'_T = 0$ ($-\,-\,-$).

85

In Figure 3.5, we compare the transverse velocity components of the two flame response functions, R_v and $R_{v,f}$. Figure 3.5(a) shows the magnitudes of R_v and $R_{v,f}$ as a function of frequency. Here we see that the two magnitudes differ at lower frequencies ($\Omega < 500$ radians/s), but are in excellent agreement at higher frequencies (where combustion instabilities typically occur). Figure 3.5(b) compares the phases of R_v and $R_{v,f}$. As with the magnitudes, the phases differ at lower frequencies, but are essentially identical for $\Omega > 500$ radians/s. Also, for $\Omega > 500$, the phases of both R_v and $R_{v,f}$ are nearly zero, indicating that the transverse velocity fluctuations are in phase with the heat-release rate fluctuations.

The differences in the phases of R_u and $R_{u,f}$, and the agreement in the phases of R_v and $R_{v,f}$, can be explained through the contributions of the turbulent flame-speed fluctuations s'_T to the respective response functions. Referring to the G' and f' equations (3.28) and (3.46), respectively, the s'_T source term on the RHS of these two equations is resolved by expressing s'_T in terms of u'. Now, it becomes evident from Eq. (3.30) that the effects of this source term are reflected in both R_u and R_v through the coefficients ψ_1 and ψ_2, respectively. However, from (3.54), we can see that the s'_T term principally influences $R_{u,f}$ and not $R_{v,f}$. This hypothesis can be further illustrated by comparing the two response functions in the absence of s'_T.

Figure 3.6 and Figure 3.7 compare R_u and $R_{u,f}$, and R_v and $R_{v,f}$, respectively, in the absence of s'_T. The magnitudes and phases of the response functions are essentially identical, thereby supporting the above argument on the effects of s'_T. This near perfect agreement between the response functions of G and f approaches, in the absence of s'_T, also suggests that the role of $\psi(y,t)$ in Eq. (3.56) is limited to

the boundary condition. It may therefore be suggested that the explicit imposition of the flame anchoring boundary condition plays a marginal role in determining the flame response to incident fluctuations. In any case, flame anchoring is implicitly achieved through the mean flame that always remains anchored. Given that in linear modal analysis, no such conditions (e.g., no-slip) are explicitly imposed on u' and v' themselves, a specific focus on f' seems not very important.

For the axial $(n = 0)$ modes, R_v and $R_{v,f}$ do not exist. As for the $n = 1$ modes, when $s'_T = 0$, the magnitudes and phases of R_u and $R_{u,f}$ are essentially identical, and hence not shown. In fact, for $n = 0$ and $s'_T = 0$, the magnitudes of R_u and $R_{u,f}$ are independent of frequency, and their phases are zero.

Figure 3.8(a) shows the magnitudes of R_u and $R_{u,f}$ as a function of frequency, with s'_T included. Both R_u and $R_{u,f}$ show periodic oscillations in frequency, but the period of oscillations for $R_{u,f}$ is higher than for R_u. However, the magnitudes of R_u and $R_{u,f}$ have the same upper and lower bounds. Figure 3.8(b) shows the phases of R_u and $R_{u,f}$ as a function of frequency. Both response functions exhibit the familiar saw-tooth like behavior. When compared to R_u, the phase of $R_{u,f}$ changes slowly. This difference in the behavior of the response functions can be attributed to s'_T.

3.5   Results of Flame Response Analysis

In this section, the flame transfer function given by Eq. (3.43) is analyzed for the combustor geometry shown in Figure 3.1. The magnitudes and phases of the various response functions that make up the overall FTF are investigated over a broad parametric space consisting of frequency, mean Mach number, mean temperature,

87
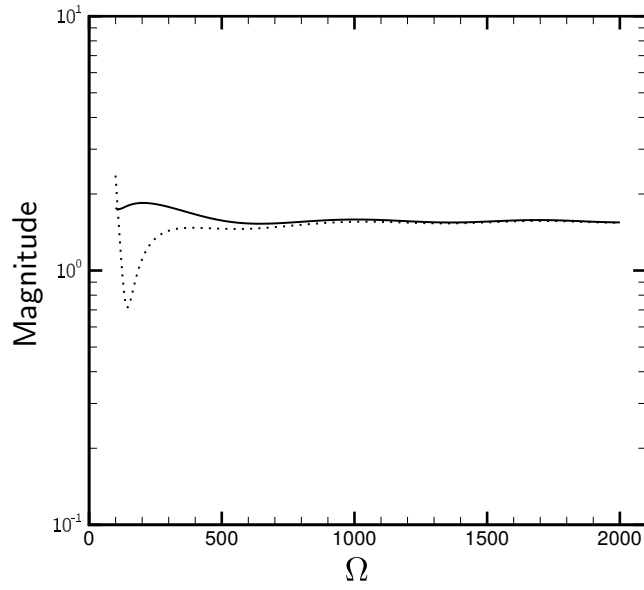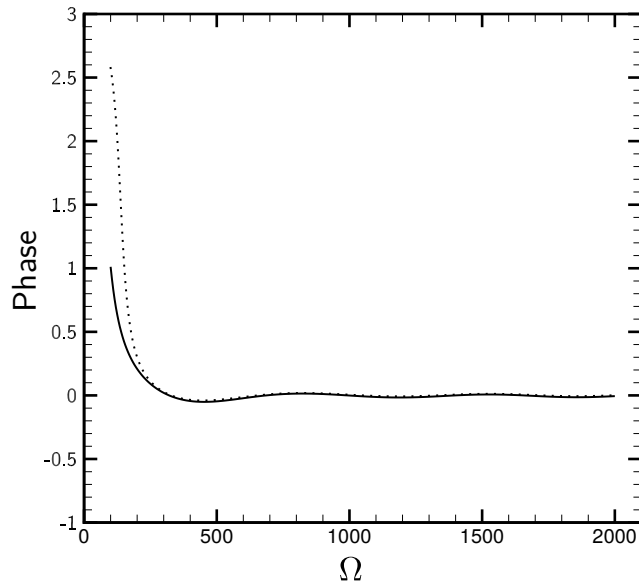
Figure 3.5: (a) Magnitude and (b) phase of the axial velocity response functions R_v and $R_{v,f}$, for $s'_T \neq 0$, are plotted as a function of frequency (in radians/s). The modal index $n = 1$. R_v: solid line (——); and $R_{v,f}$: dotted line ($\cdots\cdots$).
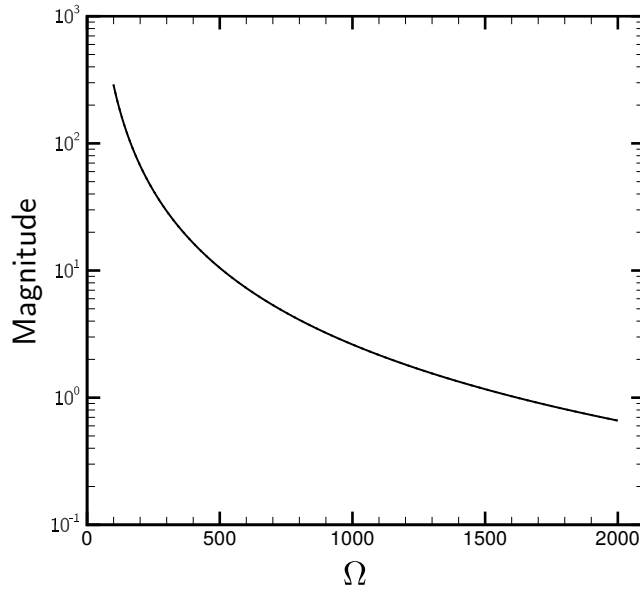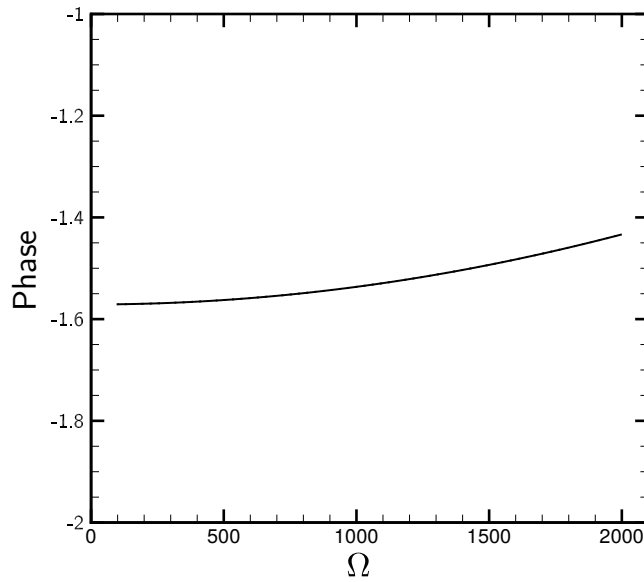
Figure 3.6: (a) Magnitude and (b) phase of the axial velocity response functions R_u and $R_{u,f}$ for $s'_T = 0$ are plotted as a function of frequency (in radians/s). The modal index $n = 1$. R_u: solid line (———); and $R_{u,f}$: dotted line ($\cdots\cdots$).
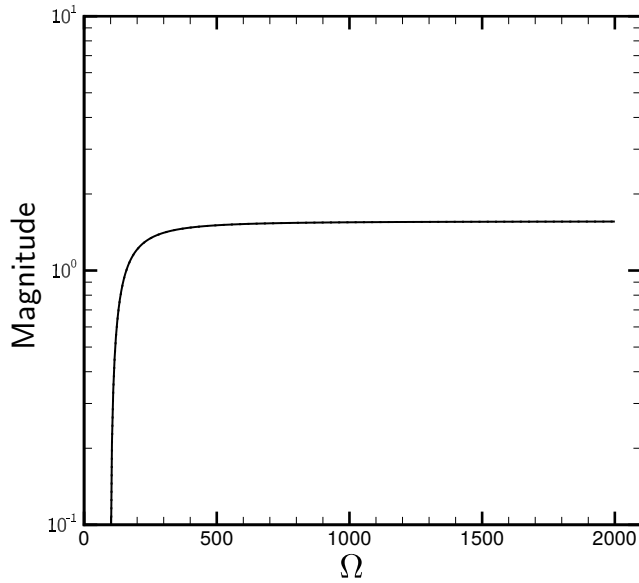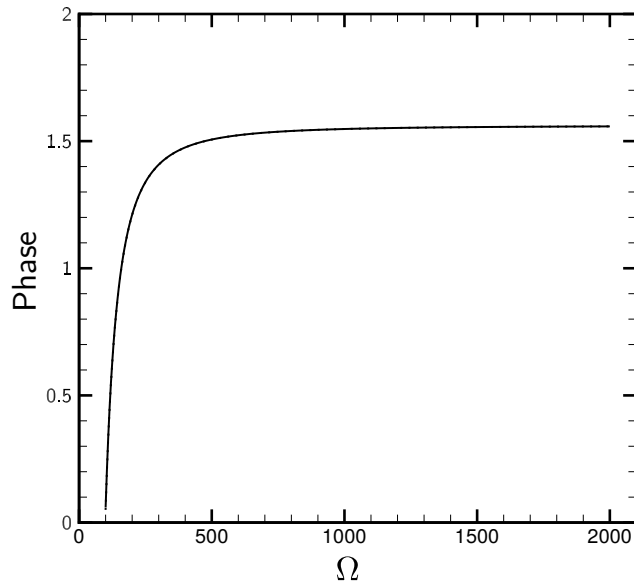
Figure 3.7: (a) Magnitude and (b) phase of the axial velocity response functions R_v and $R_{v,f}$ for $s'_T = 0$ are plotted as a function of frequency (in radians/s). The modal index $n = 1$. R_v: solid line (——); and $R_{v,f}$: dotted line ($\cdots\cdots$).
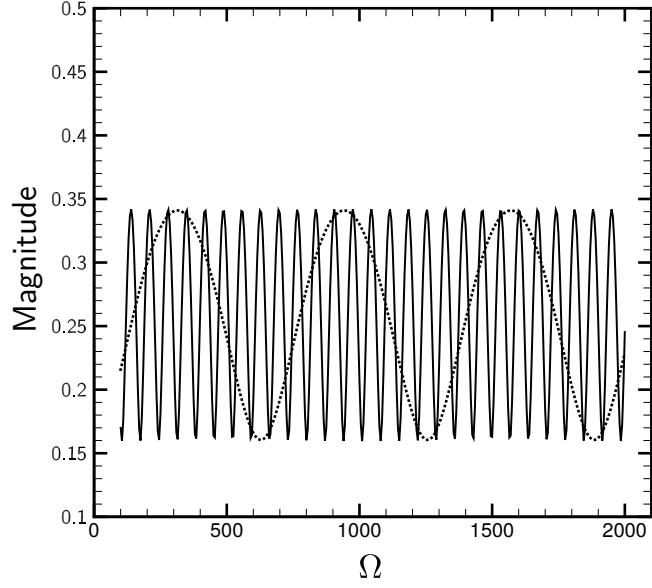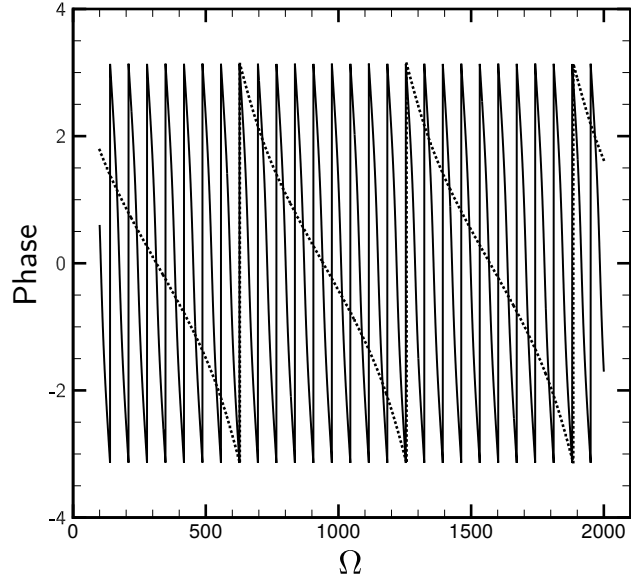
Figure 3.8: (a) Magnitude and (b) phase of the axial velocity response functions R_u and $R_{u,f}$ for $s'_T \neq 0$ are plotted as a function of frequency (in radians/s). The modal index $n = 0$. R_u: solid line (———); and $R_{u,f}$: dotted line ($\cdots\cdots$).

91

and mean equivalence ratio. For each of these parameters, the transfer functions are presented for both purely axial and mixed modes. From this point forward, we only present the results obtained using the current G-equation approach.

3.5.1 Effects of Frequency (Ω)

We begin by considering purely axial modes, i.e. modal index $n = 0$, with duct height $S = 1$m, and the following mean properties: Mach number $\overline{M} = 0.1$, temperature $\overline{T} = 2000$K, and equivalence ratio $\overline{\phi} = 0.8$. In Figure 3.9, the magnitude and phase of the response functions of density, heat of reaction, turbulent flame speed, and axial velocity—R_ρ, R_{HR}, R_{ST}, and R_u, respectively—are shown as a function of frequency (Ω) for the $n = 0$ modes. Note that for purely axial modes, $v' = 0$ and therefore R_v does not arise. Figure 3.9(a) shows the magnitudes of the above four response functions as a function of frequency. It is seen that for the purely axial modes, the magnitudes of R_{ST}, R_ρ and R_{HR} are essentially independent of Ω, whereas the magnitude of R_u shows oscillatory behavior as a function of Ω. The latter behavior suggests that R_u exhibits preferential response to certain frequencies than others. It may be noted that the magnitude of R_ρ is, in fact, larger than the magnitudes of R_{HR} and R_u, suggesting that the $\rho'/\overline{\rho}$ term in Eq. (3.6) may not necessarily be neglected. Also, the magnitude of R_{ST} is the largest among the response functions, due to the contribution of the pressure fluctuations arising from the term $(\partial s_T/\partial p)\, p'$ in Eq. (3.22).

Figure 3.9(b) shows the phases of the four response functions as a function of frequency. The phase-angle range is limited to $[-\pi,\ \pi]$ since we are principally

interested in the fundamental values of the phase angle. For purely axial modes, we can see that the phase of $R_\rho = 0$, i.e. the density fluctuations are always in phase with the heat release fluctuations. This is because there is no convective time-lag term $e^{-i\Omega\tau}$ in the density fluctuations (Eq. (3.15)). The phases of R_{HR}, R_{ST} and R_u show saw-tooth like behavior, characterized by jumps in phase from $-\pi$ to π at regular intervals in Ω. This behavior is due to the convective time-lag term $e^{-i\Omega\tau}$, with τ being a constant for given mean flow conditions. It can also be seen that the phases of R_{ST} and R_u are nearly identical, which is to be anticipated for purely axial modes.

In Figure 3.10, for $n = 1$, the magnitude and phase of R_ρ, R_{HR}, R_{ST}, R_u, as well as of R_v are shown. Figure 3.10(a) shows the magnitudes of these five response functions as a function of frequency. In an averaged sense, R_{ST} has the highest magnitude, followed by R_ρ, R_u, and R_{HR}. These four response functions also broadly decrease as Ω increases. However, the magnitude of R_v oscillates around a fixed value, with the oscillation amplitude decreasing with Ω. The response function magnitudes, except that of R_v, tend toward infinity as the frequency approaches zero, consistent with Boyer and Quinard [39]. The magnitude of R_ρ decreases monotonically with frequency and does not show any oscillations, since R_ρ does not contain the convective lag term $e^{-i\Omega\tau}$. Again, the magnitude of R_ρ is greater than the magnitudes of R_{HR}, R_u and R_v. This is because of the contribution of the temperature flucutuations T' (see Eq. (3.14)) to the second term in R_ρ in Eq. (3.15).

In Figure 3.10(b), the phases of the five response functions are shown as a function of frequency. The phase lines for $-\pi/2$ and $\pi/2$ are also shown by thin solid

93
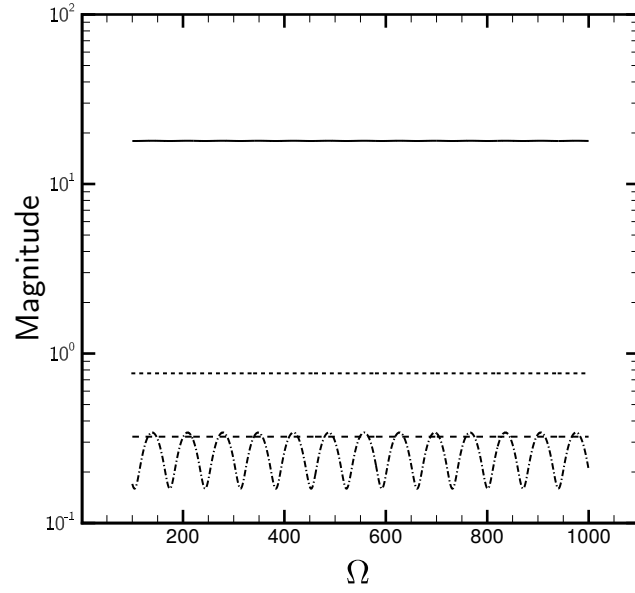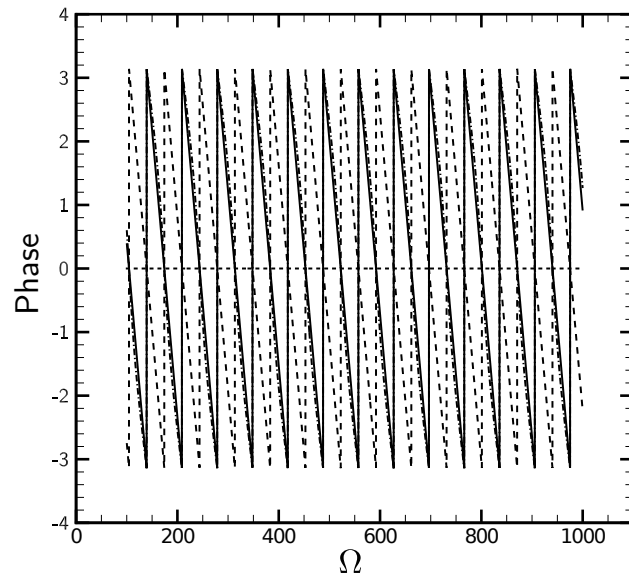
Figure 3.9: (a) Magnitude and (b) phase of the response functions are plotted as a function of frequency (in radians/s) for modal index $n = 0$. R_ρ: dotted line ($\cdots\cdots$); R_{HR}: dashed line ($----$); R_{ST}: solid line (——); and R_u: dash-dot line ($-\cdot-\cdot-$).

94

lines. The phase of R_ρ asymptotes to $-\pi/2$ at zero frequency, and to 0 at infinity frequency, and increases monotonically for frequencies in between. Since the phase of R_ρ is in the range $[-\pi/2, \pi/2]$, $\dot{Q}'$ is always positively correlated to ρ'. The phases of R_{HR} and R_{ST} follow the well-known saw-tooth behavior, with the phase jumping from $-\pi$ to π at regular intervals. At lower frequencies, the phase of R_u shows low-amplitude oscillations about an angle of $+\pi/2$, and approaches the high-amplitude saw-tooth behaviour only for $\Omega > 3000$ radians/s. The phase of R_v is very close to zero, indicating that the transverse velocity fluctuations are nearly in phase with heat-release fluctuations. The asymptoting of the phase of R_ρ to 0 as the frequency tends to infinity, and the transition of the phase of R_u from low-amplitude oscillations to the saw-tooth behavior at higher frequiencies are both more clearly illustrated in Figure 3.11.

3.5.2   Effects of Mean Mach Number $(\overline{M})$

Since $\rho'/\overline{\rho} = R_\rho(p'/\overline{p})$, $h'_r/\overline{h}_r = R_{\mathrm{HR}}(p'/\overline{p})$, and $s'_T/\overline{s}_T = R_{\mathrm{ST}}(p'/\overline{p})$, henceforth, we only present the consolidated pressure response function $R_p = R_\rho + R_{\mathrm{HR}} + R_{\mathrm{ST}}$, as seen in Eq. (3.43). It may be recalled from Figure 3.3 that R_ρ, R_{HR}, and R_{ST} are all eventually expressed in terms of R_p. As a result, it will be seen in the following discussion that R_p dominates R_u and R_v, where R_u and R_v arise solely from the flame surface-area response. A similar observation may also be seen in [46, 47], where $R_{\mathrm{HR}} + R_{\mathrm{ST}}$ is seen to dominate R_u, with R_u arising only from the surface-area response. We also discuss the response functions R_u and R_v, the latter for $n = 1$.
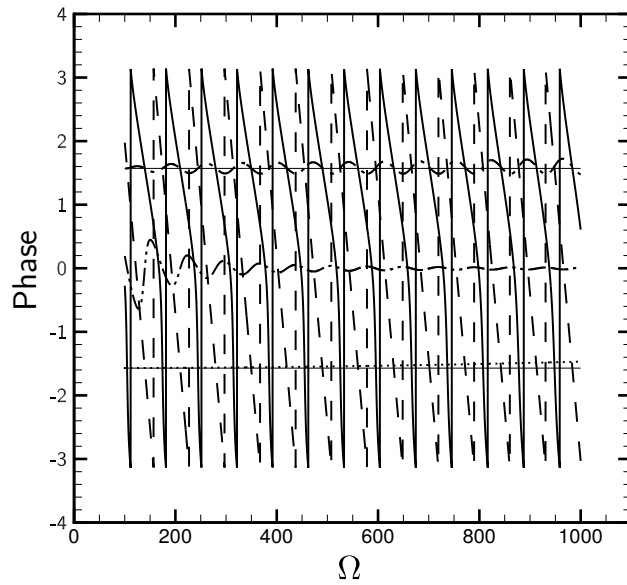
Figure 3.10: (a) Magnitude and (b) phase of the response functions are plotted as a function of frequency (in radians/s) for modal index $n = 1$. R_ρ: dotted line ($\cdots\cdots$); R_{HR}: dashed line ($----$); R_{ST}: solid line (———); R_u: dash-dot line ($-\cdot-\cdot-$); and R_v: dash-dot-dot line ($-\cdots--$).

96
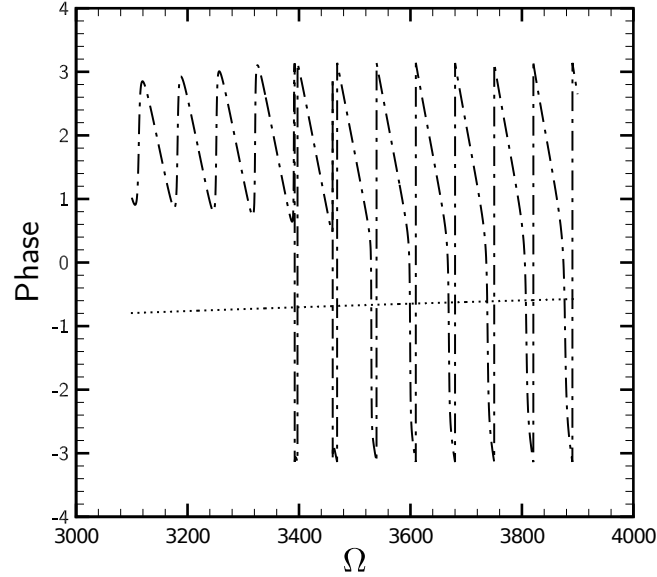
Figure 3.11: Phases of the response functions R_ρ and R_u are plotted as a function of frequency (in radians/s) for modal index $n = 1$. R_ρ: dotted line ($\cdots\cdots$); and R_u: dash-dot line ($-\cdot-\cdot-$).

In Figure 3.12, the magnitudes and phases of the response functions R_p and R_u are shown at a purely axial frequency of 2000 radians/s. Figure 3.12(a) presents the magnitudes of the response functions as a function of the mean inflow Mach number ($\overline{M}$). It can be observed that for lower $\overline{M}$, the magnitude of R_p dominates that of R_u, but for higher $\overline{M}$, their magnitudes approach each other. Further, as $\overline{M}$ goes to zero, the magnitude of R_u approaches zero, while that of R_p tends to infinity. In Figure 3.12(b), it can be seen that the phases of R_p and R_u show very similar variation as a function of $\overline{M}$. Both phases oscillate as a function of $\overline{M}$, with the oscillation frequency decreasing as $\overline{M}$ increases.
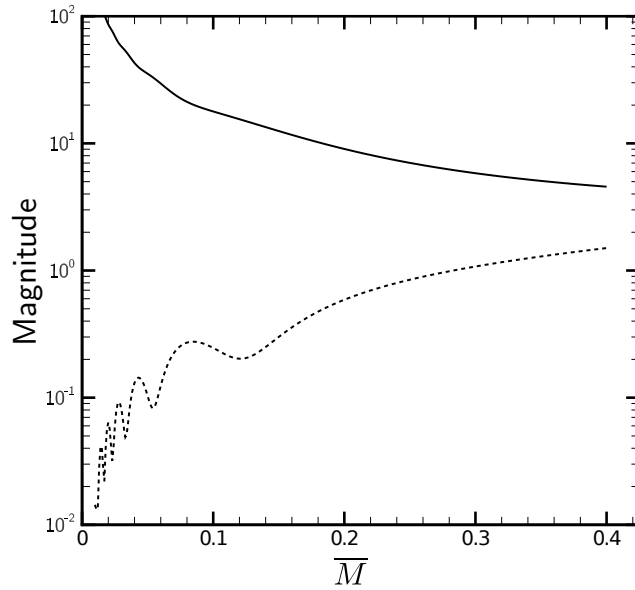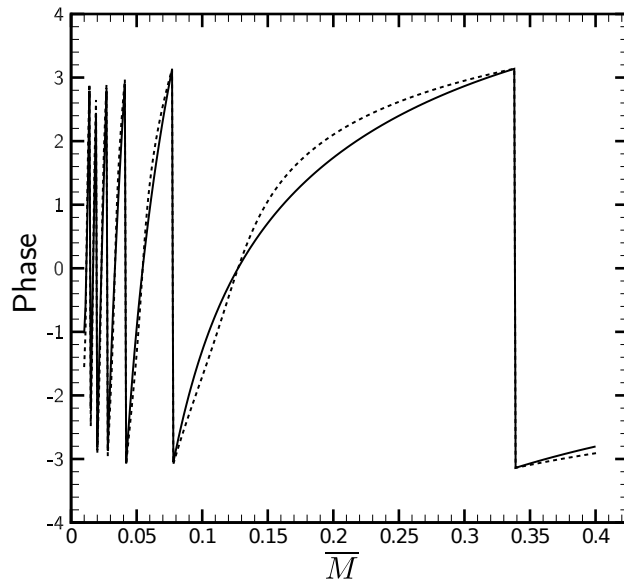
Figure 3.12: (a) Magnitude and (b) phase of the response functions are plotted as a function of mean Mach number for modal index $n = 0$. R_p: solid line (——); and R_u: dotted line (······).

In Figure 3.13, the effects of mean Mach number $\overline{M}$ on the response functions R_p, R_u and R_v at a mixed-mode $(n = 1)$ frequency of 2000 radians/s are shown. Figure 3.13(a) presents their magnitudes as a function of $\overline{M}$. As $\overline{M}$ approaches zero, the magnitude of the pressure response function tends to infinity, whereas those of the axial- and transverse-velocity response functions go to zero. At low Mach numbers $(\overline{M} \lesssim 0.25)$, R_p dominates, while at high Mach numbers $(\overline{M} > 0.25)$, R_v is dominant among the three response functions. The magnitude of R_v increases monotonically with $\overline{M}$, while that of R_u first increases with $\overline{M}$, and then dips around $\overline{M} \sim 0.1$ before increasing again.

In Figure 3.13(b), the phases of the above three response functions are shown as a function of $\overline{M}$. At low $\overline{M}$ $(\lesssim 0.2)$, all three response functions show oscillatory behavior. The phase of R_u is always positive, while that of R_v stays very close to zero. Since a phase angle in the range $-\pi/2 < \theta < \pi/2$ suggests a constructive correlation among flame response and acoustic fluctuations, the transverse velocity fluctuations are positively correlated to heat-release fluctuations at all $\overline{M}$. But, fluctuations in ρ and u show this behavior only for certain values of $\overline{M}$.

3.5.3 Effects of Mean Temperature ($\overline{T}$)

In Figure 3.14, the magnitudes and phases of the response functions R_p and R_u are shown at an axial frequency of 2000 radians/s. In Figure 3.14(a), the magnitudes of the response functions are shown as a function of mean temperature $(\overline{T})$. We see that the magnitudes of both R_p and R_u show oscillations in $\overline{T}$, with the magnitude of R_p being much higher than that of R_u. The frequency of oscillations decreases
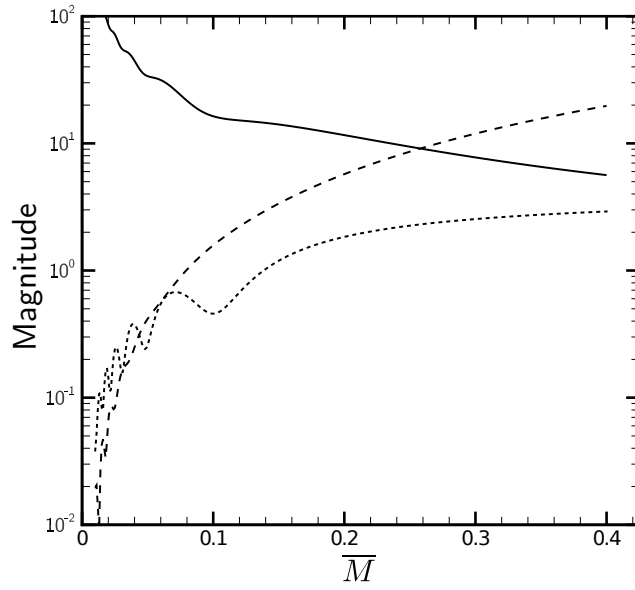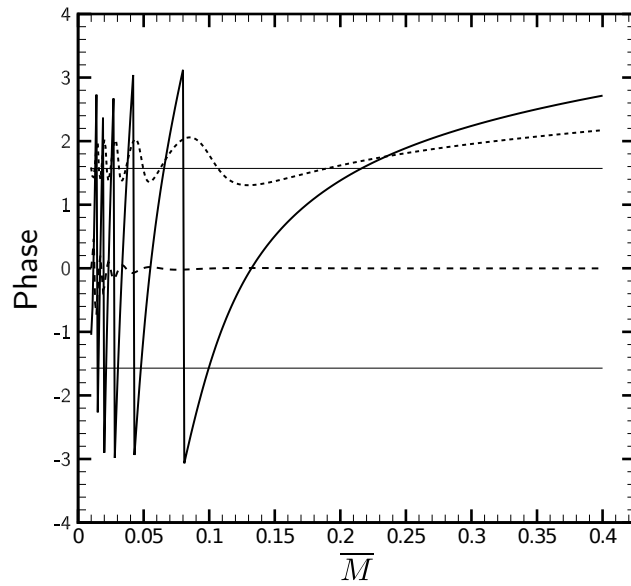
Figure 3.13: (a) Magnitude and (b) phase of the response functions are plotted as a function of mean Mach number for modal index $n = 1$. R_p: solid line (———); R_u: dotted line ($\cdots\cdots$); and R_v: dashed line (– – – -).

with increase in $\overline{T}$. This is because the convective time-lag τ increases with $\overline{T}$. In Figure 3.14(b), the phases of the response functions are shown as a function of $\overline{T}$. It is seen that the phases of both R_p and R_u exhibit saw-tooth behavior and are nearly identical to each other.

Next, we present the magnitudes and phases of the response functions R_p, R_u and R_v at a mixed-mode ($n = 1$) frequency of 2000 radians/s. In Figure 3.15(a), the magnitude of the response functions is shown as a function of mean temperature ($\overline{T}$). The magnitude of R_p is the most dominant among the three response functions. The magnitudes of both R_p and R_u oscillate as a function of $\overline{T}$, whose amplitude increases and frequency decreases with $\overline{T}$. The magnitude of R_u increases and that of R_v decreases with mean temperature. In Figure 3.15(b), the phases of the response functions are shown as a function of $\overline{T}$. The phase of R_p shows saw-tooth-like oscillations with $\overline{T}$, while that of R_u has comparatively smaller amplitude oscillations. For both phases, the oscillation frequency decreases with $\overline{T}$. As before, we observe that the phase of R_v stays very close to zero.

3.5.4 Effects of Mean Equivalence Ratio ($\overline{\phi}$)

We now present the effects of mean equivalence ratio ($\overline{\phi}$) on the magnitudes of the response functions, first for the mixed modes ($n = 1$), and subsequently for the axial modes ($n = 0$) at a frequency of 2000 radians/s. We only present their magnitudes and not the phases, as the trends in the latter are qualitatively similar to those seen previously. In Figure 3.16(a), the magnitudes of the response functions are shown as a function of $\overline{\phi}$ for $n = 1$. For $\overline{\phi} < 1$, i.e. under fuel-lean conditions,
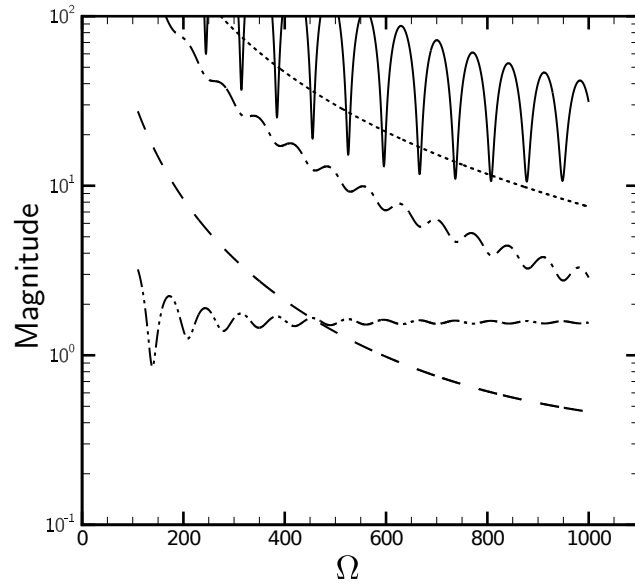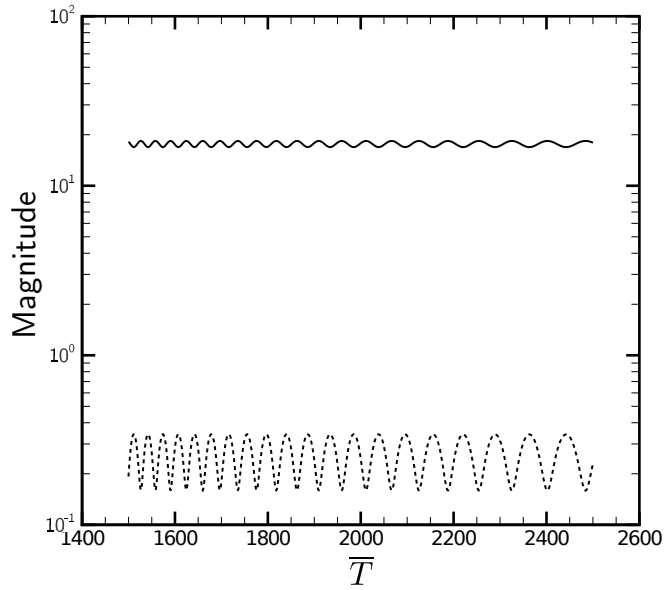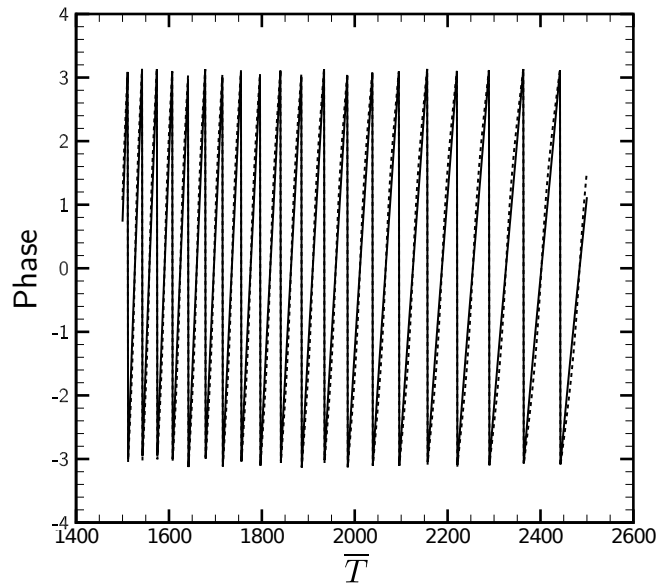
Figure 3.14: (a) Magnitude and (b) phase of the response functions are plotted as a function of mean temperature for modal index $n = 0$. R_p: solid line (———); and R_u: dotted line ($\cdots\cdots$).
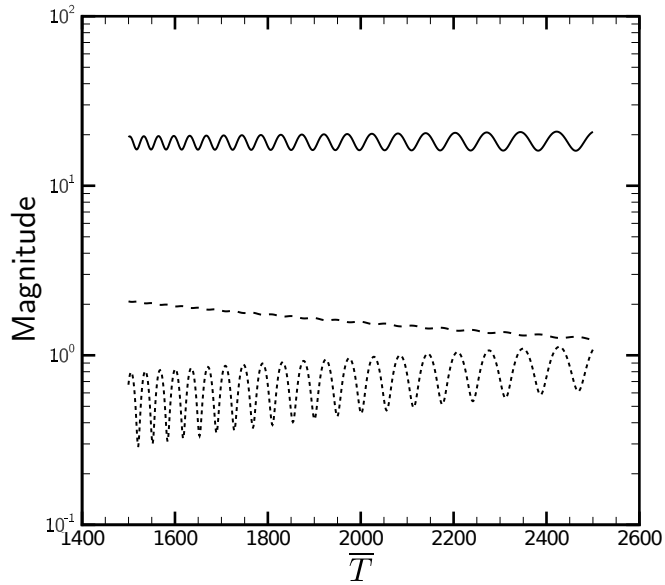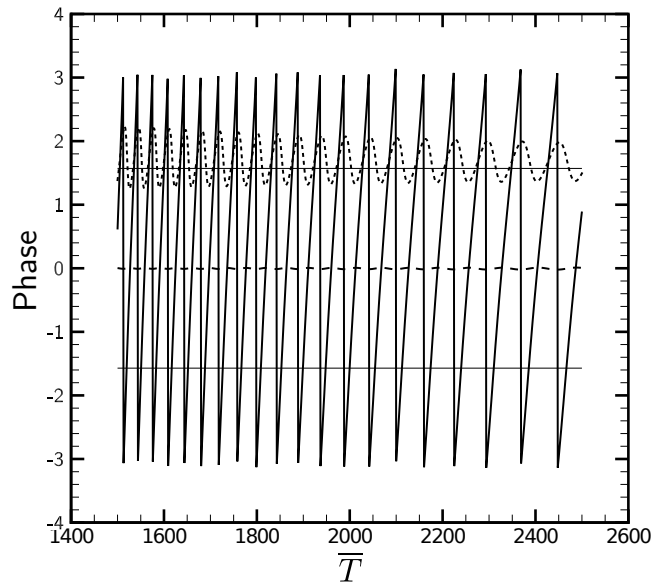
Figure 3.15: (a) Magnitude and (b) phase of the response functions are plotted as a function of mean temperature for modal index $n = 1$. R_p: solid line (———); R_u: dotted line ($\cdots\cdots$); and R_v: dashed line (- - - -).

the magnitudes of R_p and R_v are higher than those for $\overline{\phi} \sim 1$, i.e. at stoichiometric conditions. This is consistent with the observation in prior studies that fuel-lean combustion is prone to instabilities [11, 47, 54]. The magnitude of R_p first decreases for $1 < \overline{\phi} < 1.2$ and then grows sharply for $\overline{\phi} > 1.2$. The sudden increase in the magnitude of R_p at $\overline{\phi} = 1$ is due to the discontinuity of $h_r(\phi)$ at $\phi = 1$ (Eq. (3.16)). The magnitude of R_u is the lowest among the three, and exhibits significantly smaller variation with $\overline{\phi}$ including a rather slow increase for $\overline{\phi} > 1$. Both R_p and R_u show high-frequency oscillations with $\overline{\phi}$, except around $\overline{\phi} \sim 1$. The magnitude of R_v does not oscillate with $\overline{\phi}$, and shows a sharp increase only for $\overline{\phi} > 1.6$. In Figure 3.16(b), the magnitudes of R_p and R_u are shown as a function of $\overline{\phi}$ for $n = 0$. It is seen that the dependence of R_p and R_u on $\overline{\phi}$ is qualitatively similar to that for mixed modes. However, the oscillations in the magnitudes for $n = 0$ have smaller amplitude than the those for $n = 1$. This observation is consistent with that in [54].

3.6 Combustion Instability Analysis using the FTF

In a prior study [23], the current authors developed an acoustically consistent modal analysis approach for predicting combustion instabilities. In that study, novel jump or matching conditions at the cross-sectional interfaces were presented such that the analytically known dispersion relations for the axial acoustic modes of ducts with multiple discontinuities are consistently recovered. Furthermore, the effects of the fluctuating heat-release source term in the acoustic wave equation were incorporated directly into the axial wavenumber, obviating the need for a separate energy matching condition across the flame. The derived FTF was incorporated into
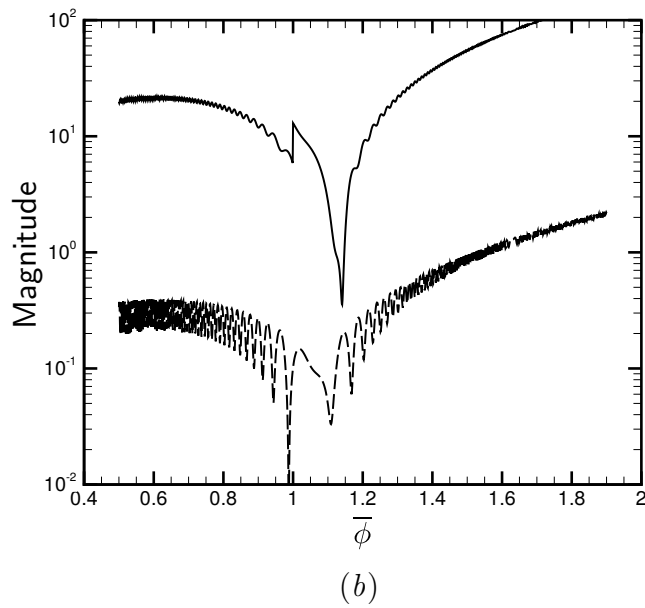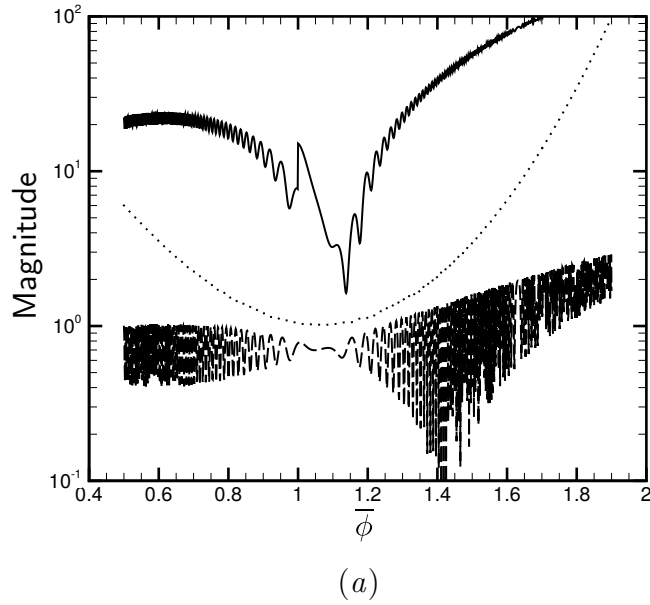
Figure 3.16: Magnitudes of the response functions for (a) mixed modes ($n = 1$) and (b) purely axial modes ($n = 0$) are plotted as a function of mean equivalence ratio. R_p: solid line (———); R_u: dashed line (– – – –); and R_v: dotted line ($\cdots\cdots$).

this modal analysis framework to predict instabilities in a 2-D dump combustor. For completeness, the salient features of the modal analysis are presented in the following discussion.

The inhomogeneous wave equation with the fluctuating heat-release source term included is given by [4, 23]:

$$\frac{1}{\bar{c}^2}\frac{\overline{D}^2 p'}{\overline{Dt}^2} - \nabla^2 p' = \frac{\gamma - 1}{\bar{c}^2}\frac{\overline{D}\dot{q}'}{\overline{Dt}} \tag{3.61}$$

where

$$\frac{\overline{D}}{\overline{Dt}} = \frac{\partial}{\partial t} + \overline{\mathbf{u}} \bullet \nabla$$

fluctuating heat-release rate per unit volume $\dot{q}' = 2\frac{\overline{Q}}{L_f S}\frac{\mathrm{d}\dot{Q}'}{\mathrm{d}\bar{\dot{Q}}}$, $\overline{\mathbf{u}}$ is the mean velocity vector, and γ is the ratio of specific heats. Here $\overline{Q} = \overline{\rho s_T} \overline{h_r}\,\overline{A}$ is the mean heat-release rate ($\overline{A}$ is the total mean flame surface area), and $\frac{\mathrm{d}\dot{Q}'}{\mathrm{d}\bar{\dot{Q}}}$ is obtained from the RHS of Eq. (3.43).

The combustor under consideration is divided into three zones as shown in Figure 3.1. The acoustic fluctuations in each of these zones are given by [5, 10, 14, 23, 54]:

$$p'_\beta(x, y, t) = e^{i\Omega t} \sum_{n=0}^{\infty} \left(A_{n,\beta}^+ e^{ik_{n,\beta}^+ x} + A_{n,\beta}^- e^{ik_{n,\beta}^- x} \right) \cos\left(k_{y,\beta}\, y\right)$$

$$\rho'_\beta(x, y, t) = \frac{1}{\bar{c}_\beta^2} e^{i\Omega t} \sum_{n=0}^{\infty} \left(A_{n,\beta}^+ e^{ik_{n,\beta}^+ x} + A_{n,\beta}^- e^{ik_{n,\beta}^- x} \right) \cos\left(k_{y,\beta}\, y\right)$$

$$u'_\beta(x, y, t) = -\frac{1}{\bar{\rho}_\beta} e^{i\Omega t} \sum_{n=0}^{\infty} \left(\frac{k_{n,\beta}^+}{\Omega + \overline{u}_\beta k_{n,\beta}^+} A_{n,\beta}^+ e^{ik_{n,\beta}^+ x} + \frac{k_{n,\beta}^-}{\Omega + \overline{u}_\beta k_{n,\beta}^-} A_{n,\beta}^- e^{ik_{n,\beta}^- x} \right) \cos\left(k_{y,\beta}\, y\right)$$

$$v'_\beta(x, y, t) = \frac{1}{\bar{\rho}_\beta} e^{i\Omega t} \sum_{n=0}^{\infty} \left(\frac{k_{y,\beta}}{\Omega + \overline{u}_\beta k_{n,\beta}^+} A_{n,\beta}^+ e^{ik_{n,\beta}^+ x} + \frac{k_{y,\beta}}{\Omega + \overline{u}_\beta k_{n,\beta}^-} A_{n,\beta}^- e^{ik_{n,\beta}^- x} \right) \sin\left(k_{y,\beta}\, y\right)$$

$$\tag{3.62}$$

106

where $\beta = 1, 2, 3$ is the zonal index, $k_{y,\beta} = 2n\pi/S_\beta$ (S_β is the duct height of zone β), and $A_n^\pm$ and $k_n^\pm$ are the amplitudes and axial wavenumbers, respectively, of the waves propagating in the positive and negative x-directions. The forms of $k_n^\pm$ depend upon the mean velocity profile, as well as the flame response function.

3.6.1 Matching Conditions at Zonal Interfaces

The acoustically consistent matching conditions presented in [23] are applied at the zonal interfaces. This approach involves only the velocity and pressure matching conditions with distinct forms for the axial and nonaxial modes, and no separate energy matching condition.

For the axial modes, the velocity matching condition imposes the continuity of acoustic mass velocity ($\int_S \rho u \ dy$). At the interface between zones 1 and 2, this is given by

$$\int_{S_1} \rho_1 u_1 \ dy \ = \ \int_{S_2} \rho_2 u_2 \ dy \tag{3.63}$$

which after linearization yields

$$\int_{S_1} [\rho_1' \overline{u}_1 + \overline{\rho}_1 u_1'] \ dy = \int_{S_2} [\rho_2' \overline{u}_2 + \overline{\rho}_2 u_2'] \ dy \tag{3.64}$$

Since the fluctuating quantities are being integrated across their respective zonal cross-sections, only the zeroth-mode (purely axial) contribution remains. Accordingly,

the velocity matching condition for the purely axial modes is given by:

$$[\rho_1^{(0)} \, \overline{u}_1 + \overline{\rho}_1 \, u_1^{(0)}] \, S_1 \;=\; [\rho_2^{(0)} \, \overline{u}_2 + \overline{\rho}_2 \, u_2^{(0)}] \, S_2 \qquad (3.65)$$

where the superscript (0) represents the zeroth mode $(n = 0)$ of a fluctuating quantity. For the axial modes, the pressure matching condition is

$$\int\limits_{S_1} \left\{ p_1' + \overline{\rho}_1 \, \overline{u}_1 \, u_1' + \frac{1}{2}\rho_1' \, \overline{u}_1 \, \overline{u}_1 \right\} dy = \int\limits_{S_1} \left\{ p_2' + \overline{\rho}_2 \, \overline{u}_2 \, u_2' + \frac{1}{2}\rho_2' \, \overline{u}_2 \, \overline{u}_2 \right\} dy \quad (3.66)$$

In the above equation, the integrations on the LHS and RHS are over the cross-sectional interface or the aperture between the two zones, resluting in different be-haviors on the two sides of the equation. While only the axial mode $(n = 0)$ terms remain on the LHS, both axial and non-axial modes $(n \neq 0)$ contribute to the RHS. For calculating the axial modes, the pressure matching condition involves only the $n = 0$ terms on the RHS.

For the non-axial modes $(n > 0)$, the velocity matching condition is given by:

$$u_1' = u_2' \qquad (3.67)$$

and, the pressure matching condition is :

$$p_1' + \overline{\rho}_1 \, \overline{u}_1 \, u_1' + \frac{1}{2}\rho_1' \, \overline{u}_1 \, \overline{u}_1 = p_2' + \overline{\rho}_2 \, \overline{u}_2 \, u_2' + \frac{1}{2}\rho_2' \, \overline{u}_2 \, \overline{u}_2 \qquad (3.68)$$

For the non-axial modes, Eqs. (3.67) and (3.68) contains an infinite series summation on both the LHS and RHS. We reduce this complexity by utilizing the orthogonality property of the cosine function, where Eqs. (3.67) and (3.68) are multiplied with $\cos\left(\frac{2N\pi}{S_1}y\right)$ ($N > 0$ is an integer), and integrated over $y \in [-S_1/2, S_1/2]$ (The final forms of the matching conditions are not reproduced here. See [23]). The preceding matching conditions for the axial and non-axial modes are also applied at the interface between zones 2 and 3.

3.6.2   Mean Velocity Profiles and Heat-Release Term

As discussed previously, the form of the axial wavenumbers $k_n^\pm$ depends on the mean velocity profile (and the heat-release source term). For a uniform mean velocity with no heat release, the axial wavenumbers have the following well-known form:

$$k_n^\pm = \frac{\frac{\Omega\overline{M}}{\overline{c}} \mp \sqrt{\frac{\Omega^2}{\overline{c}^2} - (1 - \overline{M}^2)(\frac{2n\pi}{S})^2}}{1 - \overline{M}^2} \tag{3.69}$$

For nonuniform axial mean flow, $k_n^\pm$ are obtained using the following wave equation [23]:

$$\frac{1}{\overline{c}^2}\frac{\partial^2 p'}{\partial t^2} + \frac{2\overline{M}(y)}{\overline{c}}\frac{\partial^2 p'}{\partial t\partial x} + \left[\overline{M}^2(y) - 1\right]\frac{\partial^2 p'}{\partial x^2} - \frac{\partial^2 p'}{\partial y^2} = 2\overline{\rho}\frac{d\overline{u}}{dy}\frac{\partial v'}{\partial x} + \frac{\gamma - 1}{\overline{c}^2}\left(\frac{\partial \dot{q}'}{\partial t} + \overline{u}\frac{\partial \dot{q}'}{\partial x}\right) \tag{3.70}$$

where $\bar{u} = \bar{u}(y)$ and $\overline{M} = \overline{M}(y)$. The three mean velocity profiles considered in this study are:

$$\text{Uniform Velocity Profile :} \quad \bar{u} \quad = \quad \overline{M}_{\text{bulk}}\, \bar{c} \tag{3.71}$$

$$\text{Parabolic Velocity Profile :} \quad \bar{u}(y) \quad = \quad \frac{6\overline{M}_{\text{bulk}}\, \bar{c}}{S^2}\left(\frac{S^2}{4} - y^2\right) \tag{3.72}$$

$$\text{Turbulent Velocity Profile :} \quad \bar{u}(y) \quad = \quad \overline{M}_{\text{bulk}}\, \bar{c}\left(1 - \frac{4y^2}{S^2}\right)^{\frac{1}{7}} \tag{3.73}$$

where $\overline{M}_{\text{bulk}}$ is the bulk Mach number of the flow.

Substituting the pressure, velocity, and heat-release rate fluctuation forms, as well as $\bar{u}(y)$ into Eq. (3.70), we get an equation in k_n. Solving this equation yields the appropriate forms of $k_n^{\pm}$ (see [23] for details).

3.7 Results of Combustion Instability Analysis

3.7.1 Validation

The model analysis approach combined with the FTF is validated using the experimental and theoretical combustion instability predictions of Yu et al. [2]. Yu et al. [2] considered a 1-D planar flame located downstream of the area discontinuity, as shown in Figure 4.10. The geometric parameters and mean flow properties in the Yu et al. study are provided in Table 4.2, and are used for validating the current approach as well.

In Table 4.4, the unstable longitudinal mode frequencies predicted by our approach are compared with those from Yu et al. [2]. It can be seen that the current
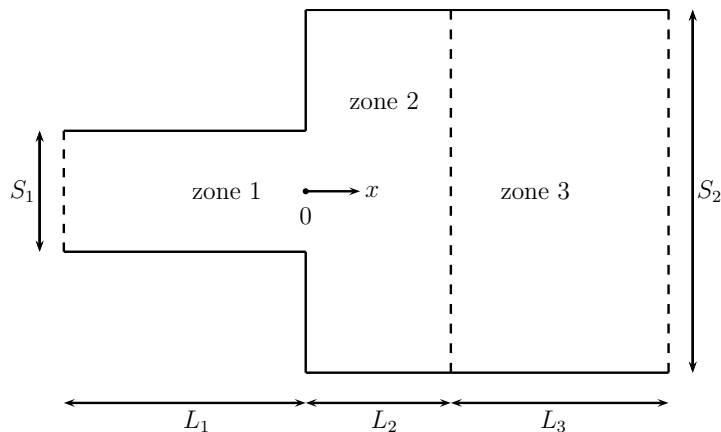
Figure 3.17: Geometry of the dump combustor considered by Yu et al., with the planar mean flame shape indicated using dashed line separating zones 2 and 3.

Table 3.1: Geometric parameters and mean flow properties in the three-zone dump combustor (see Figure 4.10) considered in Yu et al. [2].

Geometry/Mean Property	Zone 1	Zone 2	Zone 3
Length (m)	0.171	0.038	0.215
Height (m)	0.0225	0.0450	0.0450
Mach number, $\overline{M}$	0.265	0.0548	0.0933
Temperature, $\overline{T}$ (K)	1020	1030	2660
Speed of sound, $\bar{c}$ (ms^{-1})	698	701	1110
Density, $\bar{\rho}$ (kg·m^{-3})	7.53	5.92	2.20
Pressure, $\bar{p}$ (MPa)	2.27	2.29	2.28

instability predictions agree better with the experimental data than do the modal analysis results of Yu et al. The difference between the current and experimental frequencies is less than 3%. These improved predictions may be attributed to the comprehensive FTF developed in this study, as well as the acoustically consistent modal analysis.

Table 3.2: Comparison of unstable longitudinal mode frequencies obtained by using the current FTF with those from the experiments and 1-D modal analysis of Yu et al. [2].

Frequency (Hz)	Experimental (Yu et al.)	1-D Analytical (Yu et al.)	Modal Analysis (Using Current FTF)
Fundamental (Ω_{10})	1905	1997	1859
First harmonic (Ω_{20})	3890	3785	3895
Second harmonic (Ω_{30})	5610	5878	5760

3.7.2 Application to 2-D Dump Combustor

In studying the effects of mean velocity on instability modes, we considered three profiles: uniform (Eq. (3.71)), laminar parabolic (Eq. (3.72)), and turbulent 1/7th power law profiles (Eq. (3.73)). For each of these profiles, the mean flame shape was determined by writing $\overline{G}(x,y) = x - \overline{f}(y)$, and then substituting this into Eq. (3.26). This gives us

$$\overline{f}(y) = \mp \int_{S/2}^{y} \sqrt{\frac{\overline{u}(y)^2}{\overline{s_T}^2} - 1} \, \mathrm{d}y \tag{3.74}$$

Figure 3.18 shows the upper half of the calculated mean flame shape, $x - \overline{f}(y) = 0$, for the three mean velocities. For the uniform and parabolic profiles, $\overline{s_T}$ in Eq. (3.74) is simply replaced by a laminar flame speed that is again obtained from Eq. (3.21). The mean properties considered are: $\overline{T} = 2000\mathrm{K}$, $\overline{M}_{\mathrm{bulk}} = 0.1$, $\overline{p} = 5.7$ bar and, $\overline{\phi} = 0.8$. The inlet duct height $S_1 = 1\mathrm{m}$. As expected, the mean flame shape is linear for the uniform mean flow case. For the turbulent mean velocity case, the flame

shape far away from the flame anchoring point is essentially linear and parallel to the flame for the uniform flow case. This behavior is to be anticipated since the turbulent power-law profile varies slowly with y in the core of the duct (i.e., essentially behaves like a uniform flow). Close to the anchoring point, the shape becomes non-linear. The mean flame shape for the parabolic velocity profile is much more non-linear than for the turbulent velocity profile. Defining the flame length L_f as the x for which $\overline{G}(x,0) = 0$, it can be seen that the uniform and parabolic velocity profile cases have the same flame length, while the turbulent velocity profile case has the lowest flame length.

Prediction of Combustion Instabilities

The geometric parameters and mean conditions for the dump combustor (Figure 3.1) are given in Table 3.3. It should be noted that for the uniform and parabolic mean velocity profiles, $L_f = 8.6$m, and for the turbulent velocity profile $L_f = 7.9$m. Acoustically closed boundary conditions ($\frac{\partial p'}{\partial x}\big|_{x=-L_1,\ L_2} = 0$) are imposed at the inlet and exit of the combustor. In Table 3.4, we present the unstable longitudinal and transverse modes for the three mean flame shapes. Also presented in Table 3.4 are the nominal growth rates, i.e. the imaginary part of the complex frequency, which is negative for unstable modes. It is evident that the mean velocity profile does not significantly impact the unstable frequencies, at least for the mean conditions considered here.
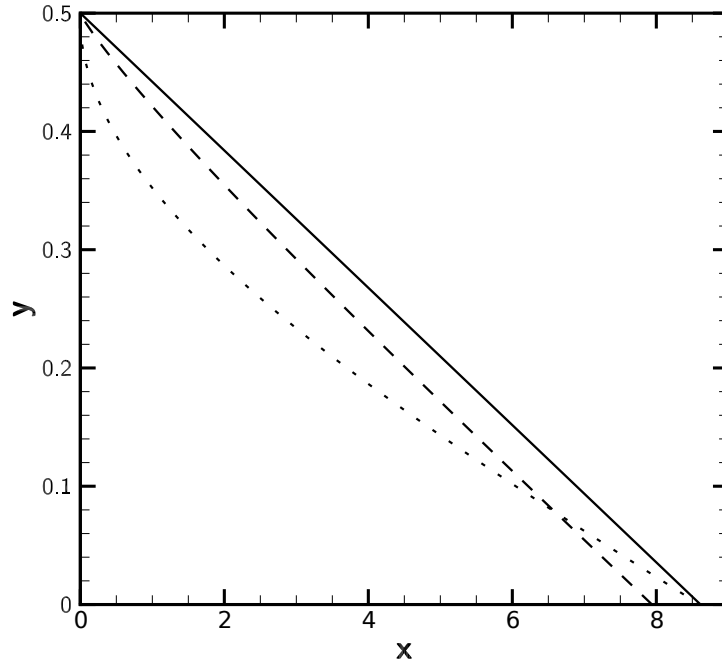
Figure 3.18: Mean flame shape for three mean velocity profiles: uniform (———), parabolic (······), and turbulent (– – – –), are shown. The flame anchoring point is $(0, 0.5)$.

Table 3.3: Geometric parameters and mean flow properties in the three-zone dump combustor (see Figure 3.1) considered in this study.

Geometry/Mean Property	Zone 1	Zone 2	Zone 3
Length (m)	1	L_f	$10 - L_f$
Height (m)	1	2	2
Bulk Mach number, $\overline{M}_{\text{bulk}}$	0.1	0.035	0.032
Temperature, $\overline{T}$ (K)	1000	2000	2500
Equivalence ratio, $\overline{\phi}$	0.8	0.4	0.05
Density, $\overline{\rho}$ (kg·m^{-3})	7.53	5.92	2.20
Pressure, $\overline{p}$ (MPa)	2.27	2.29	2.28

Table 3.4: Unstable longitudinal and transverse mode frequencies for the dump combustor (Figure 3.1) with three mean flame shapes due to uniform, parabolic, and turbulent mean velocity profiles.

Acoustic Modes	Uniform		Parabolic		Turbulent	
(radians/s)	Frequency Ω_{real}	Growth rate Ω_{imag}	Frequency Ω_{real}	Growth rate Ω_{imag}	Frequency Ω_{real}	Growth rate Ω_{imag}
Fundamental (Ω_{10})	261.79	-7.84	261.72	-7.86	264.71	-7.70
First harmonic (Ω_{20})	517.86	-10.46	517.71	-10.48	520.80	-9.79
Second harmonic (Ω_{30})	762.30	-14.30	763.07	-14.3	763.30	-13.41
Fundamental transverse (Ω_{01})	2758.00	-15.18	2757.24	-15.22	2768.82	-15.19

3.8 Summary

A comprehensive flame transfer function for turbulent premixed flames is presented. The FTF includes the effects of fluctuations in density, heat of reaction, turbulent flame speed, and flame surface area. Flame surface-area response to acoustic fluctuations is formulated using a novel G-equation method. This approach facilitates the consistent inclusion of the effects of 2-D/3-D acoustic-perturbations and 2-D/3-D flame-kinematics on the FTF. A detailed comparison between the current G-approach and the well-established f-approach is presented. In the absence of turbulent flame-speed fluctuations, the two approaches give nearly identical response functions. However, they differ when turbulent flame-speed fluctuations are included, principally in the phase of the axial velocity response functions. A detailed analysis of the current FTF was undertaken for a V-shaped mean flame, wherein the effects of varying the frequency, modal index, mean Mach number, mean temperature, and mean equivalence ratio were studied. For the purely axial modes, it was found that

the magnitude of the response functions corresponding to fluctuations in density, heat of reaction, flame speed, and flame surface area are largely unaffected by the frequency, except for low-amplitude harmonic-like oscillations. For mixed modes, the magnitudes of these response functions scale inversely with frequency, along with the harmonic-like oscillations. This suggests that for mixed modes the flame acts like a high-pass filter. From the phase analysis, it was observed that R_ρ and R_v are always positively correlated with heat-release-rate fluctuations. At any given frequency, the magnitudes of the response functions are lowest around the stoichiometric mean equivalence ratio ($\overline{\phi} \sim 1$). By combining the FTF with an acoustically consistent modal analysis framework, combustion instability analysis of a 2-D dump combustor was performed for three mean velocity profiles. For a given bulk Mach number, the mean velocity profiles do not seem to have much effect on the unstable mode frequencies.

CHAPTER 4

PREDICTION OF COMBUSTION INSTABILITIES USING A WKB-TYPE SOLUTION FOR THE WAVE EQUATION IN INHOMOGENEOUS MEDIA

4.1   Abstract

Linear modal analysis is a widely used reduced-order method to predict combustion instabilities. However, this method is only applicable under the assumption that a combustion system is comprised of chambers with homogeneous mean-flow properties. A well-known analytical solution approach to the one-dimensional (1-D) wave equation in inhomogeneous media is the Wentzel-Kramers-Brillouin (WKB) method, which is based on the assumptions of high frequency and slowly varying flow properties. In this study, a novel WKB-type methodology is developed by relaxing the latter assumption. Solutions are derived for the quasi 1-D wave equation in ducts with varying cross-sectional area and inhomogeneous mean-flow properties. Numerical simulations of the wave equation were also performed. Both the current and classical WKB solutions are compared with the numerical results, as well as known exact solutions. The WKB solution is then applied to predict the longitudinal instabilities in a dump combustor with an area discontinuity. The predicted unstable

frequencies are found to be in good agreement with prior experimental and analytical results.

4.2   Introduction

A fundamental consideration in the design and operation of propulsion and power generation systems is the occurrence of combustion instabilities. Combustion instabilities manifest as self-excited acoustic oscillations arising from the constructive interference between the heat-release rate fluctuations and the acoustic perturbations inside the combustor [22, 23]. Reduced-order analytical models for the prediction of instabilities entail two broad steps—the solution of the acoustic wave equation, and the incorporation of the thermo-acoustic interactions through a flame response function [4, 5, 7, 11, 14, 23]. Linear modal analysis is one of the widely used reduced-order methods for computing the resonant frequencies of a combustion chamber. In modal analysis, the geometry of interest is first divided into zones with uniform mean-flow properties. Matching conditions are then imposed on the wave solutions (in adjacent zones) at the zonal interfaces [2, 23, 54]. However, when accounting for inhomogeneities in media, the domain has to be divided into a large number of homogeneous zones. This approach poses the problem of increased computational cost in determining the eigenfrequencies, since convergence to the higher order unstable modes becomes particularly difficult as the number of zones increases [1, 23]. In this study, an approximate analytical solution based on the Wentzel-Kramers-Brillouin (WKB) method is developed for the acoustic wave equation in a quasi one-dimensional (1-D) domain with non-uniform cross-sectional area and flow properties. Numerical

solutions to the wave equation were also obtained. Both the current and classical WKB solutions are compared with the corresponding numerical solutions, as well as the exact solutions where available. The WKB method is then applied to determine the instabilities in a dump combustor with a sudden change in cross-section.

During the past six decades or so, numerous approximate solution methods, based on ray or geometrical acoustics considerations, have been developed for the linear wave equation in inhomogeneous media [61–68]. In ray acoustics, the acoustic perturbation is described using an amplitude and a harmonic-like functionality called the eikonal, which are both functions of space. Substitution of this perturbation form into the wave equation yields coupled, non-linear ordinary differential equations (ODEs) for the amplitude and phase (in the eikonal). In general, it is not possible to get exact, closed form solutions to these ODEs, so that they will have to be solved numerically. However, under certain conditions, approximate analytical solutions can be obtained for 1-D geometries. One such approach is called the Wentzel-Kramers-Brillouin (WKB) method [69–73]. The WKB method utilizes the high frequency approximation, i.e. the acoustic wavelength is small compared to the characteristic scale of the inhomogeneity. This approximation allows us to neglect certain terms in the ODEs and thereby develop closed form solutions for the amplitude and phase.

Cummings [74] developed a variant of the high-frequency WKB solution for rigid-walled ducts with axial mean temperature gradients. The modified method differs from the conventional WKB method in the approximations made to obtain analytical solutions to the governing equations. The solutions obtained using this

method showed marginally improved agreement with experimental data and numerical solutions than did the classical WKB solutions.

Approximate solutions that are *not* based on the ray acoustics approximation have also been developed [75–78]. Peat [77] presented an approximate analytical solution for the acoustic perturbations inside a capillary duct with uniform flow and axial temperature gradients. This method utilizes a perturbation series expansion of the acoustic fluctuations with a dimensionless mean temperature gradient as the small parameter, along with an assumed quadratic spatial dependence for the acoustic pressure and velocity fluctuations. It was found that both the amplitude and phase-speed varied significantly with the mean temperature gradient. However, they were found not to change appreciably along the duct length, due to the low-order spatial approximation used. Peat also noted that the isentropic assumption used in deriving the approximate solution broke down as the mean Mach number or temperature gradient increased, necessitating numerical solution.

Munjal and Prasad [78] also developed a non-WKB approximate solution to the 1-D wave equation in a uniform cross-sectional area duct with gradients in both mean flow and temperature. They used perturbation theory in conjunction with the Green's function method to derive the solution. Peat [75] developed an alternative approximate solution to the problem considered by Munjal and Prasad [78], wherein the phase was assumed to be spatially invariant, but not the amplitude.

Exact solutions were also developed for the wave equation in inhomogeneous media [3, 79–81]. Sujith et al. [3] derived an exact solution, involving Bessel functions, to the 1-D cartesian wave equation with mean temperature gradients and no

mean flow. They suggested that this solution was also applicable at low mean Mach numbers $\overline{M}$ such that $\overline{M}^2 \ll 1$. Subsequently, Karthik, Kumar and Sujith [79] extended this technique to include mean temperature and velocity gradients. Under the assumptions of low Mach number and linear mean temperature profile, they transformed the spatial Helmholtz equation to the temperature space, and obtained exact solutions in the form of a hypergeometric series. Bala Subrahmanyam, Sujith and Lieuwen [80] derived exact solutions to the wave equation in a quasi 1-D cartesian duct with mean temperature gradients and a varying cross-sectional area. They presented the cross-sectional area and mean velocity profiles for which closed form solutions are possible. In a subsequent study, they also derived [81] solutions to the wave equation in cylindrical and spherical geometries with mean temperature gradients. These solutions had a $\overline{T}^{-1/4}$ dependence on the mean temperature, as is also the case with the WKB solutions to these problems.

Modal analysis-based solutions to the wave equation are commonly applied to predict combustion instabilities. However, modal analysis suffers from certain limitations, which have already been discussed. To our knowledge, approximate solution methods, such as the WKB method, have not yet been applied to predict combustion instabilities in ducts with inhomogeneities. This study aims to fill this gap by developing a WKB-type solution for a duct with varying cross-sectional area and mean flow properties, and applying it to predict the longitudinal instabilities in a dump combustor. The current WKB solution is compared with the classical WKB solution, as well as numerical results. The resonant frequencies predicted by the current WKB solution for a duct with a linearly varying mean temperature are shown to be in

good agreement with those obtained from the exact solution of Sujith [3]. The WKB solution is then employed to predict the unstable frequencies of a dump combustor with a single discontinuity in area. The instability predictions are validated against the experimental and analytical results of Yu et al. [2].

The organization of this paper is as follows. In Section 4.3, we derive the current and classical WKB solutions to three problems involving variations in mean temperature and cross-sectional area, both with and without mean flow. We then compare in Section 4.4 the two WKB solutions with the numerical and exact solutions to the corresponding wave equations. The resonant frequences of a duct with linearly varying temperature were also obtained and compared with those obtained from the exact solution to the wave equation. In Section 4.5, the predictions of combustion instability frequencies using the WKB solution are presented. Finally, in Appendix D, we compare the eigenfrequences obtained using the modal analysis and WKB methods for a duct with mean temperature gradient.

4.3 WKB-Type Solution

We begin by deriving the linear wave equation in a quasi 1-D cartesian duct with varying cross-sectional area, shown in Figure 4.1. For this geometry, the continuity equation is [80]

$$S\frac{\partial \rho}{\partial t} + \frac{\partial}{\partial x}(\rho u S) = 0 \tag{4.1}$$

where S is the cross-sectional area, ρ is the fluid density and u is the axial flow velocity. We decompose the flow variables into mean and fluctuating quantities (e.g.,
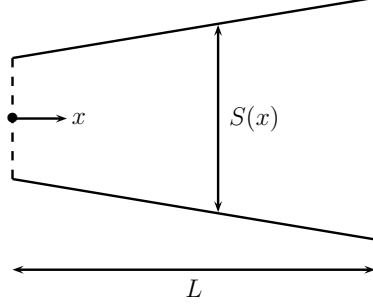
Figure 4.1: Geometry of quasi 1-D duct with changing cross-sectional area. $S(x)$ is the axially varying area.

$\rho = \overline{\rho} + \rho'$), and linearize Eq. (4.1) yielding the mean and fluctuating forms of the continuity equation.

$$S \left(\overline{u} \frac{\mathrm{d}\overline{\rho}}{\mathrm{d}x} + \overline{\rho} \frac{\mathrm{d}\overline{u}}{\mathrm{d}x} \right) + \overline{\rho} \, \overline{u} \frac{\mathrm{d}S}{\mathrm{d}x} = 0 \tag{4.2}$$

$$S \frac{\partial \rho'}{\partial t} + S \overline{u} \frac{\partial \rho'}{\partial x} + S \frac{\partial \overline{\rho}}{\partial x} u' + S \overline{\rho} \frac{\partial u'}{\partial x} + S \frac{\partial \overline{u}}{\partial x} \rho' + \overline{\rho} \frac{\partial S}{\partial x} u' + \overline{u} \frac{\partial S}{\partial x} \rho' = 0 \tag{4.3}$$

The inviscid momentum balance equation is

$$\rho \left(\frac{\partial u}{\partial t} + u \frac{\partial u}{\partial x} \right) = -\frac{\partial p}{\partial x} \tag{4.4}$$

where p is the fluid pressure. The mean and the (linearized) fluctuating forms of the momentum equation are

$$\overline{\rho u} \frac{\mathrm{d}\overline{u}}{\mathrm{d}x} = -\frac{\mathrm{d}\overline{p}}{\mathrm{d}x} \tag{4.5}$$

$$\overline{u} \frac{\partial \overline{u}}{\partial x} \rho' + \overline{\rho} \frac{\partial u'}{\partial t} + \overline{\rho} \, \overline{u} \frac{\partial u'}{\partial x} + \overline{\rho} \frac{\partial \overline{u}}{\partial x} u' = -\frac{\partial p'}{\partial x} \tag{4.6}$$

The energy balance equation with the viscous dissipation terms dropped is [77,78,80]

$$S\frac{\partial p}{\partial t} + Su\frac{\partial p}{\partial x} + \gamma p\frac{\partial(Su)}{\partial x} = 0 \tag{4.7}$$

where γ is the ratio of specific heats. The mean and the fluctuating forms of the energy equation are

$$S\overline{u}\frac{\mathrm{d}\overline{p}}{\mathrm{d}x} + S\gamma\overline{p}\frac{\mathrm{d}\overline{u}}{\mathrm{d}x} + \gamma\overline{p}\,\overline{u}\frac{\mathrm{d}S}{\mathrm{d}x} = 0 \tag{4.8}$$

$$S\frac{\partial p'}{\partial t} + S\overline{u}\frac{\partial p'}{\partial x} + S\frac{\partial\overline{p}}{\partial x}u' + S\gamma\overline{p}\frac{\partial u'}{\partial x} + S\gamma\frac{\partial\overline{u}}{\partial x}p' + \gamma\overline{p}\frac{\partial S}{\partial x}u' + \gamma\overline{u}\frac{\partial S}{\partial x}p' = 0 \tag{4.9}$$

Combining Eqs. (4.9) and (4.6), and using $\rho' = p'/\overline{c}^2$, we arrive at the wave equation:

$$
\begin{aligned}
\frac{1}{\overline{c}^2}\frac{\partial^2 p'}{\partial t^2} - \frac{\partial^2 p'}{\partial x^2} ={}& \left(\frac{\partial\overline{u}}{\partial x}\right)^2\frac{p'}{\overline{c}^2} + \frac{\overline{u}}{\overline{c}^2}\frac{\partial^2\overline{u}}{\partial x^2}p' + \frac{\overline{u}}{\overline{c}^2}\frac{\partial\overline{u}}{\partial x}\frac{\partial p'}{\partial x} - 2\frac{\overline{u}}{\overline{c}^3}\frac{\partial\overline{u}}{\partial x}\frac{\partial\overline{c}}{\partial x}p' \\
&- \frac{1}{\overline{\rho}}\frac{\partial\overline{\rho}}{\partial x}\frac{\partial p'}{\partial x} - \frac{\overline{u}}{\overline{\rho}\,\overline{c}^2}\frac{\partial\overline{\rho}}{\partial x}\frac{\partial\overline{u}}{\partial x}p' - \frac{\overline{u}}{\overline{c}^2}\frac{\partial^2 p'}{\partial x\partial t} - \frac{\gamma}{\overline{c}^2}\frac{\partial\overline{u}}{\partial x}\frac{\partial p'}{\partial t} - \frac{\overline{\gamma}}{S}\frac{\overline{u}}{\overline{c}^2}\frac{\partial S}{\partial x}\frac{\partial p'}{\partial t} \\
&- \frac{\overline{\rho}}{S}\frac{\partial S}{\partial x}\frac{\partial u'}{\partial t} - \frac{1}{\overline{c}^2}\frac{\partial\overline{p}}{\partial x}\frac{\partial u'}{\partial t} + 2\overline{\rho}\frac{\partial\overline{u}}{\partial x}\frac{\partial u'}{\partial x} + \overline{\rho}\frac{\partial^2\overline{u}}{\partial x^2}u' + \overline{\rho u}\frac{\partial^2 u'}{\partial x^2}
\end{aligned}
\tag{4.10}
$$

Substituting $p' = \hat{p}(x)e^{i\Omega t}$ and $u' = \hat{u}(x)e^{i\Omega t}$ into Eq. (4.10), we have

$$
\begin{aligned}
-\frac{\Omega^2}{\overline{c}^2}\hat{p} - \frac{\partial^2\hat{p}}{\partial x^2} ={}& \left(\frac{\partial\overline{u}}{\partial x}\right)^2\frac{\hat{p}}{\overline{c}^2} + \frac{\overline{u}}{\overline{c}^2}\frac{\partial^2\overline{u}}{\partial x^2}\hat{p} + \frac{\overline{u}}{\overline{c}^2}\frac{\partial\overline{u}}{\partial x}\frac{\partial\hat{p}}{\partial x} - 2\frac{\overline{u}}{\overline{c}^3}\frac{\partial\overline{u}}{\partial x}\frac{\partial\overline{c}}{\partial x}\hat{p} \\
&- \frac{1}{\overline{\rho}}\frac{\partial\overline{\rho}}{\partial x}\frac{\partial\hat{p}}{\partial x} - \frac{\overline{u}}{\overline{\rho}\,\overline{c}^2}\frac{\partial\overline{\rho}}{\partial x}\frac{\partial\overline{u}}{\partial x}\hat{p} - \frac{i\Omega\overline{u}}{\overline{c}^2}\frac{\partial^2\hat{p}}{\partial x} - \frac{i\Omega\gamma}{\overline{c}^2}\frac{\partial\overline{u}}{\partial x}\hat{p} - \frac{i\Omega\overline{\gamma}}{S}\frac{\overline{u}}{\overline{c}^2}\frac{\partial S}{\partial x}\hat{p} \\
&- i\Omega\frac{\overline{\rho}}{S}\frac{\partial S}{\partial x}\hat{u} - i\Omega\frac{1}{\overline{c}^2}\frac{\partial\overline{p}}{\partial x}\hat{u} + \overline{\rho u}\frac{\partial^2\hat{u}}{\partial x^2} + 2\overline{\rho}\frac{\partial\overline{u}}{\partial x}\frac{\partial\hat{u}}{\partial x} + \overline{\rho}\frac{\partial^2\overline{u}}{\partial x^2}\hat{u}
\end{aligned}
\tag{4.11}
$$

In the following discussion, we present WKB-type solutions to the wave equation for cases involving linearly varying cross-sectional area and temperature. Both zero and uniform mean velocities are considered.

124

4.3.1 Case 1: $\overline{u} = 0$, $\frac{dS}{dx} = 0$ and $\overline{T} = mx + T_1$

In this case, we consider a duct with uniform cross-section, no mean flow, and a linear mean temperature. For this case, Eq. (4.5), in conjunction with the ideal gas law, becomes

$$\frac{1}{\overline{\rho}}\frac{d\overline{\rho}}{dx} + \frac{1}{\overline{T}}\frac{d\overline{T}}{dx} = 0 \tag{4.12}$$

Using Eq. (4.12) in Eq. (4.11) we get [3]

$$\frac{d^2\hat{p}}{dx^2} + \frac{1}{\overline{T}}\frac{d\overline{T}}{dx}\frac{d\hat{p}}{dx} + \frac{\Omega^2}{\gamma R\overline{T}}\hat{p} = 0 \tag{4.13}$$

where $\overline{c}^2 = \gamma R\overline{T}$ (R is the the specific gas constant). Sujith et al. [3] derived an exact solution to Eq. (4.13) involving Bessel functions. Our interest, however, is to obtain a WKB-type solution to Eq. (4.13). Therefore, we consider a solution of the form:

$$\hat{p}(x) = A(x)e^{i\theta(x)} \tag{4.14}$$

where $A(x)$ and $\theta(x)$ are the amplitude and phase of the pressure wave, respectively. Substituting Eq.(4.14) in Eq.(4.13), and equating the real and imaginary parts, we get two coupled non-linear ODEs given by

$$\frac{d^2A}{dx^2} - A\left(\frac{d\theta}{dx}\right)^2 + \frac{1}{\overline{T}}\frac{d\overline{T}}{dx}\frac{dA}{dx} + \frac{\Omega^2}{\gamma R\overline{T}}A = 0 \tag{4.15}$$

$$2\frac{dA}{dx}\frac{d\theta}{dx} + A\frac{d^2\theta}{dx^2} + \frac{1}{\overline{T}}\frac{d\overline{T}}{dx}A\frac{d\theta}{dx} = 0 \tag{4.16}$$

125

There is no closed form solution to these non-linear ODEs. However, by making certain approximations, we can obtain an analytical solution.

The standard WKB method is based on two principal approximations. The first is the high-frequency approximation, which enables us to neglect $\frac{\mathrm{d}^2 A}{\mathrm{d}x^2}$ as compared to $\frac{\Omega^2}{\gamma R \overline{T}} A$. Second, it is assumed that the mean temperature is large and that it changes slowly in x, allowing us to drop the $\frac{1}{\overline{T}} \frac{\mathrm{d}\overline{T}}{\mathrm{d}x} \frac{\mathrm{d}A}{\mathrm{d}x}$ term as well. In this study, we also derive a modified WKB-type solution by dropping the second assumption. We now present for Case 1 both the standard WKB solution and the current WKB-type solution.

4.3.1.1 Standard WKB Solution

Dropping both $\frac{\mathrm{d}^2 A}{\mathrm{d}x^2}$ and $\frac{1}{\overline{T}} \frac{\mathrm{d}\overline{T}}{\mathrm{d}x} \frac{\mathrm{d}A}{\mathrm{d}x}$ terms in Eq. (4.15), and solving for the phase for a linear mean temperature ($\overline{T} = mx + T_1$), we get

$$\theta(x) = \pm \frac{2\Omega}{\gamma R m} \overline{c}(x) + \mathscr{C}_\theta \tag{4.17}$$

where $\mathscr{C}_\theta$ is a constant of integration and depends on the boundary condition for the phase, and the negative and positive phases correspond to the forward and backward traveling waves, respectively.

From Eq. (4.16), we now have

$$\frac{\mathrm{d}A}{\mathrm{d}x} + A \underbrace{\left(\frac{\frac{1}{\overline{T}} \frac{\mathrm{d}\overline{T}}{\mathrm{d}x} \frac{\mathrm{d}\theta}{\mathrm{d}x} + \frac{\mathrm{d}^2\theta}{\mathrm{d}x^2}}{2 \frac{\mathrm{d}\theta}{\mathrm{d}x}} \right)}_{\psi_1(x)} = 0 \tag{4.18}$$

126

Equation (4.18) gives us two amplitudes for the forward and backward traveling waves. Their general form is given by

$$A(x) = \mathscr{C}_A e^{-\int \psi_1(x) \; \mathrm{d}x} \tag{4.19}$$

where $\mathscr{C}_A$ is the constant of integration obtained from the boundary condition on the amplitude of the wave.

4.3.1.2 Modified WKB Solution

In the current approach, we only neglect the $\frac{\mathrm{d}^2 A}{\mathrm{d}x^2}$ term in Eq. (4.15), giving us

$$\frac{1}{A}\frac{\mathrm{d}A}{\mathrm{d}x} = \frac{\left(\frac{\mathrm{d}\theta}{\mathrm{d}x}\right)^2 - \frac{\Omega^2}{\gamma R \overline{T}}}{\frac{1}{\overline{T}}\frac{\mathrm{d}\overline{T}}{\mathrm{d}x}} \tag{4.20}$$

Equation (4.16) can now be written as

$$\frac{\mathrm{d}\theta}{\mathrm{d}x}\left(\frac{2}{A}\frac{\mathrm{d}A}{\mathrm{d}x} + \frac{1}{\overline{T}}\frac{\mathrm{d}\overline{T}}{\mathrm{d}x}\right) + \frac{\mathrm{d}^2\theta}{\mathrm{d}x^2} = 0 \tag{4.21}$$

Substituting Eq. (4.20) in Eq. (4.21), we get

$$\frac{\mathrm{d}^2\theta}{\mathrm{d}x^2} + \frac{2}{\frac{1}{\overline{T}}\frac{\mathrm{d}\overline{T}}{\mathrm{d}x}}\left(\frac{\mathrm{d}\theta}{\mathrm{d}x}\right)^3 - \left(\frac{2\Omega^2}{\gamma R \frac{\mathrm{d}\overline{T}}{\mathrm{d}x}} - \frac{1}{\overline{T}}\frac{\mathrm{d}\overline{T}}{\mathrm{d}x}\right)\frac{\mathrm{d}\theta}{\mathrm{d}x} = 0 \tag{4.22}$$

Upon substituting $y = \frac{\mathrm{d}\theta}{\mathrm{d}x}$ into Eq. (4.22),

$$\frac{\mathrm{d}y}{\mathrm{d}x} + \frac{2}{\frac{1}{\overline{T}}\frac{\mathrm{d}\overline{T}}{\mathrm{d}x}}y^3 - \left(\frac{2\Omega^2}{\gamma R \frac{\mathrm{d}\overline{T}}{\mathrm{d}x}} - \frac{1}{\overline{T}}\frac{\mathrm{d}\overline{T}}{\mathrm{d}x}\right)y = 0 \tag{4.23}$$

which is non-linear in y, but can still be solved analytically (giving rise to a rather involved expression for y). However, this solution for y cannot be further integrated analytically to yield θ. Hence, we performed the integration numerically. Having obtained θ, we can solve Eq. (4.20), which is a first order linear ODE in the amplitude A.

4.3.2 Case 2: $\bar{u} = 0$, $\overline{S} = S_1 x + S_2$ and $\overline{T} = mx + T_1$

Here we consider a duct with no mean flow, and with linearly varying cross-sectional area and mean temperature. For this case, Eq. (4.11) reduces to

$$\frac{\mathrm{d}^2 \hat{p}}{\mathrm{d}x^2} + \left(\frac{1}{\overline{T}} \frac{\mathrm{d}\overline{T}}{\mathrm{d}x} + \frac{1}{S} \frac{\mathrm{d}S}{\mathrm{d}x} \right) \frac{\mathrm{d}\hat{p}}{\mathrm{d}x} + \frac{\Omega^2}{\gamma R \overline{T}} \hat{p} = 0 \tag{4.24}$$

Substituting $\hat{p}(x) = A(x) e^{i\theta(x)}$ in Eq. (4.24), we get the following coupled non-linear ODEs.

$$\frac{\mathrm{d}^2 A}{\mathrm{d}x^2} - A \left(\frac{\mathrm{d}\theta}{\mathrm{d}x} \right)^2 + \left(\frac{1}{\overline{T}} \frac{\mathrm{d}\overline{T}}{\mathrm{d}x} + \frac{1}{S} \frac{\mathrm{d}S}{\mathrm{d}x} \right) \frac{\mathrm{d}A}{\mathrm{d}x} + \frac{\Omega^2}{\gamma R \overline{T}} A = 0 \tag{4.25}$$

$$2 \frac{\mathrm{d}A}{\mathrm{d}x} \frac{\mathrm{d}\theta}{\mathrm{d}x} + A \frac{\mathrm{d}^2\theta}{\mathrm{d}x^2} + \left(\frac{1}{\overline{T}} \frac{\mathrm{d}\overline{T}}{\mathrm{d}x} + \frac{1}{S} \frac{\mathrm{d}S}{\mathrm{d}x} \right) A \frac{\mathrm{d}\theta}{\mathrm{d}x} = 0 \tag{4.26}$$

4.3.2.1 Standard WKB Solution

Neglecting both $\frac{\mathrm{d}^2 A}{\mathrm{d}x^2}$ and $\left(\frac{1}{\overline{T}} \frac{\mathrm{d}\overline{T}}{\mathrm{d}x} + \frac{1}{S} \frac{\mathrm{d}S}{\mathrm{d}x} \right) \frac{\mathrm{d}A}{\mathrm{d}x}$ terms in Eq. (4.25), the phase of the wave is given by

$$\theta(x) = \pm \frac{2\Omega}{\gamma R m} \bar{c}(x) + \mathscr{C}_\theta \tag{4.27}$$

Note that the phase is the same as that in Eq. (4.17) for Case 1, meaning that the duct cross-section does not the affect the phase.

The amplitude can now be obtained from Eq. (4.26)

$$\frac{\mathrm{d}A}{\mathrm{d}x} + A \underbrace{\left\{ \frac{\left(\frac{1}{\overline{T}}\frac{\mathrm{d}\overline{T}}{\mathrm{d}x} + \frac{1}{S}\frac{\mathrm{d}S}{\mathrm{d}x}\right)\frac{\mathrm{d}\theta}{\mathrm{d}x} + \frac{\mathrm{d}^2\theta}{\mathrm{d}x^2}}{2\frac{\mathrm{d}\theta}{\mathrm{d}x}} \right\}}_{\psi_2(x)} = 0 \qquad (4.28)$$

which yields

$$A(x) = \mathscr{C}_A e^{-\int \psi_2(x)\ \mathrm{d}x} \qquad (4.29)$$

In contrast to the phase, the wave amplitude is a function of duct geometry.

4.3.2.2   Modified WKB Solution

Neglecting the $\frac{\mathrm{d}^2 A}{\mathrm{d}x^2}$ term, Eq. (4.25) can be written as

$$\frac{1}{A}\frac{\mathrm{d}A}{\mathrm{d}x} = \frac{\left(\frac{\mathrm{d}\theta}{\mathrm{d}x}\right)^2 - \frac{\Omega^2}{\gamma R \overline{T}}}{\frac{1}{\overline{T}}\frac{\mathrm{d}\overline{T}}{\mathrm{d}x} + \frac{1}{S}\frac{\mathrm{d}S}{\mathrm{d}x}} \qquad (4.30)$$

The phase equation then becomes

$$\frac{\mathrm{d}^2\theta}{\mathrm{d}x^2} + \frac{2}{\frac{1}{\overline{T}}\frac{\mathrm{d}\overline{T}}{\mathrm{d}x} + \frac{1}{S}\frac{\mathrm{d}S}{\mathrm{d}x}}\left(\frac{\mathrm{d}\theta}{\mathrm{d}x}\right)^3 - \left\{\frac{2\Omega^2}{\gamma R \overline{T}\left(\frac{1}{\overline{T}}\frac{\mathrm{d}\overline{T}}{\mathrm{d}x} + \frac{1}{S}\frac{\mathrm{d}S}{\mathrm{d}x}\right)} - \frac{1}{\overline{T}}\frac{\mathrm{d}\overline{T}}{\mathrm{d}x} - \frac{1}{S}\frac{\mathrm{d}S}{\mathrm{d}x}\right\}\frac{\mathrm{d}\theta}{\mathrm{d}x} = 0 \quad (4.31)$$

Equation (4.31) is solved numerically for the phase, following which the amplitude is obtained from Eq. (4.30).

4.3.3 Case 3: $\frac{\mathrm{d}\overline{u}}{\mathrm{d}x} = 0$, $\frac{\mathrm{d}S}{\mathrm{d}x} = 0$ and $\overline{T} = mx + T_1$

Here we consider a duct with uniform cross-sectional area and mean flow, and a linearly varying mean temperature. We begin with the $\hat{p}(x)$ equation obtained from the classical convected wave equation [23, 75, 78]

$$\frac{\mathrm{d}^2\hat{p}}{\mathrm{d}x^2} + \frac{2i\Omega\overline{M}}{\overline{c}(\overline{M}^2 - 1)}\frac{\mathrm{d}\hat{p}}{\mathrm{d}x} - \frac{\Omega^2}{\overline{c}^2(\overline{M}^2 - 1)}\hat{p} = 0 \tag{4.32}$$

where $\overline{M} = \overline{u}/\overline{c}(x)$. Substituting $\hat{p}(x) = A(x)e^{i\theta(x)}$ into Eq. (4.32), we get

$$\frac{\mathrm{d}^2 A}{\mathrm{d}x^2} - A\left(\frac{\mathrm{d}\theta}{\mathrm{d}x}\right)^2 + \frac{2\Omega\overline{M}}{\overline{c}(\overline{M}^2 - 1)}A\frac{\mathrm{d}\theta}{\mathrm{d}x} - \frac{\Omega^2}{\overline{c}^2(\overline{M}^2 - 1)}A = 0 \tag{4.33}$$

$$2\frac{\mathrm{d}A}{\mathrm{d}x}\frac{\mathrm{d}\theta}{\mathrm{d}x} + A\frac{\mathrm{d}^2\theta}{\mathrm{d}x^2} + \frac{2\Omega\overline{M}}{\overline{c}(\overline{M}^2 - 1)}\frac{\mathrm{d}A}{\mathrm{d}x} = 0 \tag{4.34}$$

It is to be noted here that for Case 3, unlike Cases 1 and 2, the standard and the current WKB solutions coincide because of the absence of the $\frac{1}{\overline{T}}\frac{\mathrm{d}\overline{T}}{\mathrm{d}x}\frac{\mathrm{d}A}{\mathrm{d}x}$ term in Eq. (4.33).

Neglecting $\frac{\mathrm{d}^2 A}{\mathrm{d}x^2}$, we solve Eq. (4.33) for the phase

$$\theta(x) = \pm 2\frac{\overline{c}\Omega + \overline{u}\Omega\log\left[\Omega(\overline{c} - \overline{u})\right]}{\gamma m R} + \mathscr{C}_\theta \tag{4.35}$$

Equation (4.34) may now be solved for the the amplitude.

$$A(x) = \mathscr{C}_A\exp\left\{-\int\left[\frac{\frac{\mathrm{d}^2\theta}{\mathrm{d}x^2}}{2\frac{\mathrm{d}\theta}{\mathrm{d}x} + \frac{2\Omega\overline{M}}{\overline{c}(\overline{M}^2-1)}}\right]\mathrm{d}x\right\} \tag{4.36}$$

The amplitudes for the forward and backward travelling waves are obtained using the negative and positive values of θ in Eq. (4.35), respectively.

4.4   WKB Results

In this section, we compare the waveforms predicted by the standard and modified WKB solutions with the numerical solution to the governing equation for $\hat{p}$. At any location x in the domain, the spatial pressure wave $\hat{p}(x)$, comprising both the forward and backward traveling waves, is given by

$$\hat{p}(x) = \mathscr{C}^+ A^+ e^{i\theta^+} + \mathscr{C}^- A^- e^{i\theta^-} \tag{4.37}$$

where the superscripts $(\cdot)^+$ and $(\cdot)^-$ refer to the forward and backward traveling waves, respectively, and $\mathscr{C}^+$ and $\mathscr{C}^-$ are the unknown coefficients which may be determined by applying boundary conditions on $\hat{p}(x)$. Notice that the constants of integration $\mathscr{C}_\theta$ and $\mathscr{C}_A$ (e.g., in Eqs. (4.17) and (4.19)) are subsumed into $\mathscr{C}^+$ and $\mathscr{C}^-$; this step enables us to avoid the specification of boundary conditions for the amplitude $A(x)$ and phase $\theta(x)$. The coefficients $\mathscr{C}^+$ and $\mathscr{C}^-$ for both WKB solutions are then obtained using the boundary conditions (adopted from Sujith et al. [3]): $\hat{p}(x = 0) = 1$ at the inlet and $\frac{\mathrm{d}\hat{p}}{\mathrm{d}x}\big|_{x=L} = 0$ at the outlet of the duct. These boundary conditions were also used when numerically solving the $\hat{p}$ equation for each of the cases (Eqs. (4.13), (4.24), (4.32)). All numerical solutions were obtained via the technical computing platform Mathematica®.

4.4.1   Case 1: $\bar{u} = 0$, $\frac{\mathrm{d}S}{\mathrm{d}x} = 0$ and $\overline{T} = mx + T_1$

In this case, we present the (standard and modified) WKB waveforms, as well as the numerical solution to Eq. (4.13). The geometry under consideration is that of a uniform cross-section duct with no mean flow, but with a linearly varying mean temperature given by $\overline{T}(x) = 500 + 125x$. The temperatures at the two ends of the duct are 500 K and 1000 K, with the length and height of the duct being 4m and 0.2m, respectively.

In Figure 4.2, we compare $\hat{p}(x)$ from the standard and modified WKB approaches with the numerical solution at the frequencies of 100, 500 and 1000 radians/s. We also considered the exact solution of Sujith et al. [3], and found that their solution was essentially identical to the current numerical solution. Hence, it is not shown explicitly in Figure 4.2. At all three frequencies, the modified WKB solution is significantly closer to the numerical solution than the standard WKB solution. The differences between the two WKB solutions may be attributed to the neglect in the standard method of the term $\frac{1}{\overline{T}}\frac{\mathrm{d}\overline{T}}{\mathrm{d}x}\frac{\mathrm{d}A}{\mathrm{d}x}$ in Eq. (4.15). Since the temperature gradient considered is relatively large ($\frac{d\overline{T}}{dx} = 125$), the neglect of this term introduces errors into the standard WKB method. To illustrate this further, in Figure 4.3, we will consider the case of a smaller temperature gradient ($\frac{d\overline{T}}{dx} = 25$).

In Figure 4.3, $\hat{p}(x)$ is shown for a temperature profile given by $\overline{T}(x) = 500 + 25x$ (i.e., $\frac{d\overline{T}}{dx} = 25$). It is evident in Figure 4.3 that, at all frequencies, the standard and the modified WKB solutions are both in excellent agreement with the numerical solution. Therefore, it may be said that the standard WKB method is most accurate for slowly

varying mean temperature. As in Figure 4.2, the exact and numerical solutions are indistinguishable.

Figure 4.2: Spatial pressure wave $\hat{p}(x)$ is plotted along the length of the duct for angular frequencies of 100 (red), 500 (blue) and 1000 (black) radians/s. Modified WKB solution: solid line (———); Standard WKB solution: dotted line ($\cdots\cdots$); Numerical solution: dashed line (– – – –).

4.4.2 Case 2A: $\bar{u} = 0$, $S = S_1 x + S_2$, and $\frac{d\overline{T}}{dx} = 0$

We now consider the effects of variation in cross-sectional area at various (constant) mean temperatures and no mean flow.

Figure 4.3: Spatial pressure wave $\hat{p}(x)$ is plotted along the length of the duct for angular frequencies of 100 (red), 500 (blue) and 1000 (black) radians/s. Modified WKB solution: solid line (——); Standard WKB solution: dotted line ($\cdots\cdots$); Numerical solution: dashed line (– – – –).

4.4.2.1 $S(x) = 0.2 + x/20$ and $\overline{T} = 500$ K

The duct considered has an inlet cross-sectional area $S_1 = 0.2$ m² and an outlet area $S_1 = 0.4$ m², with a constant mean temperature $\overline{T} = 500$ K. The cross-sectional area gradient $\frac{dS}{dx} = \frac{1}{20}$. In Figure 4.4, we compare $\hat{p}(x)$ obtained from the modified and standard WKB approaches with the numerical solution at the frequencies 100, 500 and 1000 radians/s. At $\Omega = 100$, both the standard and modified WKB solutions are

in good agreement with the numerical solution. However, for $\Omega = 500$, the agreement of the WKB solutions with the numerical solution deteriorates, although the standard solution is marginally closer to the numerical solution. For $\Omega = 1000$, we again see excellent agreement among the three solutions. The seemingly anamolous behavior at $\Omega = 500$ may be because this frequency is close to the resonant frequency of the duct. The proximity of Ω to the resonant frequency may be deduced from the higher amplitudes at this frequency. It may be noted that at the resonant frequencies, the wave equation has singular solutions.

4.4.2.2 $S(x) = 0.2 + 3x/20$ and $\overline{T} = 500$ K

In Figure 4.5, $\hat{p}(x)$ from the three solutions is plotted as a function of x for a duct with cross-sectional area profile of $S(x) = 0.2 + 3x/20$. Here, the cross-sectional area gradient $\frac{\mathrm{d}S}{\mathrm{d}x}$ is three times that of the previous case. The length of the duct is 4 m and $\overline{T} = 500$ K. For $\Omega = 100$ radians/s, the modified WKB method does perform better than the standard WKB method. For $\Omega = 500$, we see that the two WKB solutions differ substantially from the numerical solution. This may be because the $\Omega = 500$ frequency is close to the resonant frequency of the duct. However at $\Omega = 1000$, both WKB solutions are in excellent agreement with the numerical solution.

4.4.2.3 $S(x) = 0.2 + x/20$ and $\overline{T} = 1000$ K

We consider the same duct as in Section 4.4.2.1, but with a higher mean temperature of 1000 K. We can see from Figure 4.6 that, as the frequency increases
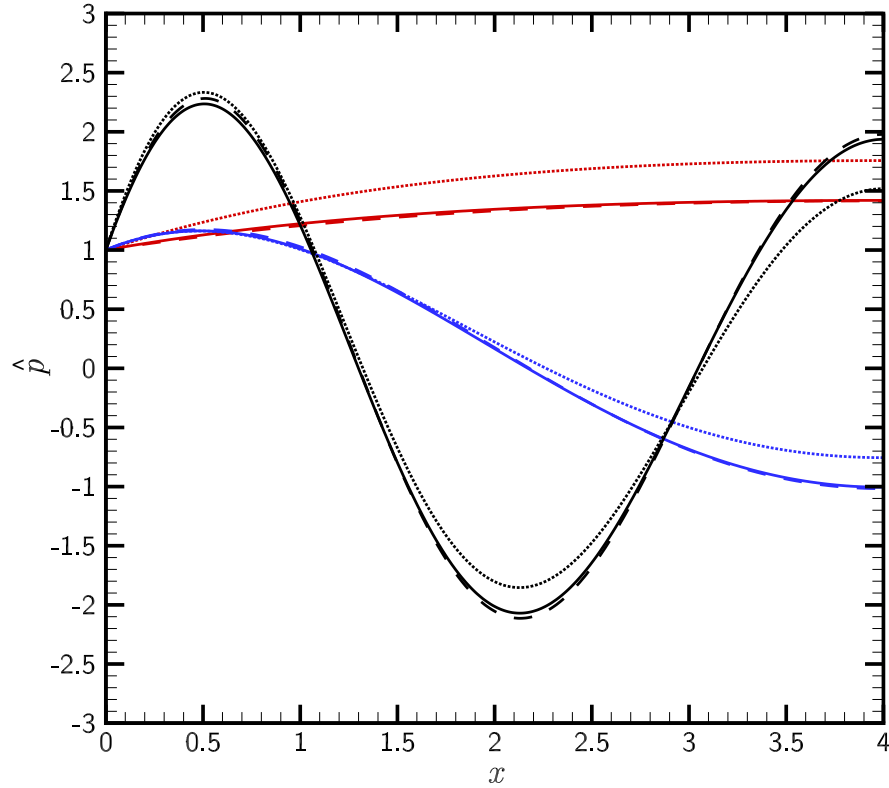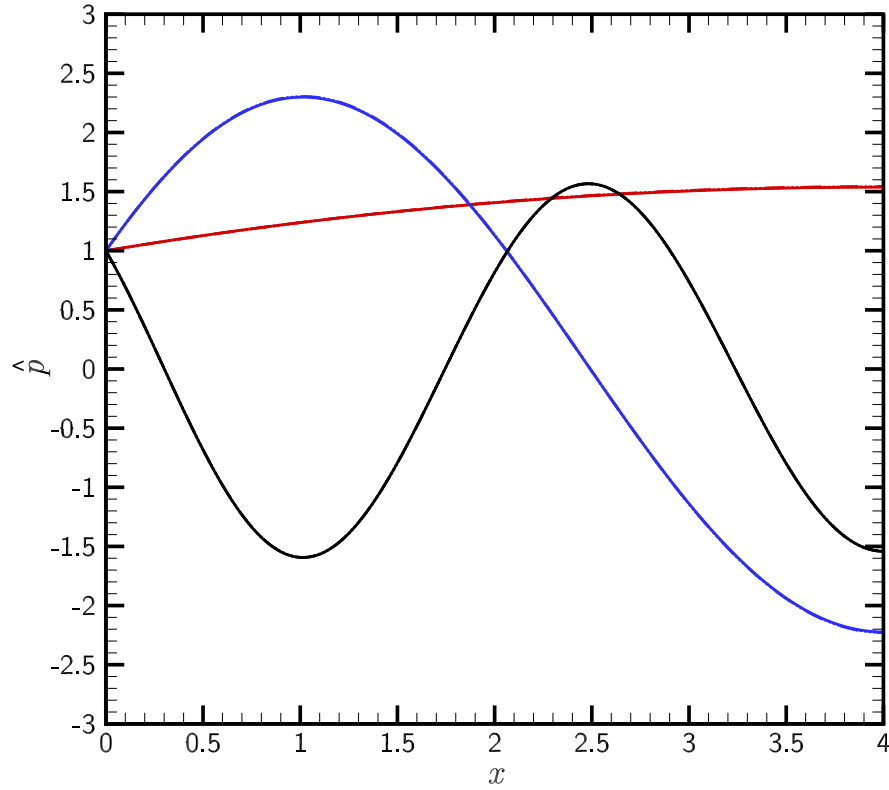
Figure 4.4: Spatial pressure wave $\hat{p}(x)$ is plotted along the length of the duct for angular frequencies of 100 (red), 500 (blue) and 1000 (black) radians/s. $S_1 = 0.2$m, $S_2 = 0.4$m and $\overline{T} = 500$ K. Modified WKB solution: solid line (——); Standard WKB solution: dotted line ($\cdots\cdots$); Numerical solution: dashed line (- - - -).

both the classical and modified WKB solutions approach the numerical solution. Interestingly, the high amplitude observed in the previous two cases at $\Omega = 500$ is not seen here, suggesting that the resonant frequency of the duct has changed due to the higher mean temperature.

Figure 4.5: Spatial pressure wave $\hat{p}(x)$ is plotted along the length of the duct for angular frequencies of 100 (red), 500 (blue) and 1000 (black) radians/s. $S_1 = 0.2$m, $S_2 = 0.8$m and $\overline{T} = 500$ K. Modified WKB solution: solid line (———); Standard WKB solution: dotted line ($\cdots\cdots$); Numerical solution: dashed line (- - - -).

4.4.3   Case 2B: $\overline{u} = 0$, $S = S_1 x + S_2$ and $\overline{T} = mx + T_1$

We consider a duct with no mean flow, and with linearly varying cross-sectional area and mean temperature. The duct area profile is given by $S(x) = 0.2 + x/20$ (same as that in Case 2A), the mean temperature $\overline{T}(x) = 500 + 125x$, and the duct length is 4m. For this case, we only present the standard WKB solution. This is because we could not compute a converged numerical solution to Eq. (4.31) for the modified

Figure 4.6: Spatial pressure wave $\hat{p}(x)$ is plotted along the length of the duct for angular frequencies of 100 (red), 500 (blue) and 1000 (black) radians/s. $S_1 = 0.2$m, $S_2 = 0.4$m and $\overline{T} = 1000$ K. Modified WKB solution: solid line (——); Standard WKB solution: dotted line ($\cdots\cdots$); Numerical solution: dashed line (- - - -).

WKB method. The absence of a numerical solution for the modified WKB case may be explained based on the observations of Subrahmanyam and Sujith [80]. They showed that a wave-like solution may not be obtained when both $\frac{d\overline{T}}{dx}$ and $\frac{dS}{dx}$ have the same sign. Since both these gradients are positive in the current case, the numerical solution for the modified WKB method fails to converge.

In Figure 4.7, the standard WKB solution and the numerical solution for $\hat{p}(x)$ are plotted. We can see from Figure 4.7 that, the standard WKB solution shows improved agreement with the numerical solution at higher frequencies.
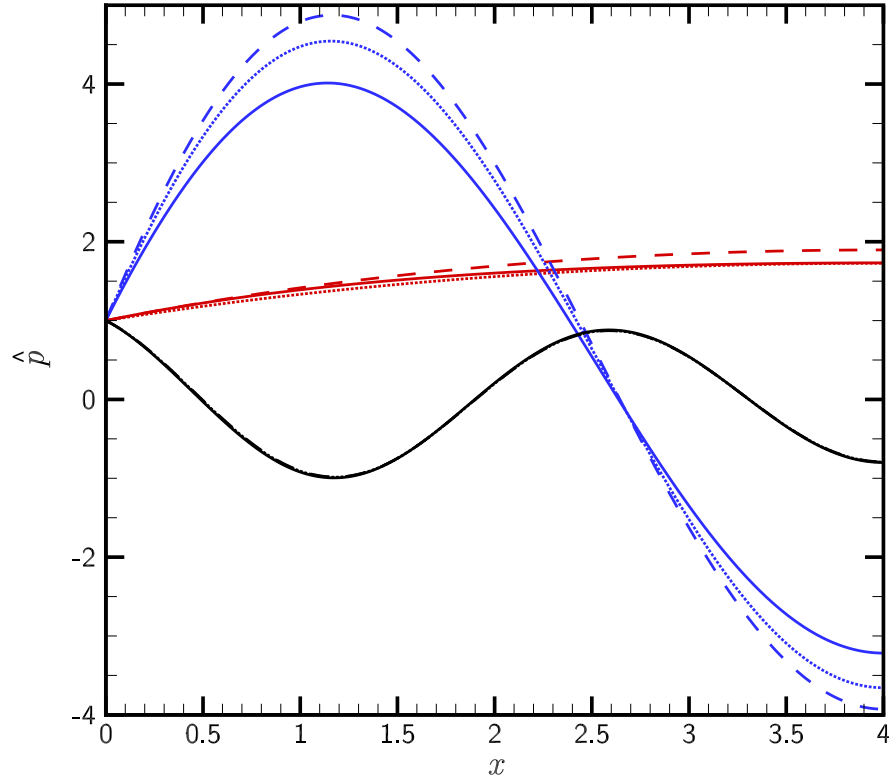

Figure 4.7: Spatial pressure wave $\hat{p}(x)$ is plotted along the length of the duct for angular frequencies of 100 (red), 500 (blue) and 1000 (black) radians/s. Standard WKB solution: dotted line ($\cdots\cdots$); Numerical solution: dashed line (- - - -).

4.4.4 Case 3: $\frac{\mathrm{d}\overline{u}}{\mathrm{d}x} = 0$, $\frac{\mathrm{d}S}{\mathrm{d}x} = 0$ and $\overline{\overline{T}} = mx + T_1$

We now compare the waveforms of a duct with uniform cross-sectional area and mean flow, and a linearly varying temperature profile. The temperature profile

for this case is $\overline{T}(x) = 500 + 125x$, and the duct length is 4m. We consider two inlet Mach numbers $\overline{M}_{\text{inlet}} = 0.1,\ 0.3$ (note that the mean velocity remains constant along the duct, but the mean Mach number and sound speed, $\overline{M}$ and $\bar{c}$, vary continually). Recall from Section 4.3.3 that, for this case, both the standard and modified WKB approaches are the same. Hence, we will just refer to the approximate analytical solution as the WKB solution.

Figure 4.8 shows $\hat{p}(x)$ obtained from the WKB approach as well as the numerical solution (to Eq. (4.32)) as a function of axial location x for $\overline{M}_{\text{inlet}} = 0.1$. We see that the WKB solution agrees quite well with the numerical solution at all frequencies. Even at the lowest frequency ($\Omega = 100$ radians/s), the maximum deviation between the WKB and the numerical solutions is less than 2%.

In Figure 4.9, $\hat{p}(x)$ from the WKB approach as well as the numerical solution is shown for $\overline{M}_{\text{inlet}} = 0.3$. The WKB solution again agrees quite well with the numerical solution at all three frequencies. It may be noted that for $\Omega = 1000$ radians/s, the waveform is seemingly damped close to the inlet, as compared to the waveform in the $\overline{M}_{\text{inlet}} = 0.1$ case.

4.4.5 Prediction of Resonant Frequencies

We now compare the resonant frequencies predicted by the (standard and modified) WKB approaches with those obtained from the exact solutions of Sujith et al. [3] for a uniform duct with a linear mean temperature profile and no mean flow (cf. Case 1 in Section 4.3.1). This exercise was undertaken so as to impart confidence into our subsequent effort to predict combustion instabilities.
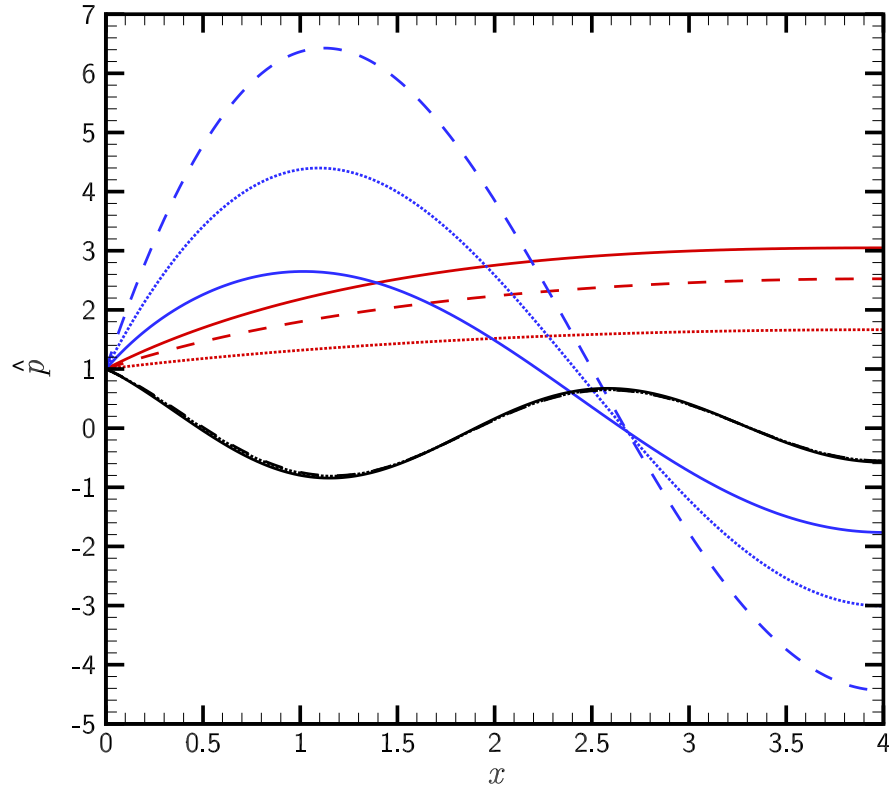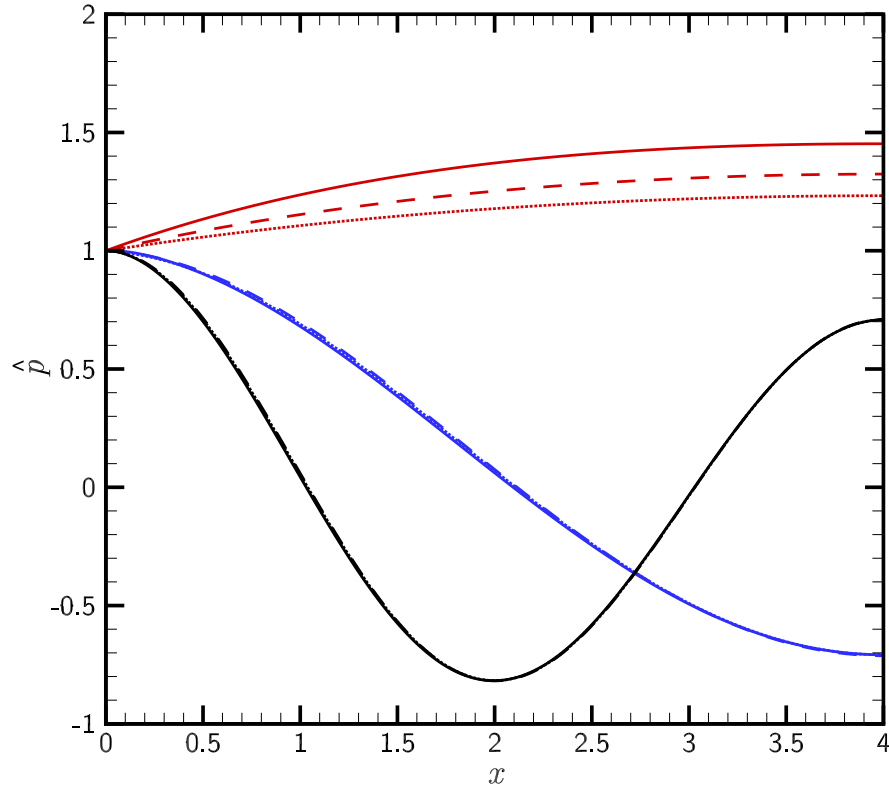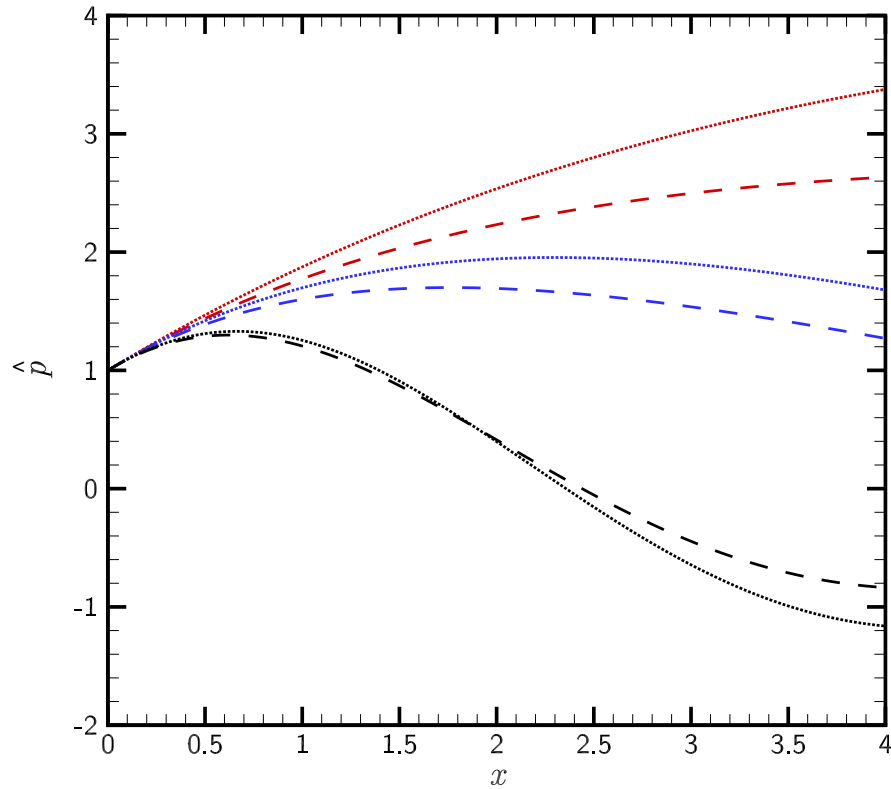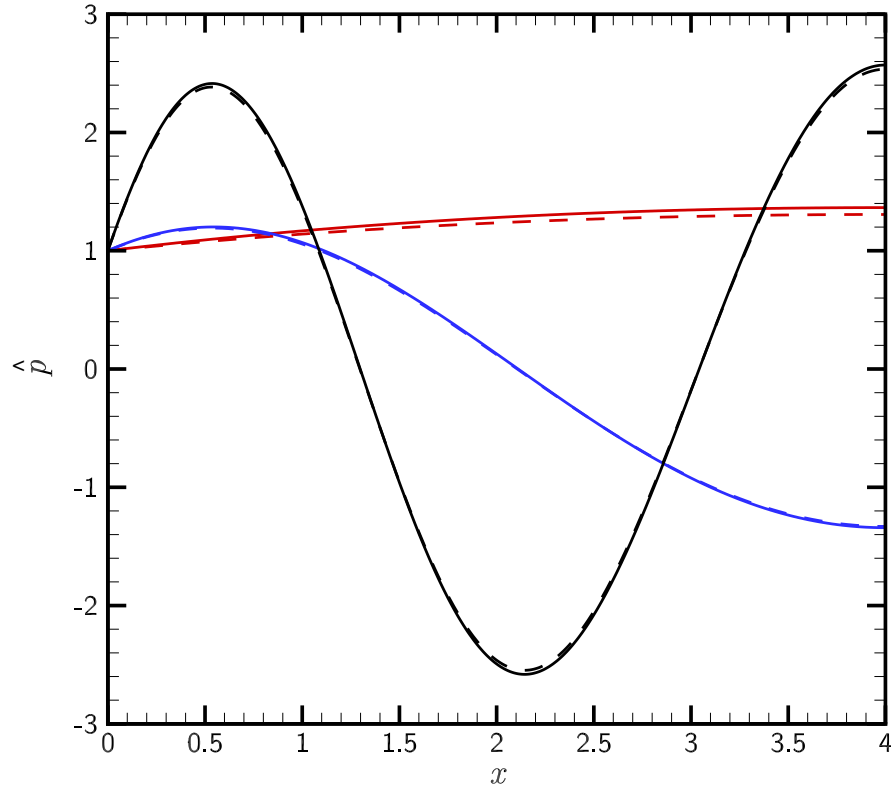
Figure 4.8: Spatial pressure wave $\hat{p}(x)$ is plotted along the length of the duct for angular frequencies of 100 (red), 500 (blue) and 1000 (black) radians/s. WKB solution: solid line (——); Numerical solution: dashed line (- - - -).

Sujith et al. [3] considered four mean temperature profiles with gradients $\frac{d\overline{T}}{dx} = m = -50, -100, -150$ and -200, and a constant outlet temperature $\overline{T}_{\text{out}} = 300$ K. The length of the duct is 4 m. We employ the same boundary conditions as those in Sujith et al., which are: the duct is acoustically closed at the left end ($\left.\frac{dp'}{dx}\right|_{x=0} = 0$), and open at the right end ($p'|_{x=L} = 0$). Using the boundary conditions, a system of
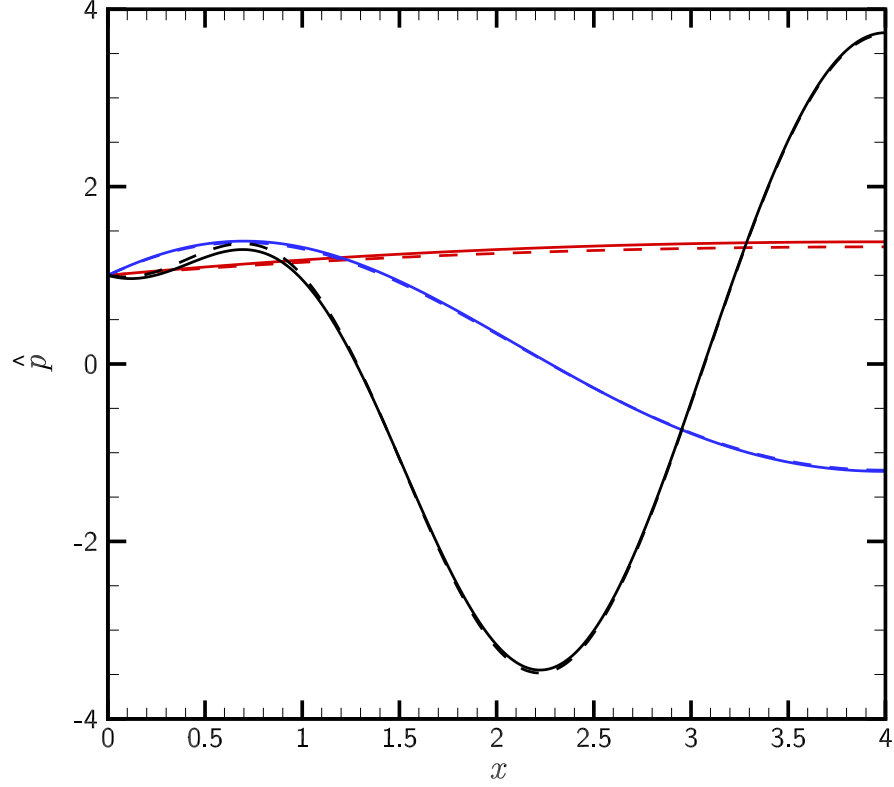
Figure 4.9: Spatial pressure wave $\hat{p}(x)$ is plotted along the length of the duct for angular frequencies of 100 (red), 500 (blue) and 1000 (black) radians/s. WKB solution: solid line (———); Numerical solution: dashed line (- - - -).

homogeneous linear equations in the unknown coefficients $\mathscr{C}^+$ and $\mathscr{C}^-$ is formed:

$$
\begin{pmatrix} \frac{\mathrm{d}}{\mathrm{d}x}\left(A(x)^+e^{\theta(x)^+}\right)\Big|_{x=0} & \frac{\mathrm{d}}{\mathrm{d}x}\left(A(x)^-e^{\theta(x)^-}\right)\Big|_{x=0} \\ \\ A(L)^+e^{\theta(L)^+} & A(L)^-e^{\theta(L)^-} \end{pmatrix} \begin{pmatrix} \mathscr{C}^+ \\ \\ \mathscr{C}^- \end{pmatrix} = \begin{pmatrix} 0 \\ \\ 0 \end{pmatrix} \tag{4.38}
$$

The resonant frequencies of the duct are found by solving the dispersion relation $\det(\mathscr{M}) = 0$, where $\mathscr{M}$ is the coefficient matrix.

Table 4.1 shows the fundamental mode Ω_0, as well as the first four harmonics Ω_1 through Ω_4. In general, we see that both WKB predictions agree quite well with those of Sujith et al. [3]. For the fundamental mode, the resonant frequencies obtained from the standard WKB method are slightly closer to the Sujith et al. results. For all the other harmonics, both WKB methods are in excellent agreement with the Sujith et al. results. We see that as the temperature gradients become steeper, the WKB frequencies show increasing deviation from the exact frequencies. However, across all the cases, the maximum error in the standard WKB solution is less than 3% and that in the modified WKB solution is less than 10% (occurring at Ω_0 with $m = -200$).

Table 4.1: Comparison of the standard and modified WKB solutions with the exact solutions obtained from Sujith et al. [3]. The first four harmonics of the duct (in radians/s) with different gradients in mean temperature profiles are shown.

| $\overline{T}(x) = T_1 + mx$ | T_1 (K) | 500 | 700 | 900 | 1100 |
	m (K/m)	-50	-100	-150	-200
Standard WKB Solution	Ω_0	148.7	159.32	168.77	177.36
	Ω_1	466.14	512.86	553.37	589.64
	Ω_2	779.46	859.09	928.02	989.67
	Ω_3	1092.23	1204.39	1301.43	1388.19
	Ω_4	1404.81	1549.38	1674.43	1786.22
Modified WKB Solution	Ω_0	150.58	164.72	178.09	190.66
	Ω_1	466.83	514.95	557.21	595.41
	Ω_2	779.87	860.36	930.35	993.17
	Ω_3	1092.52	1205.3	1303.1	1390.7
	Ω_4	1405.04	1550.09	1675.72	1788.17
Exact Solution	Ω_0	148.35	158.02	166.38	173.86
	Ω_1	466.4	512.77	552.92	588.73
	Ω_2	780.06	859.54	928.28	989.66
	Ω_3	1093.09	1205.18	1302.13	1388.77
	Ω_4	1405.99	1550.56	1675.54	1787.31

In the following section, we present the results obtained when applying the WKB solution to predict the longitudinal combustion instabilities of a 2-D dump combustor (note that the standard and current WKB solutions coincide for this case).

4.5   Application of WKB method to Predict Combustion Instabilities

We apply the WKB method to predict the longitudinal instabilities of a dump combustor with an area discontinuity, shown in Figure 4.10. The current predictions will be compared with the experimental and modal analysis results of Yu et al. [2]. In their study, Yu et al. [2] considered a 1-D planar flame located at the interface between zones 2 and 3. Thus, all the heat release due to combustion is assumed to take place in an infinitesimally thin plane, and the resulting increase in temperature occurs downstream in zone 3.

The relevant governing equation for this problem is Eq. (4.32). In each of the three zones shown in Figure 4.10, the solution to this equation is considered with the appropriate mean properties. In the current study, zones 1 and 2 have uniform mean velocities and temperatures, whereas zone 3 is considered to have a uniform mean flow, but a linear temperature profile. As a result, in zones 1 and 2, the WKB solution reduces to the conventional modal form of the perturbations, whereas in zone 3, the WKB solution is given by Eqs. (4.35) and (4.36).
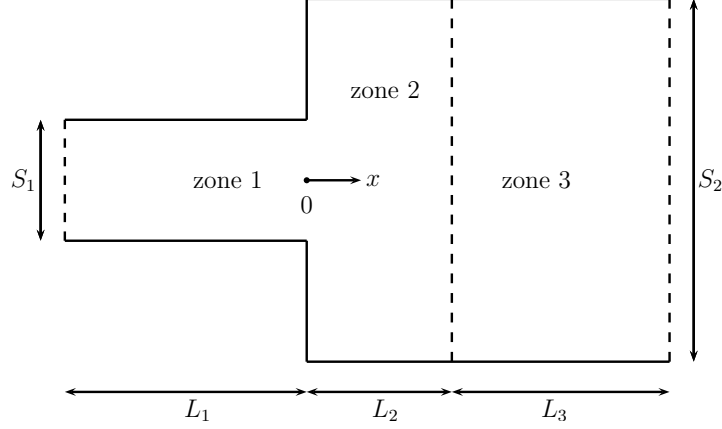
Figure 4.10: Geometry of the dump combustor considered by Yu et al., with the planar mean flame shape indicated using dashed line separating zones 2 and 3.

4.5.1 Acoustic Perturbation Forms

In zones 1 and 2, the acoustic perturbation forms are the standard modal expansions given by [4, 23]

$$
\begin{aligned}
p'_\beta &= e^{i\Omega t}\left(\mathscr{C}^+_\beta e^{ik^+_\beta x} + \mathscr{C}^-_\beta e^{ik^-_\beta x}\right) \\
\rho'_\beta &= \frac{1}{\bar{c}^2_\beta} e^{i\Omega t}\left(\mathscr{C}^+_\beta e^{ik^+_\beta x} + \mathscr{C}^-_\beta e^{ik^-_\beta x}\right) \\
u'_\beta &= -\frac{1}{\bar{\rho}_\beta} e^{i\Omega t}\left(\frac{k^+_\beta}{\Omega + \bar{u}_\beta k^+_\beta}\mathscr{C}^+_\beta e^{ik^+_\beta x} + \frac{k^-_\beta}{\Omega + \bar{u}_\beta k^-_\beta}\mathscr{C}^-_\beta e^{ik^-_\beta x}\right)
\end{aligned}
\tag{4.39}
$$

where $\beta = 1, 2$ is the zonal index and the axial wavenumbers are

$$
k^\pm = \frac{\frac{\Omega \overline{M}}{\bar{c}} \mp \sqrt{\frac{\Omega^2}{\bar{c}^2} - (1 - \overline{M}^2)}}{1 - \overline{M}^2}
\tag{4.40}
$$

Note that in zones 1 and 2, the amplitudes, $\mathscr{C}^+_\beta$ and $\mathscr{C}^-_\beta$, and the wavenumbers, k^+_β and k^-_β, are not functions of x, as the mean flow properties are uniform in these zones.

145

In zone 3, we use the WKB solution for the case with uniform mean flow and a prescribed linear temperature profile (Eqs. (4.35) and (4.36)). Thus, the pressure, density and velocity fluctuations forms, respectively, are

$$p_3' = \left\{ \mathscr{C}_3^+ A_3^+ e^{i\theta_3^+} + \mathscr{C}_3^- A_3^- e^{i\theta_3^-} \right\} e^{i\Omega t} \tag{4.41}$$

$$\rho_3' = \frac{1}{\bar{c}_3^2} \left\{ \mathscr{C}_3^+ A_3^+ e^{i\theta_3^+} + \mathscr{C}_3^- A_3^- e^{i\theta_3^-} \right\} e^{i\Omega t} \tag{4.42}$$

$$u_3' = -\frac{1}{\bar{\rho}_3} \left\{ \mathscr{C}_3^+ \frac{\theta_3^+ \frac{d\theta_3^+}{dx}}{\Omega + \bar{u}_3 \theta_3^+ \frac{d\theta_3^+}{dx}} A_3^+ e^{i\theta_3^+} + \mathscr{C}_3^- \frac{\theta_3^- \frac{d\theta_3^-}{dx}}{\Omega + \bar{u}_3 \theta_3^- \frac{d\theta_3^-}{dx}} A_3^- e^{i\theta_3^-} \right\} e^{i\Omega t} \tag{4.43}$$

where $\mathscr{C}_3^+$ and $\mathscr{C}_3^-$ are the unknown coefficients. The axial velocity fluctuation u' is obtained by substituting Eq. (5.3) into Eq. (4.6) (with $\frac{d\bar{u}}{dx} = 0$).

4.5.2 Matching Conditions

In a prior study [23], we had developed acoustically consistent matching conditions to be applied at zonal interfaces. For the longitudinal modes under consideration, these matching conditions consist of the continuity of acoustic mass velocity ($\rho u S$) and of the total pressure ($p + \frac{1}{2}\rho u^2$), where S is the zonal cross-sectional area.

At a zonal interface located at x (say, between zones 1 and 2), the continuity of acoustic mass velocity is given by

$$[\rho_1 u_1 S_1]_x = [\rho_2 u_2 S_2]_x \tag{4.44}$$

which upon linearization yields

$$[\rho'_1\overline{u}_1 + \overline{\rho}_1 u'_1]_x = [\rho'_2\overline{u}_2 + \overline{\rho}_2 u'_2]_x \tag{4.45}$$

Similarly, the linearized form of the continuity of total pressure is

$$[p'_1 + \overline{\rho}_1\ \overline{u}_1\ u'_1 + \frac{1}{2}\rho'_1\ \overline{u}_1^2]_x = [p'_2 + \overline{\rho}_2\ \overline{u}_2\ u'_2 + \frac{1}{2}\rho'_2\ \overline{u}_2^2]_x \tag{4.46}$$

Similar matching conditions are applied between zones 2 and 3.

4.5.3 Equation Assembly and Solution

The zonal matching conditions along with the boundary conditions (for zones 1 and 3) are assembled into an equation of the following form:

$$\mathcal{M}\mathcal{C} = 0 \tag{4.47}$$

where $\mathcal{C}$ is the vector of unknown coefficients and $\mathcal{M}$ is the coefficient matrix. The resonant frequencies are obtained from $\det(\mathcal{M}) = 0$. Since the resonant frequencies can be complex, the system is regarded as being unstable when the imaginary part of Ω is negative (due to the $e^{i\Omega t}$ functionality).

4.5.4 Combustion Instability Prediction

The combustion instabilities predicted using the current WKB solution are compared with the experimental and modal analysis results of of Yu et al. [2]. The

geometric parameters and the mean flow properties, same as those in the Yu et al. study, are provided in Table 4.2. Yu et al. assumed a uniform mean temperature

Table 4.2: Geometric parameters and mean flow properties in the three-zone dump combustor considered in Yu et al. [2] (see Figure 4.10).

	Zone 1	Zone 2	Zone 3
Length (m)	0.171	0.038	0.215
Height (m)	0.0225	0.0450	0.0450
Mach number, $\overline{M}$	0.265	0.0548	0.0933
Temperature, $\overline{T}$ (K)	1020	1030	2660
Speed of sound, $\bar{c}$ (ms^{-1})	698	701	1110
Density, $\bar{\rho}$ (kg·m^{-3})	7.53	5.92	2.20
Pressure, $\bar{p}$ (MPa)	2.27	2.29	2.28

in zone 3, whereas we considered a linear temperature profile. The effects of two temperature gradients on the instability predictions are investigated, as shown in Table 4.3. In the first case, the left and right ends of zone 3 are held at 2700 K and 2620 K (resulting in a relatively gentle temperature gradient). In the second case, the left and right ends are held at 2800 K and 2520 K (resulting in a steeper temperature gradient). For both cases, the temperature at the center of zone 3 is maintained at 2660 K, which is the mean temperature considered by Yu et al. [2]. The mean Mach number and the speed of sound for the two cases are also indicated in Table 4.3.

In Table 4.4, the unstable longitudinal frequencies predicted by our approach are compared with the experimental and analytical results of Yu et al. [2]. For both temperature gradient (TG) cases, it can be seen that the current instability predictions are in excellent agreement with the experimental predictions of Yu et al. In fact, the WKB results show better agreement with the experimental data than the

148

Table 4.3: Geometric parameters and mean flow properties in zone 3 of the dump combustor (see Figure 4.10).

	Zone 3 Case 1	Zone 3 Case 2
Mach number, $\overline{M}$	$\dfrac{5.167}{\sqrt{2700-372.09(x-0.038)}}$	$\dfrac{5.167}{\sqrt{2800-1302.33(x-0.038)}}$
Temperature, $\overline{T}$ (K)	$2700-372.09(x-0.038)$	$2800-1302.33(x-0.038)$
Speed of sound, $\overline{c}$ (ms^{-1})	$20.045\sqrt{2700-372.09(x-0.038)}$	$20.045\sqrt{2800-1302.33(x-0.038)}$

analytical predictions of Yu et al. Further, the frequencies for the smaller TG case are closer to the experimental results than those for the higher TG case. This may be because the WKB method is based on the approximation of slowly varying mean properties.

Table 4.4: Comparison of unstable longitudinal frequencies obtained from the WKB method (Cases 1 and 2) with those from the experiments and 1-D modal analysis of Yu et al. [2].

Frequency (Hz)	Experimental (Yu et al.)	1-D Analytical (Yu et al.)	Current Study (Case 1)	Current Study (Case 2)
Fundamental (Ω_{10})	1905	1997	1909	1938
First harmonic (Ω_{20})	3890	3785	3903	3921
Second harmonic (Ω_{30})	5610	5878	5608	5642

4.6 Summary

A number of WKB-type solutions were developed for ducts with uniform and linearly varying mean temperatures and cross-sectional areas (with and without mean

flow). Comparison of pressure waveforms from the standard and modified WKB methods shows that the two approaches result in broadly similar solutions. The WKB approaches were also used to predict the resonant frequencies of a uniform duct with no mean flow and linearly varying mean temperature. The frequencies predicted by both approaches are in good agreement with those from the exact solutions of Sujith et al. [3]. The WKB approach is then applied to predict the longitudinal instabilities of a dump combustor. The instability frequencies are found to be in excellent agreement with the experimental results of Yu et al. [2].

CHAPTER 5

THE EFFECTS OF ACOUSTIC AND COMBUSTION SOURCE TERM NONLINEARITIES ON THE LIMIT-CYCLE BEHAVIOR OF THERMOACOUSTIC INSTABILITIES

5.1 Abstract

A Linear analysis of combustion instabilities fails to capture the finite-amplitude limit cycle behavior of the pressure oscillations. Hence, a nonlinear framework is necessary to be able to predict this behavior. It is known that, for moderate amplitudes and low-Mach-number mean flow, the unsteady combustor flow can be described by a single nonlinear wave equation. This equation is solved numerically for the first two coupled longitudinal modes. Computed results predict the existence of both stable modes and unstable modes with finite-amplitude limit cycles. The unstable frequencies are obtained from a linear analysis of the system. The effects of acoustic and combustion source term nonlinearities on the stability of the system are investigated. It is found that, in the low Mach number regime, the nonlinearities arinsing from combustion source term have a greater impact on the pressure oscillations than the purely acoustic nonlinearites.

5.2 Introduction

Combustion instabilities represent one of the most significant problems encountered in the design of propulsion systems [82, 83]. Combustion instabilities are manifested as self-excited acoustic oscillations that are sustained by a feedback loop between the acoustic perturbations and the heat-release fluctuations. The Rayleigh criterion [14, 22, 24–26] suggests that instabilities occur when the net acoustic energy pumped into the system due to the pressure–heat-release feedback exceeds the energy losses due to various mechanisms (e.g., acoustic radiation and viscous losses). Reduced order analytical approaches, such as the linear modal analysis [2, 4, 5, 11–14, 23, 27] and Nyquist-plot-based network models [28–33], are commonly used to predict the instability modes. These linear reduced-order methods, however, cannot predict the limit-cycle behavior that most physical systems exhibit.

It is essential to model the nonlinearities in a system to capture the limit-cycle behavior. For small unsteady fluctuations, the dissipative mechanisms are relatively weak, hence many combustion systems are linearly unstable. The exponential growth of initial disturbances occurs until larger dissipative mechanisms are generated within the system, and determine the stabilization of the fluctuations to a limiting amplitude. Two main conclusions can be drawn from these observations. The formation of limiting unsteady motions is the result of very complex nonlinear mechanical and chemical processes. For this reason, analytical investigation of the problem can be based only on simplified, empirical models of the combustion system, obtained from experimental and numerical investigations.

The earliest analytical models were based on the derivation of simplified non-linear equations for the amplitudes of the acoustic modes. Zinn and Powell [84, 85] obtained such equations for the case of liquid propellant rockets, by spatial averaging of the conservation equations. Their results were limited to numerical integration of the derived equations, and no closed form solutions were produced for the amplitudes in the limit cycle. A similar approach was independently followed by Culick [86], for the case of solid rocket engines. The analysis was based on derivation of a semi-empirical nonlinear equation for the amplitude of the fundamental mode. Further experimental evidence showed the deficiency of the approach, by suggesting that the observed limit cycles are the result of nonlinear coupling between multiple acoustic modes.

Based on those preliminary results, Culick [87] introduced a more general approximate method, based on general expansion of the conservation equations in terms of the amplitudes of the acoustic modes. Although the initial solution scheme did not appear well-founded theoretically, the derived equations were identical with the ones obtained using a Galerkin type of approach. Experimental and numerical data indicate that for most practical applications, the characteristics of the unsteady field in the spatial and frequency domains are approximately given by the linear acoustic analysis. For this reason, the approximate method is physically and theoretically motivated, and can be used in the analysis of any combustion related instabilities.

In this study, we first derive the nonlinear wave equation with combustion source term for a 1-D Rijke tube. Two longitudinal modes are considered: fundamental and the first harmonic. Two coupled nonlinear wave equations are derived in

153

terms of these modal amplitudes. We analyze the stability criteria for the system in the linear limit. We solve the coupled nonlinear ODEs numericaly for the amplitudes of the system. We the effects of acoustic and combustion source term nonlinearities on the the limit-cycle behavior of the system.
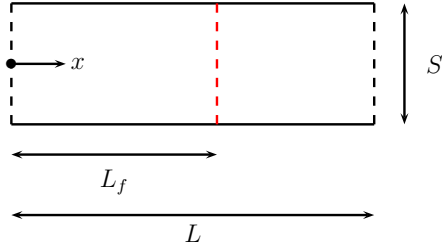
5.3 Theory

Figure 5.1: Geometry of the 1-D duct with the planar flame shown in red.

For a 1-D Rijke tube shown in Figure 5.1, wtih no gradients in mean properties, the wave equation (1.10) reduces to:

$$\frac{1}{\bar{c}^2}\frac{\partial^2 p'}{\partial t^2} - \frac{\partial^2 p'}{\partial x^2} = \bar{\rho}\frac{\partial^2 u'}{\partial x \partial t} - \frac{\bar{u}}{\bar{c}^2}\frac{\partial^2 p'}{\partial x \partial t} + \bar{u}\frac{\partial^2 u'}{\partial x^2} + \frac{1}{\bar{c}^2}\frac{\partial p'}{\partial x}u'\frac{\partial u'}{\partial x} + \frac{p'}{\bar{c}^2}\left(\frac{\partial u'}{\partial x}\right)^2 + \frac{p'}{\bar{c}^2}u'\frac{\partial^2 u'}{\partial x^2}$$
$$- \frac{u'}{\bar{c}^2}\frac{\partial^2 p'}{\partial x \partial t} - \frac{1}{\bar{c}^2}\frac{\partial p'}{\partial t}\frac{\partial u'}{\partial x} + \bar{\rho}\left(\frac{\partial u'}{\partial x}\right)^2 + \bar{\rho}u'\frac{\partial^2 u'}{\partial x^2} + \frac{\gamma - 1}{\bar{c}^2}\frac{\partial q'}{\partial t}$$

$$(5.1)$$

where $\bar{u}$ and u' are the mean and fluctuating components of axial velocity. Since we neglected the dissipation terms to obtain Eq. (5.1), we may add a damping term of the form $\mathscr{D}\frac{\partial p'}{\partial t}$ (where $\mathscr{D}$ is the damping coefficient) to Eq. (5.1). Thus we get the

damped nonliear wave equation with source terms:

$$\frac{1}{\bar{c}^2}\frac{\partial^2 p'}{\partial t^2} + \mathscr{D}\frac{\partial p'}{\partial t} - \frac{\partial^2 p'}{\partial x^2} = \bar{\rho}\frac{\partial^2 u'}{\partial x\partial t} - \frac{\bar{u}}{\bar{c}^2}\frac{\partial^2 p'}{\partial x\partial t} + \bar{u}\frac{\partial^2 u'}{\partial x^2} + \frac{1}{\bar{c}^2}\frac{\partial p'}{\partial x}u'\frac{\partial u'}{\partial x} + \frac{p'}{\bar{c}^2}\left(\frac{\partial u'}{\partial x}\right)^2 + \frac{p'}{\bar{c}^2}u'\frac{\partial^2 u'}{\partial x^2}$$

$$- \frac{u'}{\bar{c}^2}\frac{\partial^2 p'}{\partial x\partial t} - \frac{1}{\bar{c}^2}\frac{\partial p'}{\partial t}\frac{\partial u'}{\partial x} + \bar{\rho}\left(\frac{\partial u'}{\partial x}\right)^2 + \bar{\rho}u'\frac{\partial^2 u'}{\partial x^2} + \frac{\gamma - 1}{\bar{c}^2}\frac{\partial q'}{\partial t}$$

(5.2)

5.3.1 Solving the Nonlinear Wave Equation

Equation (5.2) is a nonlinear PDE with three unknowns p', u' and q'. We first

have to reduce the number of unknowns to one to be able to solve the wave equation.

That is accomplished by relating u' to p' using the linearized momentum equation.

We then use a flame transfer function (FTF) to relate heat-release rate fluctuations

q' to either p' or u'.

In the limit-cycle analysis of the nonlinear wave equation, temporal growth

of the acoustic fluctuations (p' and u') is the quantity of interest. For a duct with

prescribed boundary conditions, we assume a harmonic spatial dependence of p' in x

and substitute that into Eq. (5.2) to get an ODE in time. We assume the following

forms for p' and u', corresponding to closed-closed ($\frac{\mathrm{d}p'}{\mathrm{d}x}\big|_{x=0} = \frac{\mathrm{d}p'}{\mathrm{d}x}\big|_{x=L} = 0$) boundary

conditions:

$$p' = \sum_{n=1}^{\infty} A_n(t)\cos k_n x \tag{5.3}$$

$$u' = -\frac{1}{\gamma\bar{\rho}\bar{c}^2}\sum_{n=1}^{\infty}\frac{1}{k_n}\frac{\mathrm{d}A_n(t)}{\mathrm{d}t}\sin k_n x \tag{5.4}$$

where A_n and k_n are the amplitude and wavenumbers of the nth mode of the fluctuation. Wavenumbers are related to the frequency as $k_n = n\frac{\Omega_1}{\bar{c}}$ (where Ω_1 is the fundamental mode). In this study, we cut off the summation at $n = 2$. So, we have to solve for two modal amplitudes $A_1(t)$ and $A_2(t)$.

5.3.1.1 Flame Transfer Function

In this study, we relate heat-release rate flcutuations q' to pressure fluctuations p' using a nonlinear FTF given by (**citation needed**):

$$q' = \bar{q}\left[0.2\left(\frac{p'}{\bar{p}}\right) + \left(\frac{p'}{\bar{p}}\right)^3 - \left(\frac{p'}{\bar{p}}\right)^5\right]e^{-i\Omega\tau} \tag{5.5}$$

where $\bar{q}$ is the mean heat-release rate per unit volume and τ is the convective time-lag.

5.3.1.2 Solution Procedure

Substituting Eqs. (5.3), (5.4) and (5.5) in Eq. (5.2) after truncating the summation at $n = 2$, we get an ODE in $A_1(t)$ and $A_2(t)$. Further, we multiply this ODE by $\cos(k_N x)$ (where $N = 1, 2$) and using orthogonality of the cosine and sine functions and integrating in x from 0 to L, we get two coupled nonlinear ODEs in $A_1(t)$ and $A_2(t)$.

We now have two second order nonlinear ODEs in A_1 and A_2. We solve these ODEs numerically using the following initial conditions:

$$A_1(t = 0) \quad = \quad 0.05 \tag{5.6}$$

$$\left. \frac{\mathrm{d}A_1}{\mathrm{d}t} \right|_{t=0} \quad = \quad 0.005 \tag{5.7}$$

$$A_2(t = 0) \quad = \quad 0.035 \tag{5.8}$$

$$\left. \frac{\mathrm{d}A_2}{\mathrm{d}t} \right|_{t=0} \quad = \quad -0.1 \tag{5.9}$$

$$\tag{5.10}$$

5.3.2 Linear Stability

In order to study the effects of nonlinear source terms on the wave equation, we first analyze the linear wave equation. From Eq. (5.2), retaining only the linear terms, we get

$$\frac{1}{\bar{c}^2} \frac{\partial^2 p'}{\partial t^2} + \mathscr{D} \frac{\partial p'}{\partial t} + 2 \frac{\overline{M}}{\bar{c}} \frac{\partial^2 p'}{\partial t \partial x} + \left(\overline{M}^2 - 1 \right) \frac{\partial^2 p'}{\partial x^2} = \frac{\gamma - 1}{\bar{c}^2} \frac{\partial q'}{\partial t} \tag{5.11}$$

where $\overline{M} = \frac{\bar{u}}{\bar{c}}$ is the mean Mach number. Considering only a single mode (for simplicity), we assume the following forms for p' and q':

$$p' \quad = \quad A(t) \cos kx \tag{5.12}$$

$$q' \quad = \quad \bar{q} \frac{p'}{\bar{p}} e^{-i\Omega\tau} \tag{5.13}$$

157

where $k = \Omega/\bar{c}$. Substituting the above forms of p' and q' in Eq. (5.11), we get

$$\frac{1}{\bar{c}^2}\frac{\mathrm{d}^2 A}{\mathrm{d}t^2}\cos kx + \mathscr{D}\frac{\mathrm{d}A}{\mathrm{d}t}\cos kx - 2k\frac{\overline{M}}{\bar{c}}\frac{\mathrm{d}A}{\mathrm{d}t}\sin kx - \left(\overline{M}^2 - 1\right)k^2 A\cos kx = \frac{\gamma-1}{\bar{c}^2}\frac{\bar{q}}{\bar{p}}\frac{\mathrm{d}A}{\mathrm{d}t}e^{-i\Omega\tau}\cos kx$$

(5.14)

Multiplying Eq. (5.14) by $\cos kx$ and integrating from 0 to L in x,

$$\frac{1}{\bar{c}^2}\frac{\mathrm{d}^2 A}{\mathrm{d}t^2} + \left(\mathscr{D} - \frac{\gamma-1}{\bar{c}^2}\frac{\bar{q}}{\bar{p}}e^{-i\Omega\tau}\right)\frac{\mathrm{d}A}{\mathrm{d}t} + \left(1 - \overline{M}^2\right)k^2 A = 0$$

(5.15)

Substituting $A = e^{\sigma t}$ (where σ is the growth rate) in Eq. (5.15), we have

$$\sigma = \frac{\bar{c}^2}{2}\left\{-\left(\mathscr{D} - \frac{\gamma-1}{\bar{c}^2}\frac{\bar{q}}{\bar{p}}e^{-i\Omega\tau}\right) \pm \sqrt{\left(\mathscr{D} - \frac{\gamma-1}{\bar{c}^2}\frac{\bar{q}}{\bar{p}}e^{-i\Omega\tau}\right)^2 - 4\left(1 - \overline{M}^2\right)\frac{\Omega^2}{\bar{c}^4}}\right\}$$

(5.16)

In the case when there is no damping, linear growth rate is given by

$$\sigma = \frac{\gamma-1}{2}\frac{\bar{q}}{\bar{p}}e^{-i\Omega\tau} \pm \sqrt{\left((\gamma-1)\frac{\bar{q}}{\bar{p}}e^{-i\Omega\tau}\right)^2 - 4\left(1 - \overline{M}^2\right)\Omega^2}$$

(5.17)

Taking the real part of $e^{-i\Omega\tau}$, we have

$$\sigma = \frac{\gamma-1}{2}\frac{\bar{q}}{\bar{p}}\cos\Omega\tau \pm \frac{1}{2}\sqrt{\left((\gamma-1)\frac{\bar{q}}{\bar{p}}\cos\Omega\tau\right)^2 - 4\left(1 - \overline{M}^2\right)\Omega^2}$$

(5.18)

For a stable solution,

$$\frac{\gamma-1}{2}\frac{\bar{q}}{\bar{p}}\cos\Omega\tau < 0$$

(5.19)

$$\Rightarrow \frac{\pi}{2\Omega} < \tau < \frac{3\pi}{2\Omega}; \ \frac{5\pi}{2\Omega} < \tau < \frac{7\pi}{2\Omega}...$$

(5.20)

And the solution will be linearly unstable when

$$0 < \tau < \frac{\pi}{2\Omega}; \ \frac{3\pi}{2\Omega} < \tau < \frac{5\pi}{2\Omega}... \quad (5.21)$$

In this study, we will analyze the limit-cycle behavior in the linearly unstable regime and investigate the effects of acoustic as well as combustion nonlinear source terms. We also study the effects of damping or the lack thereof on the nature of instability.

5.4   Results

Here we present the numerical results of solution to Eq. (5.2). Table 5.1 shows the mean properties used in the numerical solutions. In this work, since we are interested in studying the limit-cycle behavior of the thermoacoustic system, we only choose those frequencies that are linearly unstable.

Table 5.1: Mean properties

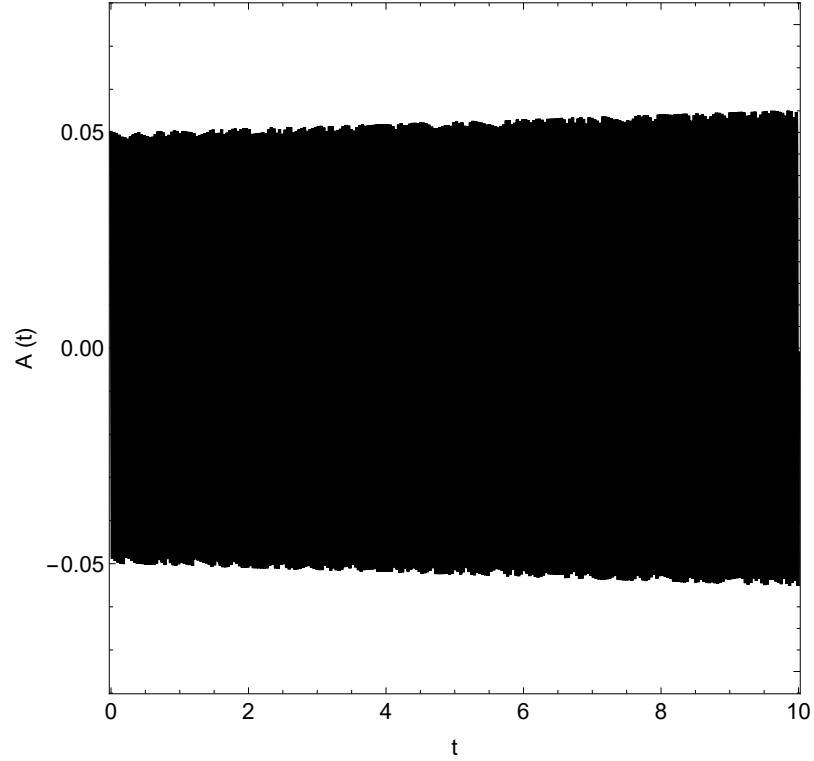| Mean properties	Values
Length, L (m)	10
Mach number, $\overline{M}$	0.1
Speed of sound, $\overline{c}$ (m/s)	500
Damping coefficient, $\mathscr{D}$ (s^{-1})	0
Pressure, $\overline{p}$ (N/m^3)	10000
Fundamental mode, Ω_1 (radians/s)	400
First harmonic, Ω_2 (radians/s)	800
Convective time-lag, τ (s)	$\frac{\pi}{3\Omega_1}$

Figure 5.2: Amplitude of the fundamental mode A in the linear regime is plotted as a function of time. Mean heat-release rate per unit volume $\overline{q}$ is 10000 W/m^3.

Figure 5.2 shows the amplitude of the fundamental mode ($\Omega = 400$ radians/s) A in the linear regime plotted as a function of time. The mean heat-release rate $\overline{q}$ is 10000 W/m^3. Convective time-lag $\tau = \pi/1200$s, which makes the system linearly unstable (see Eq. (5.21)). Here damping coefficient is set to 0. We can clearly see from Figure 5.2 that the amplitude is growing in time, and threfore temporally unstable.
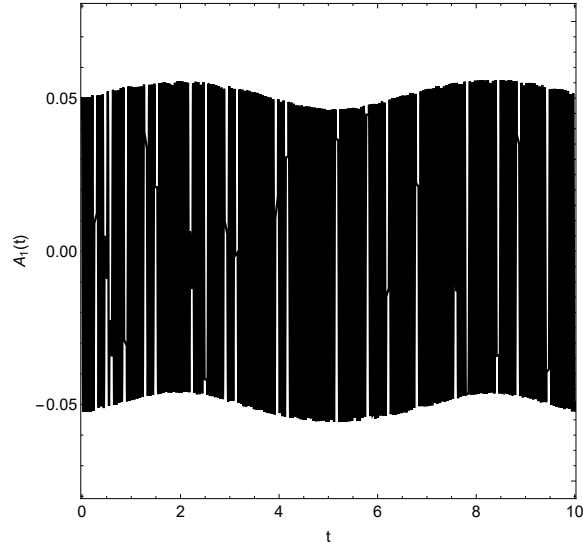
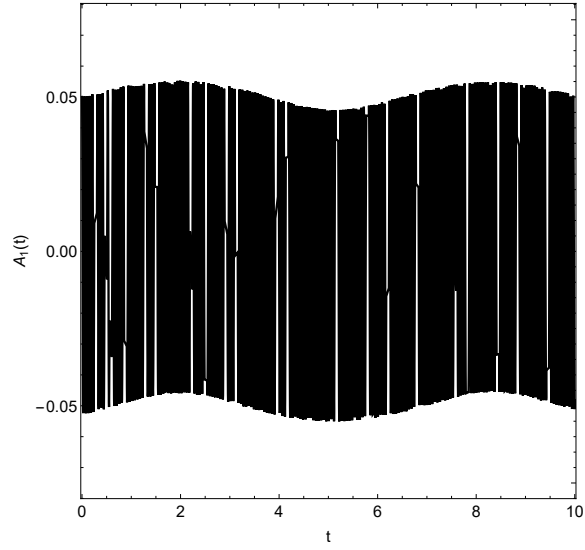(a)
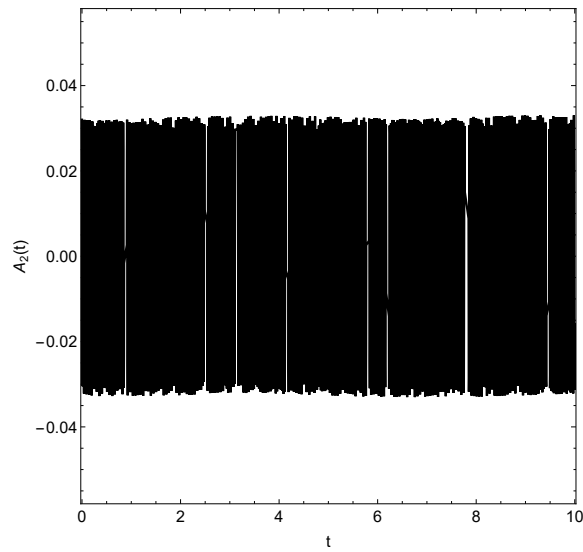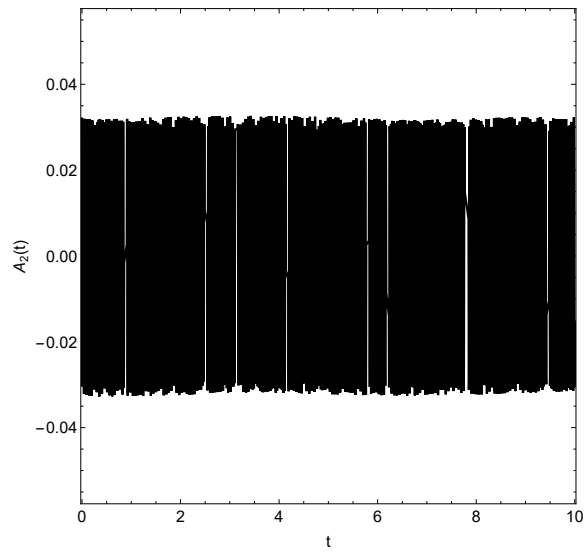

(b)

Figure 5.3: Amplitude of the (a) fundamental A_1 and (b) the first harmonic A_2 are plotted as a function of time. Only acoustic nonlinearities are considered. Mean heat-release rate per unit volume $\bar{q}$ is 10000 W/m^3.

Figure 5.3 shows the amplitudes of the fundamental ($\Omega_1 = 400$ radians/s) A_1 and the first harmonic ($\Omega_2 = 800$ radians/s) A_2 as a function of time. Mean heat-release rate per unit volume $\bar{q}$ is 10000 W/m^3 and $\tau = \pi/1200$s. Here only the acoustic nonlinearities are considered i.e., only the linear component of the FTF (5.5) is considered. From Figure 5.3, we can see that both amplitudes A_1 and A_2 have reached limit-cycle and the system is no longer unstable. In contrast to the linear analysis (shown in Figure 5.2) which predicts the system to be unstable, the addition of acoustic nonlinearities have stabilized the system. It is also interesting to see from Figure 5.3(a) that there are at least three distinct frequencies in A_1. We are not sure if these distinct frequencies are also present in A_2 and, in the linear case A.

(a)

(b)

Figure 5.4: Amplitude of the (a) fundamental A_1 and (b) the first harmonic A_2 are plotted as a function of time. Only combustion source term nonlinearities are considered. Mean heat-release rate per unit volume $\bar{q}$ is 10000 W/m^3.

Figure 5.4 show A_1 and A_2 as a function of time. In this case only the combustion source term nonlinearities are considered and the acoustic nonlinearities are neglected. The amplitudes show very similar behavior as in the previous case with just the acoustic nonlinearities turned on. Similarly in Figure 5.5, where the amplitudes are computed with both the acoustic and combustion source term nonlinearities included, show very similar behavior to Figure 5.3 and Figure 5.4.
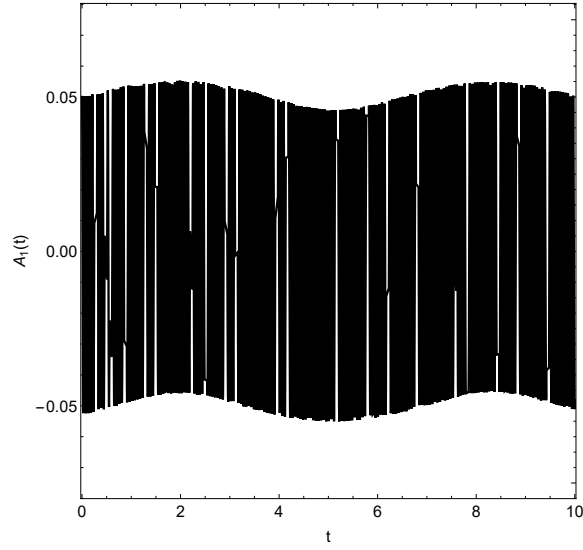
(a)

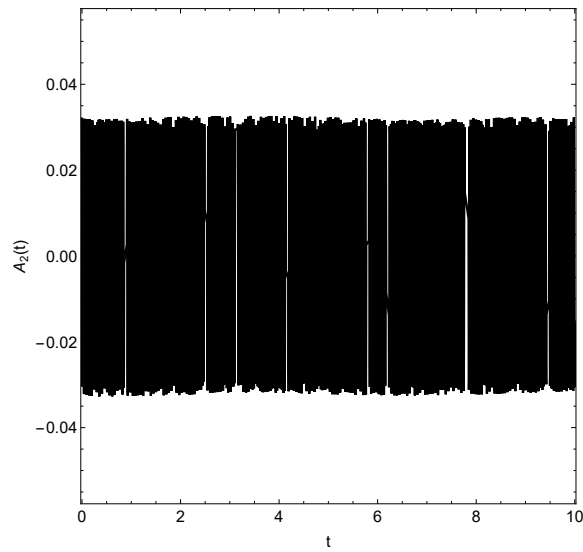(b)

Figure 5.5: Amplitude of the (a) fundamental A_1 and (b) the first harmonic A_2 are plotted as a function of time. Both acoustic and combustion source term nonlinearities are considered. Mean heat-release rate per unit volume $\overline{q}$ is 10000 W/m^3.

Figure 5.6 shows the amplitude of the fundamental mode in the linear regime with $\bar{q} = 100000$ W/m^3. The rest of the mean properties are the same as in the previous case. As expected, the fundamental mode is linearly unstable. Compared to Figure 5.2, in this case, we can clearly see a much steeper increase in the A, which is to be expected as the growth rate is proportional to heat-release rate $\sigma \propto \bar{q}$ (see Eq. (5.17)).
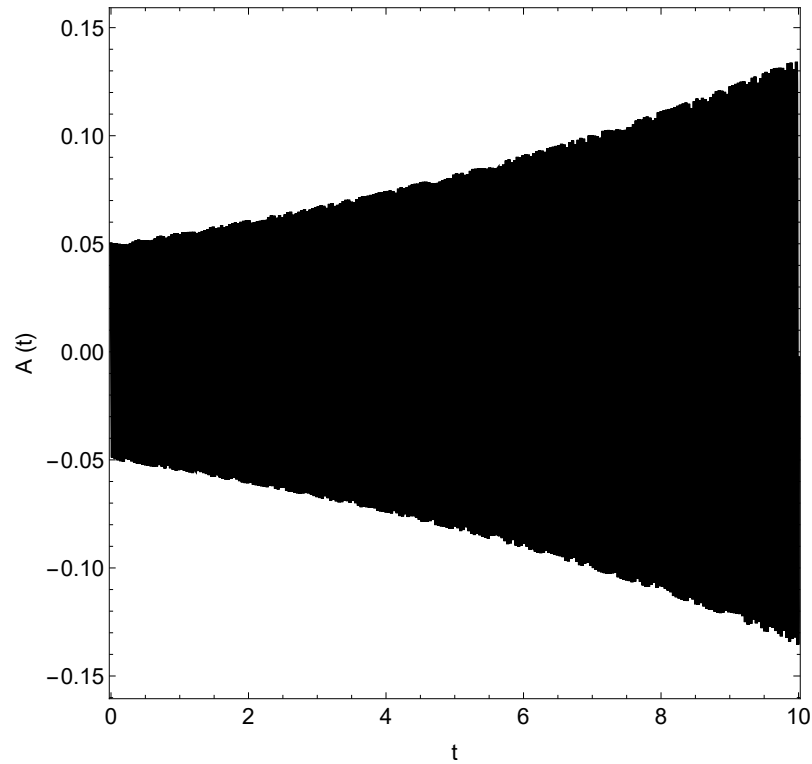
Figure 5.6: Amplitude of the fundamental mode A in the linear regime is plotted as a function of time. Mean heat-release rate per unit volume $\bar{q}$ is 100000 W/m^3.

Figure 5.7 shows the amplitudes of the fundamental A_1 and the first harmonic A_2 as a function of time for $\bar{q} = 100000$ W/m^3. Here only the acoustic nonlinearities

are included. We can see from Figure 5.7, that both A_1 and A_2 are increasing in time. Even though the growth rate has reduced considerably when compared to the purely linear regime (Figure 5.2), the acoustic nonlinearities are not able to attain a stable limit-cycle in this case.
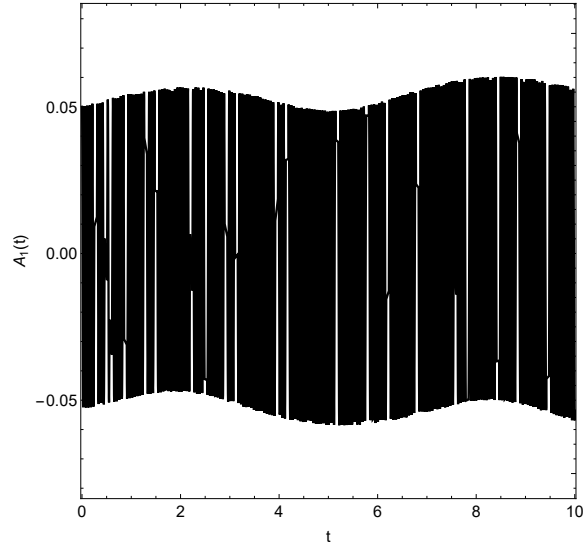
(a)
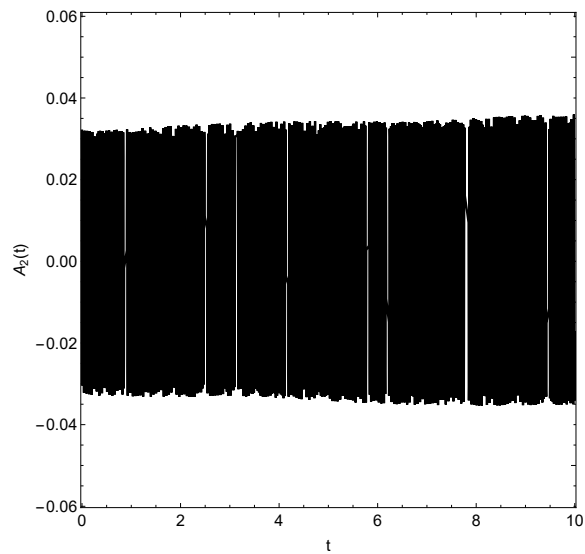
(b)

Figure 5.7: Amplitude of the (a) fundamental A_1 and (b) the first harmonic A_2 are plotted as a function of time. Only acoustic nonlinearities are considered. Mean heat-release rate per unit volume $\bar{q}$ is 100000 W/m^3.

In Figure 5.7, A_1 and the first harmonic A_2 are shown as a function of time for $\overline{q} = 100000$ W/m^3. Here only the acoustic nonlinearities are considered. In stark contrast to the previous case (Figure 5.7), here the combustion source term nonlinearities are able to contain the temporal growth of the amplitudes. This tells us that, in this case, nonlinearities arising from the combustion source term are more dominant than their purely acoustic counterparts. Figure 5.9 shows the amplitudes considering both acoustic and combustion source term nonlinearities. The amplitudes in this case are quite similar to Figure 5.7, indicating that the addition of acoustic nonlinearities does not much affect the solution i.e., heat-release rate nonlinearites are more dominant than acoustic nonlinearities.

Figure 5.8: Amplitude of the (a) fundamental A_1 and (b) the first harmonic A_2 are plotted as a function of time. Only combustion source term nonlinearities are considered. Mean heat-release rate per unit volume $\bar{q}$ is 100000 W/m^3.
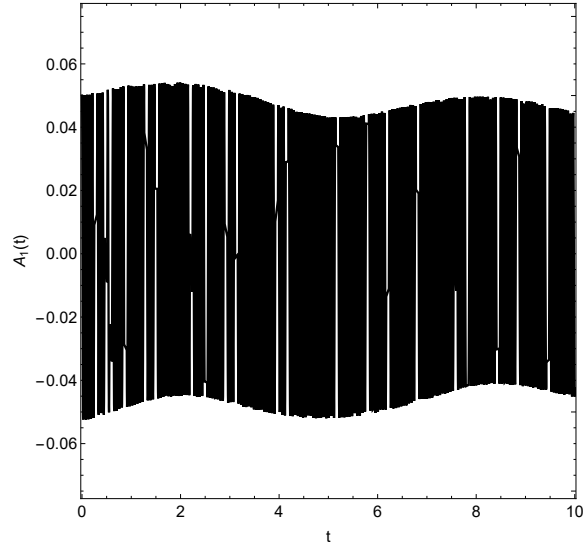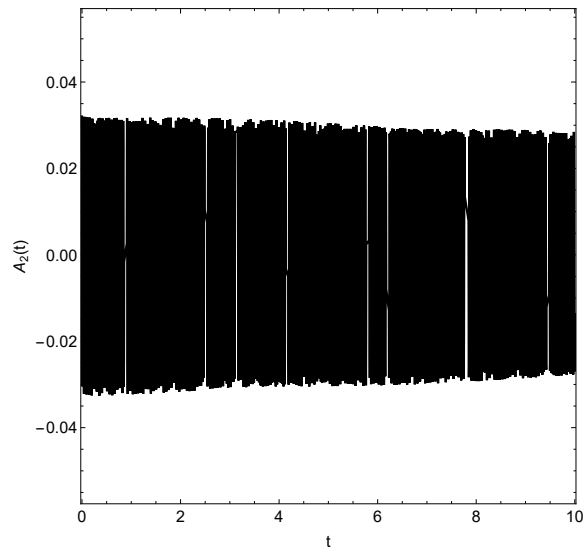
(a)

(b)

Figure 5.9: Amplitude of the (a) fundamental A_1 and (b) the first harmonic A_2 are plotted as a function of time. Both acoustic and combustion source term nonlinearities are considered. Mean heat-release rate per unit volume $\overline{q}$ is 100000 W/m^3.

Figure 5.10 shows the amplitude of the fundamental mode in the linear regime with $\bar{q} = 1000000$ W/m^3. Here $\bar{q}$ is so large that we see an exponential increse in the amplitude.
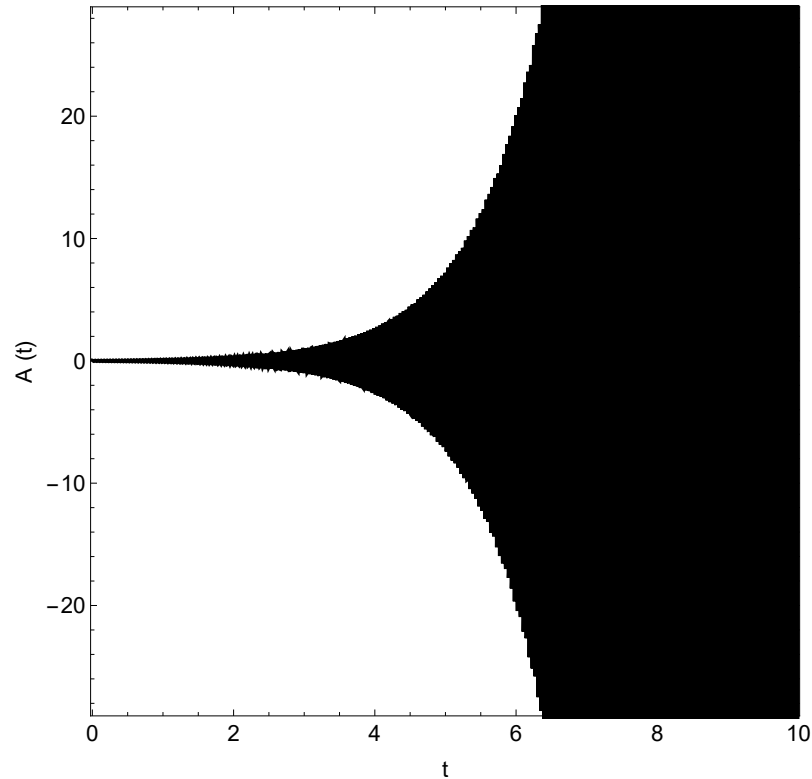
Figure 5.10: Amplitude of the fundamental mode A in the linear regime is plotted as a function of time. Mean heat-release rate per unit volume $\bar{q}$ is 1000000 W/m^3.

Figure 5.11 shows A_1 and A_2 as a function of time for $\bar{q} = 100000$ W/m^3. Both acoustic and combustion nonlinearities are considered. We can see from Figure 5.11 that while the nonlinearities are able to rein in the growth of A_2, the amplitude of the fundamental mode A_1 appears to be increasing in time. That is, the fundamental

mode is not just linearly unstable but also nonlinearly unstable even after inlcuding both the acoustic and combustion nonlinearities.

In such cases where even the system is even nonlinearly unstable, damping can help contain the growth. So far, the damping coefficient $\mathscr{D}$ in Eq. (5.2) is set to zero. Figure 5.12 shows A_1 and A_2 as a function of time with $\bar{q} = 100000 \text{ W/m}^3$ and damping coefficient $\mathscr{D} = 0.000001/\text{s}$. Both acoustic and combustion source term nonlinearities are included. We can see that both A_1 and A_2 are being damped as opposed to Figure 5.12(a) where A_1 was growing in time. And similar to Figure 5.12(b) where A_2 was decreasing in time, the addition of damping coefficient has steepened the decay of A_2 in this case.
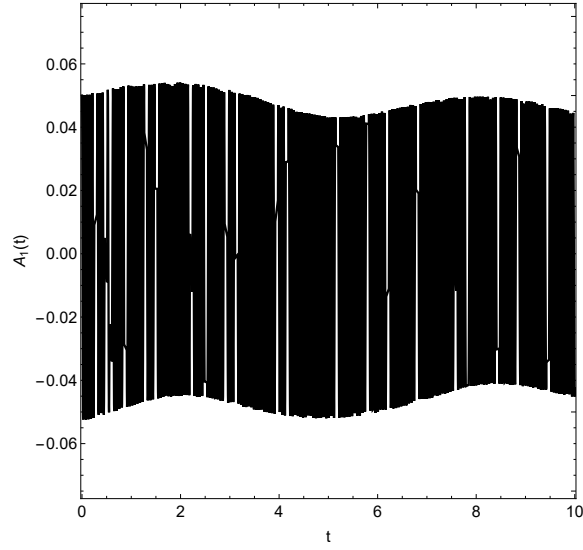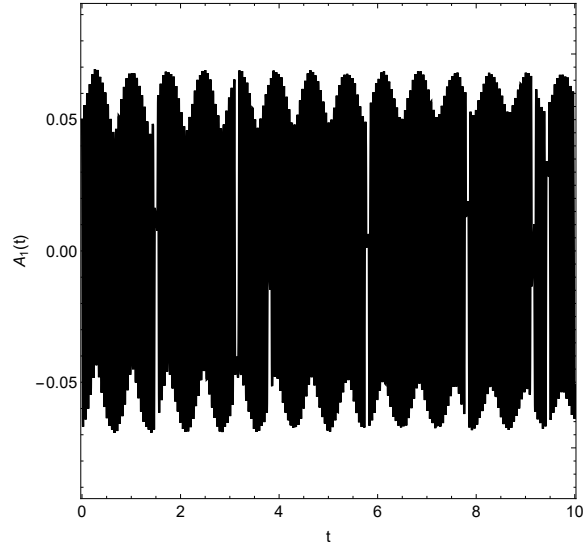
(a)
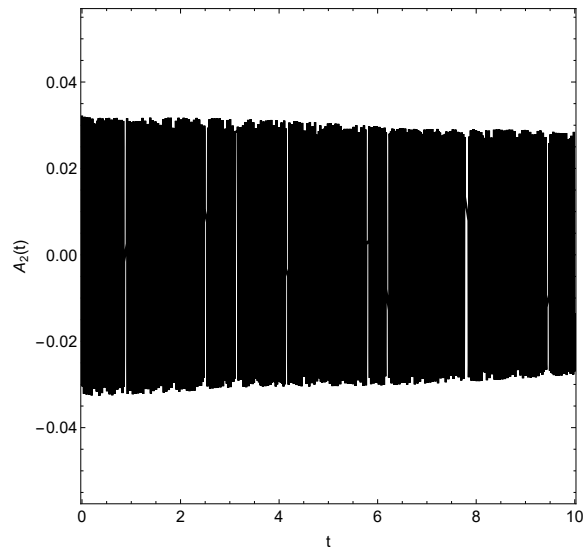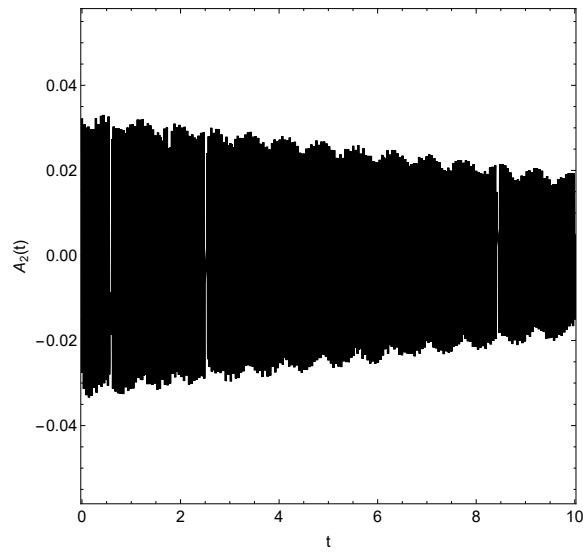

(b)

Figure 5.11: Amplitude of the (a) fundamental A_1 and (b) the first harmonic A_2 are plotted as a function of time. Both acoustic and combustion source term nonlinearities are considered. Mean heat-release rate per unit volume $\overline{q}$ is 100000 W/m³.
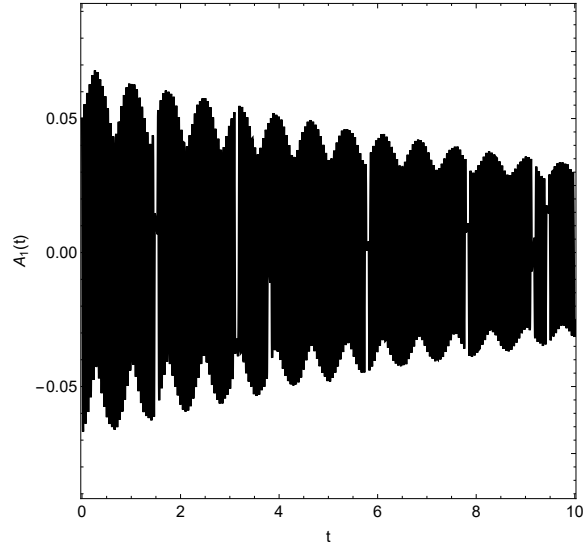
(a)
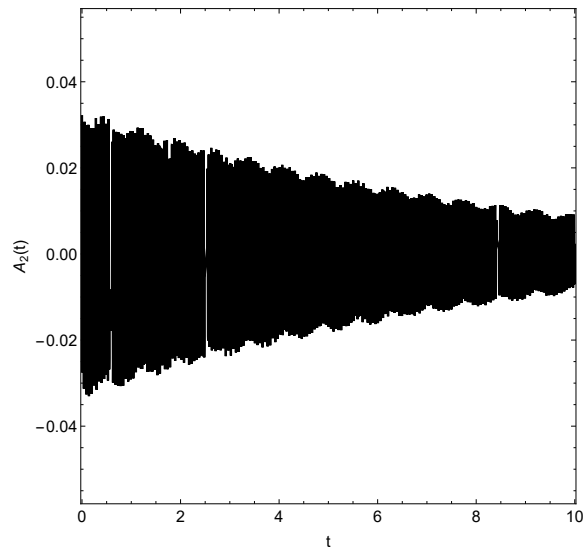
(b)

Figure 5.12: Amplitude of the (a) fundamental A_1 and (b) the first harmonic A_2 are plotted as a function of time. Both acoustic and combustion source term nonlinearities are considered. Mean heat-release rate per unit volume $\bar{q}$ is 100000 W/m^3. Damping coefficient $\mathscr{D} = 0.000001$/s.

5.5 Summary

A nonlinear acoustic wave equation with combustion source term is derived for a 1-D Rijke tube. Two second order nonlinear coupled ODEs in fundamental and first harmonic of the duct are derived. These nonlinear coupled ODEs are solved numerically to obtain the amplitudes of the duct. The system is analyzed for stability in the linear limit and the parameters governing the linear stability, namely, convective time-lag and mean heat-release rate fluctuations per unit volume are identified. In the linearly unstable regime, the limity-cycle behavior of the system is studied. It was found that, at low $\bar{q}$, acoustic nonlinearities alone are able to rein in the unbounded growth of the linear system, where as at higher $\bar{q}$ values, combustion source term nonlinearities are essential to tame the growth in the amplitudes. It was also observed that at sufficiently high $\bar{q}$, the presence of nonlinearities alone cannot contain the increase in amplitudes, i.e., the system becocmes nonlinearly unstable and only the inlcusion of damping can contain the unbounded growth in amplitudes.

CHAPTER 6

CONCLUSIONS

6.1 Conclusions

In this work, a thorough investigation of analytical methods to predict thermoacoustic instabilities in premixed combustion systems is undertaken. Novel analytical methods to predict combustion instabilities have been developed and validated against experimental and numerical results in the literature. This work begins by addressing some fundamental problems in acoustics and applies them to the study of thermoacoustic instabilities. We tackle fundamental problems and progressively build up on those ideas and apply those novel techniques to problems in thermoacoustic systems.

In Chapter 2, acoustically consistent matching conditions were developed that allows us to recover the dispersion relation for a duct with multiple changes in cross-sectional area. A detailed investigation of the effects of non-uniform laminar and turbulent mean velocity profiles was undertaken. A novel analytical solution to the inhomogeneous acoustic wave equation was developed. This novel technique incorporates the effects of the liniearized source terms directly into the axial wavenumbers. Consequently, combustion effects are incorporated directly into the axial wavenumber

in the combustion zone. In contrast to the prior studies in which heat release effects are included *a posteriori* in the form of energy balance across the flame, which inherently means that the flame is assumed to be compact, the current approach makes no such assumption. A detailed investigation of the parametric space including the effects of cross-sectional area ratio, flow Mach number and boundary conditions affecting combustion instabilities was undertaken.

In Chapter 3, a comprehensive flame transfer function for turbulent premixed flames is developed. The FTF includes the effects of fluctuations in density, heat of reaction, turbulent flame speed, and flame surface area. A novel G-equation method relating flame surface-area response to acoustic fluctuations is developed. A detailed analysis of the current FTF was undertaken for a V-shaped mean flame, wherein the effects of varying the frequency, modal index, mean Mach number, mean temperature, and mean equivalence ratio were studied. Combustion instability analysis of a 2-D dump combustor was performed by s combining this FTF with the acoustically consistent modal analysis framework developed in Chapter 2.

In Chapter 4, novel WKB-type solutions were developed for ducts with uniform and linearly varying mean temperatures and cross-sectional areas (with and without mean flow). These WKB approaches were also used to predict the resonant frequencies of a uniform duct with no mean flow and linearly varying mean temperature. The WKB approach is then applied to predict the longitudinal instabilities of a dump combustor using the acoustically conistent modal analysis framework.

And finally in Chapter 5, a generic nonlinear acoustic wave equation with combustion source term is derived for a 1-D Rijke tube. First, the system is analyzed

for stability in the linear limit and the parameters governing the linear stability, namely, convective time-lag and mean heat-release rate fluctuations per unit volume are identified. Further, in the linearly unstable regime, the limity-cycle behavior of the system is studied.

6.2   Future Work

The scope of the current work was limited to 2-D cartesian geomtery. Extending the acoustically consistent modal analysis framework and the FTF into 3-D cartesian and polar coordinates will be a exciting endeavour. In this dissertation, only acoustic fluctuations were considered. Inclusion of entropy and vorticity fluctuations will make for a much more comprehensive study. It will also be useful to study different mean flame shapes other than planar and V-flames. It will also be worthwhile to study swirl-stabilized and bluff-body-stabilized flames and their response to incident acoustic fluctuations. A comprehensive numerical investigation of eikonal methods to compute the acoustic waveforms in inhomogeneous media would be an exciting research topic. A computational (RANS/LES) study on the intermodal energy transfer, bifurcation and limit-cycle behavior of thermoacoustic systems would also be a challenging undertaking.

APPENDICES

APPENDIX A

EDGE CONDITIONS

Considering a duct with single discontinuity (see Figure 2.1), the axial velocity fluctuations in zones 1 and 2 should satisfy the following interface condition:

$$u_1'(0, y) = u_2'(0, y), \quad y \in \left[-\tfrac{S_2}{2}, \tfrac{S_2}{2}\right] \tag{A.1}$$

To determine the velocity fluctuations satisfying Eq. (A.1), we begin by writing them as

$$u_1'(x, y, t) = e^{i\Omega t} \, \hat{u}_1(x, y) \tag{A.2}$$

$$u_2'(x, y, t) = e^{i\Omega t} \, \hat{u}_2(x, y) \tag{A.3}$$

where

$$\hat{u}_1(x, y) = -\frac{1}{\bar{\rho}_1} \frac{k_{n,1}}{\Omega + \bar{u}_1 k_{n,1}} A_{n,1} \, e^{i k_{n,1} x} \cos\left(\frac{2n\pi}{S_1} y\right) \tag{A.4}$$

$$\hat{u}_2(x, y) = -\frac{1}{\bar{\rho}_2} \frac{k_{n,2}}{\Omega + \bar{u}_2 k_{n,2}} A_{n,2} \, e^{i k_{n,2} x} \cos\left(\frac{2n\pi}{S_2} y\right) \tag{A.5}$$

Letting $u_1'(0, y) = u_2'(0, y) = e^{i\Omega t} f(y)$, where $y \in [-S_2/2, S_2/2]$, we get from Eq. (A.2) and Eq. (A.3)

$$-\frac{1}{\overline{\rho}_1} \frac{k_{n,1}}{\Omega + \overline{u}_1 k_{n,1}} A_{n,1} \cos\left(\frac{2n\pi}{S_1} y\right) = f(y) \qquad (A.6)$$

$$-\frac{1}{\overline{\rho}_2} \frac{k_{n,2}}{\Omega + \overline{u}_2 k_{n,2}} A_{n,2} \cos\left(\frac{2n\pi}{S_2} y\right) = f(y) \qquad (A.7)$$

Multiplying Eq. (A.6) and Eq. (A.7) with $\cos(2n\pi/S_1)$ and integrating across the interface, we have

$$A_{n,1} = -\overline{\rho}_1 \frac{2/S_1}{1 + \delta_{n0}} \frac{\Omega + \overline{u}_1 k_{n,1}}{k_{n,1}} \int_{-\frac{S_2}{2}}^{\frac{S_2}{2}} f(y) \cos\left(\frac{2n\pi}{S_1} y\right) dy \qquad (A.8)$$

$$A_{n,2} = -\overline{\rho}_2 \frac{2/S_2}{1 + \delta_{n0}} \frac{\Omega + \overline{u}_2 k_{n,2}}{k_{n,2}} \int_{-\frac{S_2}{2}}^{\frac{S_2}{2}} f(y) \cos\left(\frac{2n\pi}{S_2} y\right) dy \qquad (A.9)$$

where δ is the Kronecker delta function. The function $f(y)$ is determined from the following interface constraint:

$$u_1'(0, y) = 0, \quad y \in \left[\frac{S_2}{2}, \frac{S_1}{2}\right] \text{ and } y \in \left[-\frac{S_1}{2}, -\frac{S_2}{2}\right] \qquad (A.10)$$

Using Eq. (A.4), Eq. (A.8), Eq. (A.9) and Eq. (2.5) in Eq. (A.10), we get the following integral equation:

$$
\sum_{n=0}^{\infty} \left(\frac{k_{n,1}^+}{\Omega + \overline{u}k_{n,1}^+} \left\{ \frac{2/S_1}{1+\delta_{n0}} \frac{\Omega + \overline{u}_1 k_{n,1}^+}{k_{n,1}^+} \int_{-\frac{S_2}{2}}^{\frac{S_2}{2}} f(y) \cos\left(\frac{2n\pi}{S_1} y\right) dy \right\} + \right.
$$
$$
\left. \frac{k_{n,1}^-}{\Omega + \overline{u}_1 k_{n,1}^-} \left\{ \frac{2/S_1}{1+\delta_{n0}} \frac{\Omega + \overline{u}_1 k_{n,1}^-}{k_{n,1}^-} \int_{-\frac{S_2}{2}}^{\frac{S_2}{2}} f(y) \cos\left(\frac{2n\pi}{S_1} y\right) dy \right\} \right) \cos\left(\frac{2n\pi}{S} y\right) = 0,
$$
$$
y \in \left[\frac{S_2}{2}, \frac{S_1}{2}\right] \quad \text{and} \quad y \in \left[-\frac{S_1}{2}, -\frac{S_2}{2}\right] \tag{A.11}
$$

To transform this integral equation into matrix form, we further write $f(y)$ in terms of basis functions $B_i(y)$ as

$$
f(y) = \sum_{i=1}^{M} c_i B_i(y) \tag{A.12}
$$

where c_i are the unknown coefficients, and the choice of $B_i(y)$ is discussed below. Thus, the problem of determining $f(y)$ is transformed into that of determining the coefficients c_i.

Equation Eq. (A.11) consists of a double summation (over the indices n and i), the evaluation of which is highly complicated. However, Mittra and Lee [16] demonstrated that if the basis functions B_i are chosen so that the convergence criterion $u'(\sigma) = O(\sigma^{-\frac{1}{3}})$ is satisfied, then the neglect of higher order terms in the summation of Eq. (A.12) does not result in a significant error. In fact, Amari et al. [88] prove rigorously that $M = 1$ will suffice. As a result, Eq. (A.11) now becomes a linear system

of equations that can be solved for the coefficients c_i, provided the basis functions B_i are chosen to satisfy Mittra and Lee's criterion.

Accordingly, we choose $B_i(y)$ to be of the following form

$$B_i(y) = \left[1 - \left(\frac{y}{S_1}\right)^2\right]^{-\frac{1}{3}} \cos\left[(i-1)\frac{2\pi}{S_1}y\right] \tag{A.13}$$

Substituting Eq. (A.13) in Eq. (A.12) and the resulting $f(y)$ into Eq. (A.11), we have a linear system of equations that can be solved for c_i. Once c_i are known, the new set of amplitudes $A_{n,1}^{\pm}$ and $A_{n,2}^{\pm}$ such that the interface condition Eq. (A.1) is satisfied can be obtained from Eq. (A.6) and Eq. (A.7). The fluctuating velocities u_1' and u_2' defined in terms of the modified amplitudes satisfy not only the interface matching conditions, but also the edge conditions. It is, therefore, clear that by appropriately modifying the amplitudes $A_{n,1}^{\pm}$ and $A_{n,2}^{\pm}$, one can obtain velocity fluctuations that satisfy the required interface matching and edge conditions. The implication of this is that the linear stability analysis described in this study may be used as is, since the focus of the linear analysis is on the coefficient matrix of the assembled system of boundary and matching conditions.

APPENDIX B

MATCHING CONDITIONS BASED ON CONSERVATION

EQUATIONS
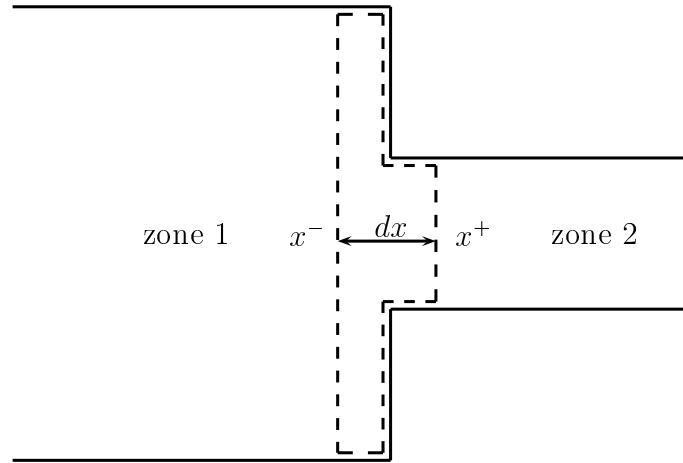
Figure B.1: Control volume of thickness dx across a zonal interface. Also indicated are the x^+ and x^- faces of the control volume.

We demonstrate this alternative approach of matching conditions for the axial momentum equation. One begins by considering a differential volume of thickness dx normal to the interface of interest as shown in Figure B.1. Equation (2.4) is multiplied with $\cos(\frac{2N\pi}{S_1}y)$ and integrated over the differential control volume with

$dx \to 0$, yielding

$$\bar{u}_1 \int_{S_1} u'_1 \cos\left(\frac{2N\pi}{S_1}y\right) dy + \frac{1}{\bar{\rho}_1} \int_{S_1} p'_1 \cos\left(\frac{2N\pi}{S_1}y\right) dy =$$
$$\bar{u}_2 \int_{S_2} u'_2 \cos\left(\frac{2N\pi}{S_1}y\right) dy + \frac{1}{\bar{\rho}_2} \int_{S_2} p'_2 \cos\left(\frac{2N\pi}{S_1}y\right) dy \qquad \text{(B.1)}$$

This approach has a few important implications. Firstly, the fluctuating velocities u'_1 and u'_2 are evaluated on the x^- and x^+ surfaces, respectively, of the control volume. This means that they are not required to rigorously satisfy the additional interface and edge condition constraints discussed in Section 2.3.1.5. Secondly, the fact that the thickness of the control volume $dx \to 0$ has a subtle implication in that the evanescent higher order modes that are generated near the discontinuity in zone 2 may not be captured. Finally, when one applies this approach to the continuity and axial momentum equations, it can be shown that one does not recover the well-known dispersion relation for the purely axial modes.

APPENDIX C

SOLUTION TO THE G-EQUATION

Solving Eq. (3.35) for ψ_1 and ψ_2 gives

$$\psi_1 = -\mathscr{C}\mathscr{E}_1 \left\{ \mathscr{E}_2 + \mathscr{E}_3 \left[\mathscr{E}_4 + \mathscr{E}_5(\mathscr{E}_6 + \mathscr{E}_7) \right] \right\} \qquad \text{(C.1)}$$

$$\psi_2 = -\mathscr{C}\mathscr{F}_1 \left\{ \mathscr{F}_2 \left[\mathscr{F}_3 + \mathscr{F}_4\mathscr{F}_5 \right] + \mathscr{F}_6 \right\} \qquad \text{(C.2)}$$

where

$$\mathscr{E}_1 = \frac{\left(m^2 + 1\right)^2}{\left(k\overline{u} - k_y m\overline{u} + m^2\Omega + \Omega\right)\left(k\overline{u} + k_y m\overline{u} + m^2\Omega + \Omega\right)}$$

$$\mathscr{E}_2 = -\frac{k_y^2 m\overline{u}}{\left(m^2 + 1\right)\overline{\rho}(k\overline{u} + \Omega)}$$

$$\mathscr{E}_3 = \frac{i(k\overline{u} + m^2\Omega + \Omega)}{\sqrt{m^2 + 1}}$$

$$\mathscr{E}_4 = \frac{km}{k\overline{\rho u} + \overline{\rho}\Omega}$$

$$\mathscr{E}_5 = \frac{C_1 \overline{\phi}^{-C_2} T_0^{-C_5} p_0^{-C_6} e^{-C_3(C_4 - \overline{\phi})^2 - i\tau\Omega}}{\chi c_v \overline{p\rho}^2 \overline{Tu}(k\overline{u} + \Omega)^2}$$

$$\mathscr{E}_6 = c_v \overline{\rho}\overline{T} T_0^{C_5} \left(\frac{\overline{T}}{T_0}\right)^{C_5} (k\overline{u} + \Omega) \left\{ -p_0^{C_6} \left(\frac{\overline{p}}{p_0}\right)^{C_6} (C_2 + 2C_3\overline{\phi}(C_4 - \overline{\phi})) \left(\chi k\overline{p} + k\overline{\rho u}^2 + \overline{\rho u}\Omega\right) \right.$$

$$\left. + \chi C_6 \overline{\rho u p}^{C_6} e^{i\tau\Omega}(k\overline{u} + \Omega) \right\}$$

187

$$\mathcal{E}_7 = -i\chi C_5 \bar{p}^2 \bar{u} \bar{T}^{C_5} p_0^{C_6} e^{i\tau\Omega} \left(\frac{\bar{p}}{p_0}\right)^{C_6} \left(ik^2 - k_y^2\right)$$

$$\mathcal{F}_1 = \frac{k_y \left(m^2 + 1\right) T_0^{-C_5} p_0^{-C_6} e^{-C_3(C_4-\bar{\phi})^2 - i\tau\Omega}}{\chi c_v \bar{p} \bar{\rho}^2 \bar{T} (k\bar{u} + \Omega)^2 \left(k\bar{u} - k_y m\bar{u} + m^2\Omega + \Omega\right) \left(k\bar{u} + k_y m\bar{u} + m^2\Omega + \Omega\right)}$$

$$\mathcal{F}_2 = c_v \bar{\rho} \bar{T} T_0^{C_5} (k\bar{u} + \Omega)$$

$$\mathcal{F}_3 = -C_1 m \sqrt{m^2 + 1} \bar{\phi}^{C_2} p_0^{C_6} \left(\frac{\bar{T}}{T_0}\right)^{C_5} \left(\frac{\bar{p}}{p_0}\right)^{C_6} (C_2 + 2C_3\bar{\phi}(C_4-\bar{\phi})) \left(\chi k\bar{p} + k\bar{\rho}\bar{u}^2 + \bar{\rho}\bar{u}\Omega\right)$$

$$\mathcal{F}_4 = \chi C_1 C_6 m \sqrt{m^2 + 1} \bar{\rho}\bar{u}\bar{\phi}^{C_2} \bar{p}^{C_6} e^{i\tau\Omega} \left(\frac{\bar{T}}{T_0}\right)^{C_5} (k\bar{u} + \Omega)$$

$$\mathcal{F}_5 = \chi \bar{p} p_0^{C_6} \left(k \left(\sqrt{m^2 + 1} m^2 + i\right) \bar{u} + i \left(m^2 + 1\right) \Omega\right) e^{C_3(C_4-\bar{\phi})^2 + i\tau\Omega}$$

$$\mathcal{F}_6 = -i\chi C_1 C_5 m \sqrt{m^2 + 1} \bar{p}^2 \bar{u} \bar{\phi}^{C_2} \bar{T}^{C_5} p_0^{C_6} e^{i\tau\Omega} \left(\frac{\bar{p}}{p_0}\right)^{C_6} \left(ik^2 - k_y^2\right)$$

$$\chi = 1/R_\rho$$

Having obtained ψ_1 and ψ_2, $G' = e^{i\Omega t} e^{ikx} [\psi_1 \cos(k_y y) + \psi_2 \sin(k_y y)]$ is the fluctuating component of level-set G governed by Eq. (3.24).

APPENDIX D

COMPARISON OF WKB AND MODAL ANALYSIS APPROACHES

As discussed in Section 4.2 Introduction, one of the principal limitations of the modal analysis approach is that it is only applicable to domains with uniform mean properties. Consequently, domains with varying mean properties would have be divided into multiple uniform-property zones. The WKB method, however, does not require multiple zones. In this appendix, we apply the the modal and WKB approaches to predict the resonant frequencies of a duct with a specified temperature gradient and no mean flow.

For the modal analysis approach, we consider four cases where the number of zones is increased from 1 to 4. For the WKB method, the entire duct is treated as a single zone. The frequency predictions from the two approaches are compared with those from the exact solutions of Sujith et al. [3].

The duct considered has a linear mean temperature profile $\overline{T}(x) = 500 - 50x$ with a length of 4 m. The duct is acoustically closed at the left end ($\frac{\mathrm{d}p'}{\mathrm{d}x}\big|_{x=0} = 0$), and open at the right end ($p'|_{x=L} = 0$). In the modal analysis approach, for the 1-zone case, the mean temperature is 400 K, which is the temperature at the center of the duct with the above linear temperature profile. For the 2-zone case, the temperatures

in the two zones are $\overline{T}_1 = 500 - 50 \times 1 = 450$ K and $\overline{T}_2 = 500 - 50 \times 3 = 350$ K

respectively. Mean temperatures are similarly obtained for the 3-zone and 4-zone

cases. In Table D.1, the frequency predictions for the fundamental mode Ω_0, as well

as the first four harmonics Ω_1 through Ω_4 are compared. It is evident that except for

the fundamental mode, the modal analysis predictions deviate significantly from the

frequencies of Sujith et al. [3], whereas the WKB results are consisently in excellent

agreement with the exact results.

Table D.1: Comparison of resonant longitudinal frequencies obtained from the modal analysis, standard and modified WKB approaches, and the exact solutions of Sujith et al. [3].

Frequency radians/s	Modal Analysis				Standard WKB	Modified WKB	Exact
	1-zone	2-zone	3-zone	4-zone			
Ω_0	133.1	137.5	138.3	138.6	148.7	150.6	148.4
Ω_1	399.2	391.8	396.1	397.3	466.1	466.8	466.4
Ω_2	665.3	666	655.2	658.8	779.5	779.9	780
Ω_3	931.4	921.8	930.1	919.4	1092.2	1092.5	1093
Ω_4	1197.5	1193.8	1188.5	1193.7	1404	1405	1406

REFERENCES

[1] M. Meissner. Effect of cross-sectional area discontinuities in closed hard-walled ducts on frequency of longitudinal modes. *Archives of Acoustics*, 35:421–435, 2010.

[2] Y. C. Yu, J. C. Sisco, V. Sankaran, and W. E. Anderson. Effects of mean flow, entropy waves, and boundary conditions on longitudinal combustion instability. *Combustion Science and Technology*, 182:739–776, 2010.

[3] R.I. Sujith, G.A. Waldherr, and B.T. Zinn. An exact solution for one-dimensional acoustic fields in ducts with an axial temperature gradient. *Journal of Sound and Vibration*, 184(3):389 – 402, 1995.

[4] Sarma L. Rani. Reduced order model for combustion instability in a two-dimensional duct with a flameholder. *Journal of Propulsion and Power*, 25(1):237–248, 2009.

[5] A. P. Dowling and S. R. Stow. Acoustic analysis of gas turbine combustors. *Journal of Propulsion and Power*, 19(5):751–764, 2003.

[6] D. H. Lee and T. Lieuwen. Acoustic near-field characteristics of a conical, premixed flame. *Journal of Acoustical Society of America*, 113(1):167–177, 2003.

[7] T. Lieuwen and B. T. Zinn. Theoretical investigation of combustion instability mechanisms in lean premixed gas turbines. In *36th AIAA Aerospace Sciences Meeting and Exhibit*, 98-0641, Reno, NV, January 1998. AIAA.

[8] T. Wang and V. Yang. Combustion response of a premixed swirl injector to longitudinal acoustic oscillations. In *35th Aerospace Sciences Meeting and Exhibit*. Aerospace Sciences Meetings, American Institute of Aeronautics and Astronautics, 1997.

[9] G. Hsio, R. Pandalia, H. Hura, and H. Mongia. Combustion dynamic modeling for gas turbine engines. In *34th AIAA/ASME/SAE/ASEE Joint Propulsion Conference and Exhibit*. Joint Propulsion Conferences, American Institute of Aeronautics and Astronautics, 1998.

[10] A. P. Dowling. The calculation of thermoacoustic oscillations. *Journal of Sound and Vibration*, 180(4):557–581, 1995.

[11] S. Hubbard and A. P. Dowling. Acoustic instabilities in premix burners. In *4th AIAA/CEAS Aeroacoustics Conference*. American Institute of Aeronautics and Astronautics, 1998.

[12] S. Hubbard and A. P. Dowling. Acoustc resonances of an industrial gas turbine system. *Journal of Engineering for Gas Turbines and Power*, 123(4):766–773, 2001.

[13] A. P. Dowling and S. Hubbard. Instability in lean premixed combustors. *Proceedings of the Institution of Mechanical Engineers Part A-Journal of Power and Energy*, 214:317–332, 2000.

[14] D. You. *A Three-Dimensional Linear Acoustic Analysis of Gas-Turbine Combustion Instablity*. PhD thesis, The Pennsylvania State University, University Park, 2004.

[15] D. Homentcovschi and R. N. Miles. A re-expansion method for determining the acoustical impedance and the scattering matrix for the waveguide discontinuity problem. *Journal of the Acoustical Society of America*, 128(2):628–638, 2010.

[16] R. Mittra and S. W. Lee. *Analytical Techniques in the Theory of Guided Waves*. Number 4–35. The Macmillan Company, 1972.

[17] R. E. Collins. *Field Theory of Guided Waves*. Number 20. IEEE, Piscataway, NJ, 1990.

[18] A. S. Omar and K. F. Schunamann. Application of the generalized spectral-domain technique to the analysis of rectangular waveguides with rectangular and circular metal inserts. *IEEE Transactions on Microwave Theory and Techniques*, 39(9), 1991.

[19] Y. Utsumi. Variational analysis of ridged waveguide modes. *IEEE Transactions on Microwave Theory and Techniques*, 33(2):111–120, 1985.

[20] F. C. Karal. The analogous acoustical impedance for discontinuities and constrictions of circular cross section. *Journal of the Acoustical Society of America*, 25(2):327334, 1953.

[21] M. L. Munjal. *Acoustics of Ducts and Muffler*. Number 2–30. Wiley-Interscience, 1987.

[22] J. W. S. Rayleigh. *The Theory of Sound*, volume 2. Dover Publications, New York, NY, 1945.

[23] Vijaya Krishna Rani and Sarma L Rani. Acoustically consistent investigation of combustion instabilities in a dump combustor. *Journal of Propulsion and Power*, pages 1–15, 2014.

[24] F. E. C. Culick. Some recent results for nonlinear acoustics in combustion chamber. In *AIAA 13th Aeronautical Conference*, 90-3927, Tallahassee, FL, October 1990. AIAA.

[25] Tim Lieuwen. *Investigation of Combustion Instability Mechanisms in Premixed Gas Turbines*. PhD thesis, Georgia Institute of Technology, 1999.

[26] Santosh Shanbhogue. *Dynamics of Perturbed Exothermic Bluff-Body Flow-Fields*. PhD thesis, Georgia Institute of Technology, 2008.

[27] S. R. Stow and A. P. Dowling. Thermoacoustic oscillations in an annular duct. In *ASME Turbo Expo*, New Orleans, LA, 2001. American Society of Mechanical Engineers.

[28] E. Gutmark, T. P. Parr, D. M. Hanson-Parr, and K. C. Schadow. Closed-loop amplitude modulation control of reacting premixed turbulent jet. *AIAA Journal*, 29(12):2155–2162, Dec 1991.

[29] A.M. Annaswamy and A.F. Ghoniem. Active control in combustion systems. *Control Systems, IEEE*, 15(6):49–63, Dec 1995.

[30] Wayne J. Dunstan, Robert R. Bitmead, and Sergio M. Savaresi. Fitting nonlinear low-order models for combustion instability control. *Control Engineering Practice*, 9(12):1301 – 1317, 2001.

[31] Ann P. Dowling and Aimee S. Morgans. Feedback control of combustion oscillations. *Annual Review of Fluid Mechanics*, 37(1):151–182, 2005.

[32] T. Sattelmayer and W. Polifke. Assessment of methods for the computation of the linear stability of combustors. *Combustion Science and Technology*, 175(3):453–476, 2003.

[33] A. Cardenas-Miranda and W. Polifke. Combustion stability analysis of rocket engines with resonators based on nyquist plots. *Journal of Propulsion and Power*, 30(4):962–977, 2014.

[34] Frank E. Marble and Sebastien M. Candel. An analytical study of the nonsteady behavior of large combustors. *Symposium (International) on Combustion*, 17(1):761–769, 1979. Seventeenth Symposium (International) on Combustion.

[35] M. V. Subbiah. Nonsteady flame spreading in two-dimensional ducts. *AIAA Journal*, 21(11), 1983.

[36] Vigor Yang and F. E. C Culick. Analysis of low frequency combustion instabilities in a laboratory ramjet combustor. *Combustion Science and Technology*, 45(1-2):1–25, 1986.

[37] T Poinsot and S. M. Candel. A nonlinear model for ducted flame combustion instabilities. *Combustion Science and Technology*, 61(4-6):121–153, 1988.

[38] C.K. Law. Dynamics of stretched flames. *Symposium (International) on Combustion*, 22(1):1381 – 1402, 1989.

[39] L Boyer and J. Quinard. On the dynamics of anchored flames. *Combustion and Flame*, 82:51–65, 1990.

[40] Paul Clavin and Jiong Sun. Theory of acoustic instabilities of planar flames propagating in sprays or particle-laden gases. *Combustion Science and Technology*, 78(4-6):265–288, 1991.

[41] K. C. Schadow, E. Gutmark, and K. J. Wilson. Active combustion control in a coaxial dump combustor. *Combustion Science and Technology*, 81(4-6):285–300, 1992.

[42] N. Darabiha and S. Candel. The influence of the temperature on extinction and ignition limits of strained hydrogen-air diffusion flames. *Combustion Science and Technology*, 86(1-6):67–85, 1992.

[43] B.H. Chao and C.K. Law. Asymptotic theory of flame extinction with surface radiation. *Combustion and Flame*, 92(1-2):1–24, 1993.

[44] M. A. Macquisten. Combustion oscillations in a twin-stream afterburner. *Journal of Sound and Vibration*, 188(4):545 – 560, 1995.

[45] M. Fleifil, A. M. Annaswamy, Z. A. Ghoneim, and A. F. Ghoniem. Response of a laminar premixed flame to flow oscillations: A kinematic model and thermoacoustic instability results. *Combustion and flame*, 106(4):487–510, 1996.

[46] Ju Hyeong Cho and Tim Lieuwen. Laminar premixed flame response to equivalence ratio oscillations. *Combustion and Flame*, 140(1-2):116–129, 2005.

[47] T. Lieuwen. Modeling premixed combustion-acoustic wave interactionss: A review. *Journal of Propuslsion and Power*, 19(5):765–781, 2003.

[48] Tim C. Lieuwen and Andrzej Banaszuk. Background noise effects on combustor stability. *Journal of Propulsion and Power*, 21(1):25–31, 2005.

[49] Tim Lieuwen, Sripathi Mohan, Rajesh Rajaram, and S. K. Preetham. Acoustic radiation from weakly wrinkled premixed flames. *Combustion and Flame*, 144(1-2):360–369, 2006.

[50] S. K. Preetham, H. Santosh, and Tim Lieuwen. Dynamics of laminar premixed flames forced by harmonic velocity disturbances. *Journal of Propulsion and Power*, 24(6):1390–1402, Nov 2008.

[51] Preetham ., S. K. Thumuluru, Tim Lieuwen, and H. Santosh. Linear response of laminar premixed flames to flow oscillations: Unsteady stretch effects. *Journal of Propulsion and Power*, 26(3):524–532, May 2010.

[52] Dong-Hyuk Shin, Dmitriy V. Plaks, Tim Lieuwen, Ulises M. Mondragon, Christopher T. Brown, and Vincent G. McDonell. Dynamics of a longitudinally forced, bluff body stabilized flame. *Journal of Propulsion and Power*, 27(1):105–116, Jan 2011.

[53] Santosh Hemchandra, Norbert Peters, and Tim Lieuwen. Heat release response of acoustically forced turbulent premixed flames-role of kinematic restoration. *Proceedings of the Combustion Institute*, 33(1):1609–1617, 2011.

[54] Danning You, Ying Huang, and Vigor Yang. A generalized model of acoustic response of turbulent premixed flame and its application to gas-turbine combustion instability aanalysis. *Combustion Science and Technology*, 177(5-6):1109–1150, 2005.

[55] Sourabh Apte and Vigor Yang. Unsteady flow evolution in porous chamber with surface mass injection, part 2: Acoustic excitation. *AIAA Journal*, 40(2):244–253, Feb 2002.

[56] C.G. Speziale. On the decomposition of turbulent flow fields for the analysis of coherent structures. *Acta Mechanica*, 70(1-4):243–250, 1987.

[57] Kenneth Kuo. *Principles of Combustion*. Wiley, 2 edition, 2005.

[58] Jr. Anderson, J.D. *Governing Equations of Fluid Dynamics*. Springer Berlin Heidelberg, 2009.

[59] GM Abu-Orf and RS Cant. Reaction rate modelling for premixed turbulent methane-air flames. *Proc. of the Joint Meeting of the Spanish, Portuguese, Swedish and British Sections of the Combust. Inst.*, 1996.

[60] GM Abu-Orf and RS Cant. A turbulent reaction rate model for premixed turbulent combustion in spark-ignition engines. *Combustion and Flame*, 122(3):233–252, 2000.

[61] Joseph B Keller. Geometrical acoustics. i. the theory of weak shock waves. *Journal of Applied Physics*, 25(8):938–947, 1954.

[62] KO Friedrichs and Joseph B Keller. Geometrical acoustics. ii. diffraction, reflection, and refraction of a weak spherical or cylindrical shock at a plane interface. *Journal of Applied Physics*, 26(8):961–966, 1955.

[63] Asbjørn Krokstad, S Strom, and Svein Sørsdal. Calculating the acoustical room response by the use of a ray tracing technique. *Journal of Sound and Vibration*, 8(1):118–125, 1968.

[64] Allan D Pierce et al. *Acoustics: an introduction to its physical principles and applications*, volume 20. McGraw-Hill New York, 1981.

[65] Victor V Krylov. Conditions for validity of the geometrical-acoustics approximation in application to waves in an acute-angle solid wedge. 1989.

[66] Victor V Krylov. Geometrical-acoustics approach to the description of localized vibrational modes of an elastic solid wedge. 1990.

[67] Jean-Dominique Polack. Playing billiards in the concert hall: The mathematical foundations of geometrical room acoustics. *Applied Acoustics*, 38(2-4):235–244, 1993.

[68] A Cummings. High frequency ray acoustics models for duct silencers. *Journal of sound and vibration*, 221(4):681–708, 1999.

[69] Allen D Pierce. Physical interpretation of the wkb or eikonal approximation for waves and vibrations in inhomogeneous beams and plates. *The journal of the Acoustical Society of America*, 48(1B):275–284, 1970.

[70] Ivan Tolstoy. The wkb approximation, turning points, and the measurement of phase velocities. *The Journal of the Acoustical Society of America*, 52(1B):356–363, 1972.

[71] Paul Filippi, Aime Bergassoli, Dominique Habault, and Jean Pierre Lefebvre. *Acoustics: basic physics, theory, and methods.* Academic Press, 1998.

[72] David T Blackstock. *Fundamentals of physical acoustics.* John Wiley & Sons, 2000.

[73] Leonid M Brekhovskikh and Oleg Godin. *Acoustics of layered media II: point sources and bounded beams*, volume 10. Springer Science & Business Media, 2013.

[74] A. Cummings. Ducts with axial temperature gradients: An approximate solution for sound transmission and generation. *Journal of Sound and Vibration*, 51(1):55 – 67, 1977.

[75] K. S. Peat. The acoustical impedance at discontinuities of ducts in the presence of a mean flow. *Journal of Sound and Vibration*, 127(1):123 –132, 1988.

[76] K. S. Peat. A first approximation to the effects of mean flow on sound propagation through cylindrical capillary tubes. *Journal of Sound and Vibration*, 175:475–489, 1994.

[77] K.S. Peat. Convected acoustic wave motion along a capillary duct with an axial temperature gradient. *Journal of Sound and Vibration*, 203(5):855 – 866, 1997.

[78] Munjal M. L. On plane-wave propagation in a uniform pipe in the presence of a mean flow and a temperature gradient. *J. Acoust. Soc. Am.*, 80:1501, 1986.

[79] B. Karthik, B. Manoj Kumar, and R. I. Sujith. Exact solutions to one-dimensional acoustic fields with temperature gradient and mean flow. *The Journal of the Acoustical Society of America*, 108(1):38–43, 2000.

[80] P.B. Subrahmanyam, R.I. Sujith, and Tim C. Lieuwen. A family of exact transient solutions for acoustic wave propagation in inhomogeneous, non-uniform area ducts. *Journal of Sound and Vibration*, 240(4):705 – 715, 2001.

[81] P. Bala Subrahmanyam, R. I. Sujith, and Tim C. Lieuwen. Propagation of sound in inhomogeneous media: Exact, transient solutions in curvilinear geometries. *Journal of Vibration and Acoustics*, 125(2):133–136, Apr 2003.

[82] FEC Culick. Report of the jannaf workshop on pressure oscillations in ramjets. In *1980 JANNAF Propulsion Meeting*, 1980.

[83] F. E. C. Culick. Combustion instability in solid rocket motors, vol. ii: A guide for motor designers. In *C. P. I. A. Publication*, volume 290, 1981.

[84] Eugene Alexander Powell. *Nonlinear combustion instability in liquid propellant rocket engines.* PhD thesis, Georgia Institute of Technology, 1970.

[85] BEN T ZINN and MANUEL E LORES. Application of the galerkin method in the solution of non-linear axial combustion instability problems in liquid rockets. *Combustion Science and Technology*, 4(1):269–278, 1971.

[86] FEC Culick. Non-linear growth and limiting amplitude of acoustic oscillations in combustion chambers. *Combustion Science and Technology*, 3(1):1–16, 1971.

[87] FEC Culick. Nonlinear behavior of acoustic waves in combustion chambersii. *Acta Astronautica*, 3(9-10):735–757, 1976.

[88] S. Amari, J. Bornemann, and R. Vahldieck. Application of a coupled-integral-equations technique to ridged waveguides. *IEEE Transactions on Microwave Theory and Techniques*, 44(12):2256–2264, 1996.